3D Multiresolution Statistical Approaches for Accelerated Medical Image and Volume Segmentation

Thesis submitted for the degree of
Doctor of Philosophy

By

Shadi Mahmoud Faleh Al Zu'bi

Electronic and Computer Engineering
School of Engineering and Design
Brunel University, West London

February 2011

Abstract

Medical volume segmentation got the attraction of many researchers; therefore, many techniques have been implemented in terms of medical imaging including segmentations and other imaging processes. This research focuses on an implementation of segmentation system which uses several techniques together or on their own to segment medical volumes, the system takes a stack of 2D slices or a full 3D volumes acquired from medical scanners as a data input.

Two main approaches have been implemented in this research for segmenting medical volume which are multi-resolution analysis and statistical modeling. Multi-resolution analysis has been mainly employed in this research for extracting the features. Higher dimensions of discontinuity (line or curve singularity) have been extracted in medical images using a modified multi-resolution analysis transforms such as ridgelet and curvelet transforms.

The second implemented approach in this thesis is the use of statistical modeling in medical image segmentation; Hidden Markov models have been enhanced here to segment medical slices automatically, accurately, reliably and with lossless results. But the problem with using Markov models here is the computational time which is too long. This has been addressed by using feature reduction techniques which has also been implemented in this thesis. Some feature reduction and dimensionality reduction techniques have been used to accelerate the slowest block in the proposed system. This includes Principle Components Analysis, Gaussian Pyramids and other methods. The feature reduction techniques have been employed efficiently with the 3D volume segmentation techniques such as 3D wavelet and 3D Hidden Markov models.

The system has been tested and validated using several procedures starting at a comparison with the predefined results, crossing the specialists' validations, and ending by validating the system using a survey filled by the end users explaining the techniques and the results. This concludes that Markovian models segmentation results has overcome all other techniques in most patients' cases. Curvelet transform has been also proved promising segmentation results; the end users rate it better than Markovian models due to the long time required with Hidden Markov models.

Acknowledgement

First of all, I would like to express my sincere thanks to my supervisor Dr. Maysam Abbod not only for his advices and guidance during this research, but for his encouragement and friendship. I would also like to thank my second supervisor Professor Wamadeva Balachandran for giving me rich feedbacks which helped improving the proposed work. I am thanking as well my ex-supervisor Dr. Abbes Amira who worked with me step by step at the early stages to build a solid base to start this research.

I would like to acknowledge Dr. Mwaffaq AlHeis - head of Diagnostic Radiology and Nuclear Medicine Department at King Abdullah University Hospital, in Ramtha-Jordan and all the radiologists working there for providing a free of use efficient data diagnosed by cancer and validating the proposed system. I further wish to thank Mr. Bal Sanghera from Paul Strickland Scanner Centre at Mount Vernon Hospital in London-UK for useful discussion regarding my work and for his help also in validating this research.

Thanks also go to my friends and colleagues within Brunel University. Thanks to Naser, Noor, Saeed, David, Nabhan, Fahed, Bader, Zeyad, Yousef, Masarweh, Nawayseh for each single moment we spent together and appreciated throughout this challenging research.

My deepest gratitude goes to my Father, Mother, Brothers (Fadi, Hadi, and Ahmed), sister and all family members for their wishes. Finally, I am passing my thankfulness to my wife and daughter for their constant encouragement, love and support and for the never failing confidence they have in me.

As it is impossible to acknowledge everyone, I would like to thank all those who have contributed, in any way, to this research. Above all, it was with the help of God, that I was able to complete this work.

Author's Publications

Journal Papers:

- *Shadi AlZu'bi and Abbes Amira, "3D Medical Volume Segmentation Using Hybrid Multiresolution Statistical Approaches," Advances in Artificial Intelligence, Special issue on Machine Learning Paradigms for Modeling Spatial and Temporal Information in Multimedia Data Mining, vol. 2010, 2010.*
- *Shadi AlZu'bi and Maysam Abbod, "Multi-resolution Analysis using Wavelet, Ridgelet, and Curvelet Transforms for Medical Image Segmentation," International Journal of Biomedical Imaging, vol. 2010, 2010 [Submitted].*

Conference Papers:

- *Shadi AlZu'bi, Naveed Islam and Maysam Abbod, "3D Multiresolution Analysis for Reduced Features Segmentation of Medical Volumes Using PCA," 2010 IEEE Asia Pacific Conference on Circuits and Systems (APCCAS 2010), Kuala Lumpur, Malaysia, 2010.*
- *Shadi AlZu'bi, Naveed Islam and Maysam Abbod, "Enhanced Hidden Markov Models for Accelerating Medical Volumes Segmentation," The 6th 2011 IEEE GCC Conference and Exhibition (IEEE GCC), Dubai, UAE, 2011.*
- *Shadi AlZu'bi and Hamideh Rezaee, Ali Aghagolzadeh and M. Hadi Seyedarabi "Tracking and Occlusion Handling in Multi- Sensor Networks by Particle Filter," The 6th 2011 IEEE GCC Conference and Exhibition (IEEE GCC), Dubai, UAE, 2011.*
- *Shadi AlZu'bi and Maysam Abbod, "Efficient Implementation and Evaluation of Wavelet Packet for Medical Image Segmentation," 2011 IEEE International Symposium on Medical Measurements and Applications Proceedings (MeMeA), Bari, Italy, May, 2011.*

- *Shadi AlZu'bi and Maysam Abbod, "Multi-Resolution Analysis using Curvelet and Wavelet Transforms for Medical Imaging," 2011 IEEE International Symposium on Medical Measurements and Applications Proceedings (MeMeA), Bari, Italy, May, 2011.*

Invited Abstracts

- *Shadi AlZu'bi and Abbes Amira, "Efficient Implementation of Wavelet Packet for Medical Image Segmentation and Analysis," The second SED research student conference (RESCON 2009), Brunel University-West London, June, 2009.*
- *Shadi AlZu'bi and Maysam Abbod, "3D Multiresolution Analysis for Segmenting Reduced Features Medical Volumes Using PCA," The Third SED research student conference (RESCON 2010), Brunel University-West London, June, 2010.*

Invited Poster Conferences

- *Shadi AlZu'bi and Abbes Amira, "Multiresolution statistical Approaches for 3D medical Imaging," The graduate school research student poster conference, Brunel University-West London, May, 2009.*
- *Shadi AlZu'bi and Abbes Amira, "Efficient Implementation of Wavelet Packet for Medical Image Segmentation and Analysis," The second SED research student poster conference (RESCON 2009), Brunel University-West London, June, 2009.*
- *Shadi AlZu'bi, "Multiresolution Analysis for Medical Image Segmentation," The 6th 2011 IEEE GCC Conference and Exhibition (IEEE GCC), Dubai, UAE, 2011.*

List of Abbreviations

No.	Number
%	Percentages
1D	One Dimensional
2D	Two Dimensional
3D	Three Dimensional
AMIDE	A Medical Image Data Examiner
AR	Autoregressive
CAT	Computed Axial Tomography
CNR	Contrast to Noise Ratio
CRT	Continuous Ridgelet Transform
CT	Computed Tomography
dB	Decibels
DHMM	Discrete HMM
DICOM	Digital Imaging and Communications in Medicine images
DSC	Dice Similarity Coefficient
DWT	Discrete Wavelet Transform
ED	Euclidean Distance
EM	Expectation Maximization
FBP	Filtered Back Projection
FDCT	Fast Discrete Curvelet Transform
FDG	Fluor-Deoxy-Glucose
FFT	Fast Fourier Transform
fMRI	functional Magnetic Resonance Imagery
FR	Feature Reduction
FRAT	Finite Radon Transform
FRIT	Finite Ridgelet Transform
GHMM	Gaussian HMM
GPR	Gaussian Pyramids Reduction
HMM	Hidden Markov Model
HWF	Haar Wavelet Filter
ICM	Iterated Conditional Modes

IDRT	Inverse Discrete Radon Transform
iFFT	inverse Fast Fourier Transform
JUST	Jordan University of Science and Technology
KAUH	King Abdullah University Hospital
LC 2D-HMM	Low-Complexity Two Dimensional HMM
LR	Left-Right
LRB	Left-Right Banded
mm	Millimeters
MRA	Multi-Resolution Analysis
MRFM	Markov Random Field Model
MRI	Magnetic Resonance Imaging
MSE	Mean Square Error
NDXWPT	Non-Decimated Complex Wavelet Packet Transform
OOI	Objects of Interest
OSEM	Ordered Subset EM
P2D-HMM	Pseudo Two Dimensional HMM
PCA	Principal Components Analysis
PET	Positron Emission Tomography
PMT	Photo Multiplier Tubes
PSNR	Peak Signal to Noise Ratio
R&D	Research and Development
RF	Radio Frequency
ROI	Region of Interest
SAR	Synthetic Aperture Radar
SBR	Spheres to background ratio
sec	Second
SHMM	Structural Hidden Markov Model
SNR	Signal to Noise Ratio
SPECT	Single Photon Emission Computed Tomography
SPM	Statistical Parametric Map
S-transform	Sequential transform
USFFT	Unequally-spaced FFT
VED	Volume Edge Detection
WP	Discrete Wavelet Packet Transform

Table of contents

Chapter 7 Medical Image Segmentation Process Acceleration

Chapter 8 System Validation for Real Applications

List of Figures

List of Tables

Chapter 1

Introduction

1.1. Introduction to Medical Image Segmentation Systems

Medical imaging is the process of creating images of the human body for clinical purposes, a medical procedure seeking to reveal, diagnose or examine disease, or a medical science including the study of normal anatomy and physiology [1] (the imaging of removed organs and tissues can also be performed).

Medical image segmentation is the process of labeling each voxel in a medical image dataset to indicate its tissue type or anatomical structure. The labels that result from this process have a wide variety of applications in medical research and visualization [1][2]. In recent years, the demand for medical image segmentation systems has risen significantly. Both commercial and healthcare organizations require methods to facilitate the process of analysis undertaken by their staff.

The segmentation system input data is a grayscale digital medical imagery such as results of the most popular scanners: Positron Emission Tomography (PET), Computed Tomography (CT) and Magnetic Resonance Imaging (MRI). The desired or the segmented

output contains the labels that classify the input grayscale voxels. The purpose of segmentation is to provide richer information than that which exists in the original medical images alone. The collection of labels that is produced through segmentation is succinctly described with regard to function as a voxel by voxel guide to the original imagery [2]. Segmentations are also valuable in building anatomical atlases, researching the shapes of anatomical structures, and tracking anatomical changes over time.

2D grayscale images on a light box are insufficient for many applications, due to the classical methods of medical image analysis. When detailed or quantitative information about the appearance, size, or shape of patient anatomy is desired, image segmentation is usually the crucial first step [3]. Many interesting applications are based on image segmentation, including 3D visualization, volumetric measurement, research into shape representation of anatomy, image-guided surgery and detection of anatomical changes.

In contrast to generic segmentation methods, methods used for medical image segmentation are often application specific, they can use the prior knowledge for particular Objects Of Interest (OOI) and other expected or possible structures in the image. This has led to the development of a wide range of segmentation methods addressing specific problems in medical applications [4]. The study of detecting lesions in the human body is an important application of segmentation tools. A contour detection algorithm based on a radial edge-detection filter was developed for Digital Imaging and Communications in Medicine (DICOM) images acquired from medical scanners such as PET, CT or MRI. The objective of segmentation algorithm is to define a Region Of Interest (ROI) in terms of size and type; this may be a lesion, or any foreign object in the human body [1].

Computational time is an important issue that must be kept in mind when using any application [5]; computational time is very important in medical image segmentation systems. In order to implement a real time system, the employment of slow segmentation methods should to be either avoided or accelerated (if applicable). Many accelerators are available, but not all of them can be used to accelerate the segmentation process due to the data loss that should be avoided in medical imaging, as well as other important factors.

The slowest blocks in the proposed system were accelerated using some Feature Reduction (FR) techniques. FR or dimension reduction is the process of reducing the number of random variables under consideration and can be divided into feature selection and feature extraction.

1.2. Aim of the Project and Research Objectives

Due to the important roles of medical image archiving and analysis, and their wide range of uses, this research has several applications. The reason for doing this research is to investigate the best way to implement a robust, accurate and automatic segmentation system; this may include multiple techniques used together to ensure that best segmentation results are delivered. The system was tested first on predefined phantom data before its generalization it for real clinical applications, as well as it used to be as fast as possible.

The main aim of this research is to enhance the application of some segmentation techniques, and use them together with other implemented techniques in medical volumes

segmentation to make the system more accurate, robust, lossless and faster in computational time. This aim can be achieved by targeting the following objectives:

- Review the related literature that has been previously done in the area of medical image processing and its applications.
- Investigate the use of wavelet transform and higher dimensional multiresolution analysis including ridgelet and curvelet transforms in medical image segmentation systems.
- Enhance the use of Hidden Markov Models for medical image segmentation by using gray scale values to generate the observation sequence and the emission matrix.
- Segment medical volumes directly using 3D techniques instead of applying 2D techniques on each slice independently, in order to get more accurate results.
- Accelerate the slowest blocks in the proposed system to reach a fast time segmentation system using software accelerators such as FR techniques.
- Come up with a new automatic, unsupervised and real time segmentation system incorporating different segmentation techniques to be used with the scanners directly.
- Validate the implemented system for real clinical applications using several procedures and pre-analyzed clinical datasets affected by lesions.
- Investigate the use of the proposed systems for other purposes.

1.3. Motivations

Two fundamental aspects of medical imagery make segmentation a difficult problem. The first aspect is the imaging process itself, and the second is the anatomy that is being

imaged. For any imaging process, the output image's interactions with the tissues of interest will provide clinically relevant information about the tissue in the resulting output image. However, this does not mean that the anatomical feature of interest will be particularly separable from its surroundings; it will not be a constant grayscale value, and its borders will not be presented by strong edges. In fact, due to noise in the image as well as the inhomogeneity of human tissues, the interaction of the imaging process with the tissue of interest will often produce a "grainy" region that is more detectable by the human eye than by sophisticated computer algorithms. Therefore, simple image processing such as thresholding is not generally successful when applied to medical image segmentation.

Thresholding and some other simple image processing techniques are lossy techniques; this means that many important features will be lost in the transformed image after applying those techniques for medical image segmentation. These features could be presenting an important factor in quantifying the cancer. Some other lossy techniques are used within the proposed system, but the data loss occurred here are mostly in the noise surrounding the main obstacles. Wavelet transform is an example of those techniques, unwanted noise is lost and the important features are extracted. Although wavelet is lossy, but it is very solid in the proposed system, the original image can be extracted from the transformed output at any time.

The preferred type according to data loss is the lossless techniques, those techniques transformed the image and segment it without any data loss, curvelet transform is one of the lossless techniques. Applying curvelet transform on medical images deliver a transformed output highlighting the important features without any changes in the other image features.

Many segmentation techniques have been implemented for the purpose of medical image segmentation, some of them could deliver a good segmentation accuracy but fail in other performance factors, such as the long computational time required for segmentation. The segmentation process accuracy is very important in medical imaging and cancer diagnosis; the transformed image (segmented one) should be as much reliable as possible and significant errors (especially for the detection stage) are not accepted. The work that have been done before in this area with its limitations and benefits will be further explained in detail in chapter 3.

The proposed system focuses on facilitating the process of analyzing medical images, particularly complex images that cannot be analyzed easily based on the radiologists vision. Different techniques have been implemented in this thesis and used together to deliver an accurate, lossless, solid, fast and easily analyzed segmented output. Fig. 1.1 illustrates the proposed medical image segmentation system which has been designed to address the segmentation difficulties and facilitate the work of the end users. The segmentation process can be done in two ways, either to use 2D segmentation techniques to segment all slices one by one and then do the volume reconstruction to create the segmented volume. The other way is to use the 3D segmentation techniques directly on the scanner output without any partitioning into slices.

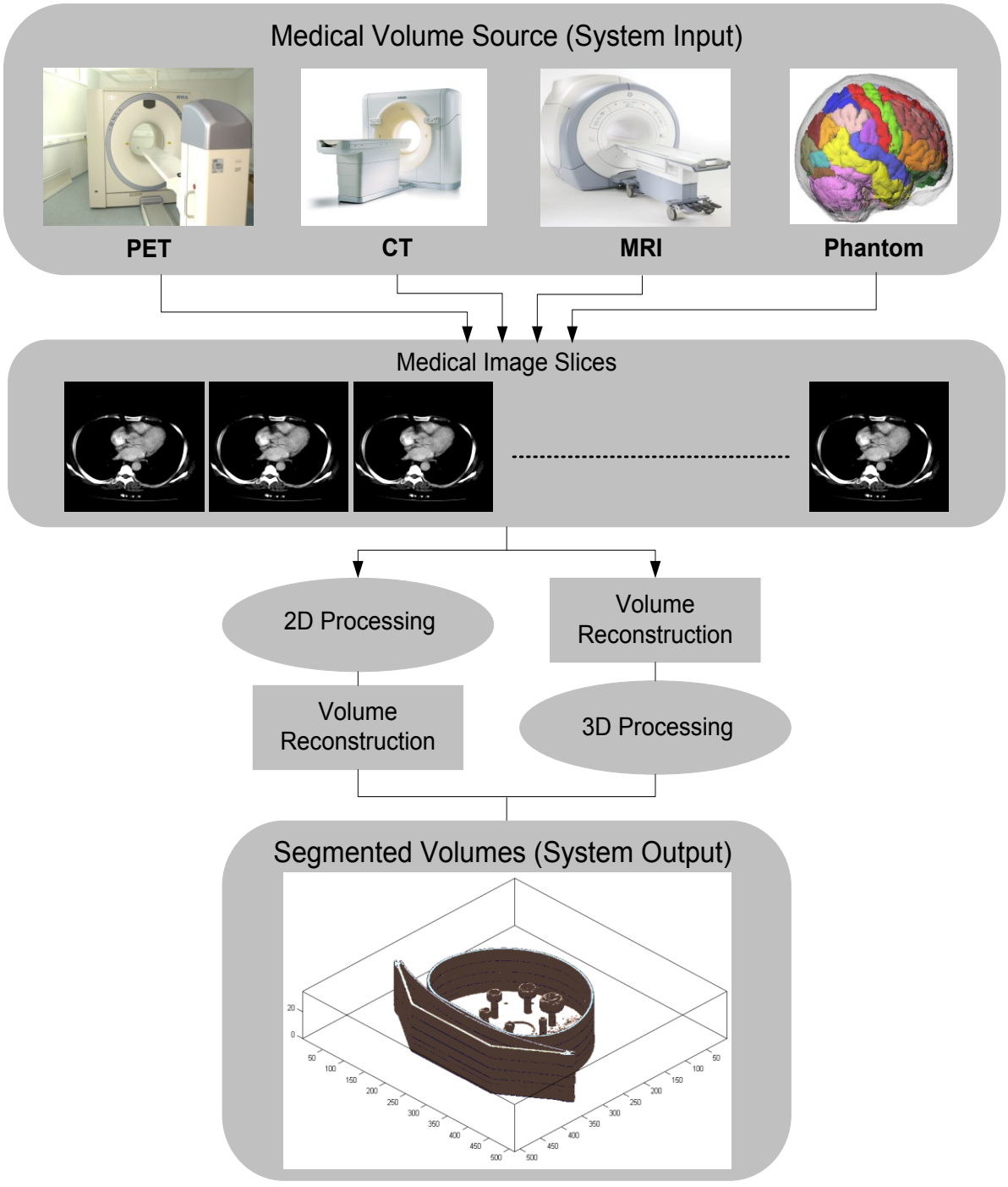

Fig. 1.1: The proposed medical image segmentation system

1.4. Contributions to knowledge

- Some of the proposed techniques have been used before in other applications including image processing and other areas. Multi-Resolution Analysis (MRA) using wavelet transform has been previously used in signal processing, power system protection, numerical analysis, managing databases, face recognition, image compression and many other applications, including medical image segmentation. The novelty here is to enhance the wavelet transform; different decompositions and filter types have been implemented in this study to deliver the most possible accurate results. Higher dimensional singularities MRA such as ridgelet and curvelet transforms have been implemented here to improve segmentation process. These two transforms have been implemented before in other applications, but never used for medical image segmentations, especially in collaboration with other system.
- The second novelty implemented in this study is the enhanced use of Hidden Markov Models (HMMs) in medical image segmentation; HMMs have been employed for the purpose of medical imaging as well as other imaging applications. What is new here is the use of a new kind of observation sequence to train the image data, and the consideration of gray scale values in forming the probability matrices during the training HMM process. This makes the segmented results more accurate, and renders sharper edges. Pseudo 2D HMMs, which have been used previously only in face recognition applications, are employed here to strengthen the process of applying HMMs on medical images, and to make it lossless.

- 3D medical volume illustration and segmentation is available, but it has been avoided by many researchers because of the long computational time required, which greatly affects the overall segmentation system quality. This has been considered in this thesis, and the 3D segmentation techniques were accelerated by reducing the medical volume features without significant data loss. Feature reduction using Gaussian pyramids and wavelet transform have been used before, but the important contribution here is the employment of principle component analysis in reducing the volume dimensions.
- The proposed system itself defines a contribution to knowledge; the system implemented is to be employed with medical scanners to facilitate radiologists' analysis. The system includes new features such as MRA and statistical modeling, which can segment in collaboration with other previously available techniques, enabling the execution of segmentation process in the fastest applicable time.

1.5. Thesis Road Map

The structure of this thesis is as follows:

- Brief overviews for the popular medical imaging modalities that their output images have been used in this thesis are provided in Chapter 2. The visualization and analysis software applications which are helping in validating the proposed techniques are introduced in this chapter as well.

- In Chapter 3, a summary of modern methodologies utilized for medical volumes segmentation is discussed, along with the methods used to measure the system performance.
- Chapter 4 presents the use of 2D multiresolution analysis for medical image segmentation system. Wavelet transform and new higher dimensional MRA transforms such as ridgelet and curvelet have been used in the medical image segmentation system for extracting the important features from the medical images.
- An enhanced version of HMMs has been implemented and used in chapter 5 for segmenting medical images automatically. Results of using HMMs for segmenting a proposed phantom dataset have been analyzed also in this chapter.
- In Chapter 6, medical volumes have been segmented directly using different 3D segmentation techniques without slicing the medical volume into a stack of 2D slices. 3D thresholding, 3D discrete wavelet transform and the new 3D HMMs are implemented in this chapter, and results using the proposed dataset are provided.
- Chapter 7 presents feature reduction techniques that can be help in accelerating the computational time of medical image segmentation process. Different feature reduction techniques are used here to reduce the dimensionalities of the tested datasets. Computational time acceleration results are provided in this chapter.
- In Chapter 8, the proposed system has been validated using different procedures. Patients' real clinical datasets which are previously analyzed by the end users of the system (radiologists) are tested, and the results achieved are compared to

their provided report of the diagnosed patients. The proposed system will be also validated in this chapter using a special survey filled in by those end users.

- Final conclusions and suggestions for future work are documented in Chapter 9.
- Appendix A presents the survey used to validate the proposed system with the end users.

Chapter 2

Overview of Medical Imaging using 3D Acquisition Systems

2.1. Introduction

In this chapter, a brief overview of using different scanners for acquiring the medical volumes has been introduced. The acquired data sets can be taken at different environments and different ways. The first step in the scanning process produces isolated parts of the scanned volume; different techniques can be applied then to reconstruct the 3D volume. Finally, the reconstructed volume can be divided into a number of slices which have the same thickness to facilitate the process of locating ROI in the scanned body part.

Three different scanners outputs have been used in this research, which are the most popular scanners: PET, CT or MRI scans. These scanners are briefly explained in section 2.2. Section 2.3 illustrates different volume reconstruction techniques that have been used within the scanners. The visualization and analysis software that have been used in

this thesis will be introduced in section 2.4. In section 2.5, the work presented in this chapter has been summarized.

2.2. Acquisition Systems

In this section, the most popular medical scanners have been introduced.

2.2.1. Positron Emission Tomography

In modern clinical diagnosis, PET is becoming one of the most frequently utilized medical imaging modalities. PET is a tomographic technique which is used to measure physiology and function rather than anatomy by imaging elements such as carbon, oxygen and nitrogen which have a high abundance within the body [6]. The most significant difference between PET and its close relative Single Photon Emission Computed Tomography (SPECT) is that the radio-pharmaceuticals used in PET emit positrons, which results in the creation of two γ-rays after annihilation with an electron in tissue [7]. For this reason, the instrumentation used in PET is designed to produce imagery containing less noise and superior spatial resolution than in SPECT [8].

PET imaging is utilized in the clinical specialties of oncology, cardiology and neurology. The major disadvantages of PET revolve around its astronomical cost, typically £1.5 million for a system [1], and the need to have specialized equipment in close proximity to produce positron-emitting nuclides as their half-lives are extremely short [8][9][10].

PET imaging is a diagnostic imaging modality used to map the distribution of positron emitting radio-pharmaceuticals within the body. These agents are created using a cyclotron and are radioactive equivalents of biologically active molecules, Fluor-Deoxy-Glucose (FDG) radio pharmaceutical which contains ^{18}F and ^{11}C is used. As illustrated in equation (2.1) isotopes such as ^{18}F and ^{11}C undergo radioactive decay by emitting a positron, where a positron is a positively charged electron (e^+) and a neutrino v [5][8][10].

$$ {}^{A}_{Z}X \rightarrow {}_{Z-1}{}^{A}X + e^{+} + v \qquad (2.1) $$

The positron travels around 1mm in tissue in a random manner before annihilating with an electron. As illustrated in equation (2.2), this reaction creates two γ-rays with energies of 511keV. These γ-rays travel in opposite directions at angle 180^{o} to one another [8].

$$ e^{+} + e^{-} \rightarrow \gamma + \gamma \qquad (2.2) $$

The PET system comprises of an entire ring of scintillation crystals which surround the patient because both γ-rays must be detected. A schematic of a PET head scanner showing annihilation coincidences is illustrated in Fig. 2.1.

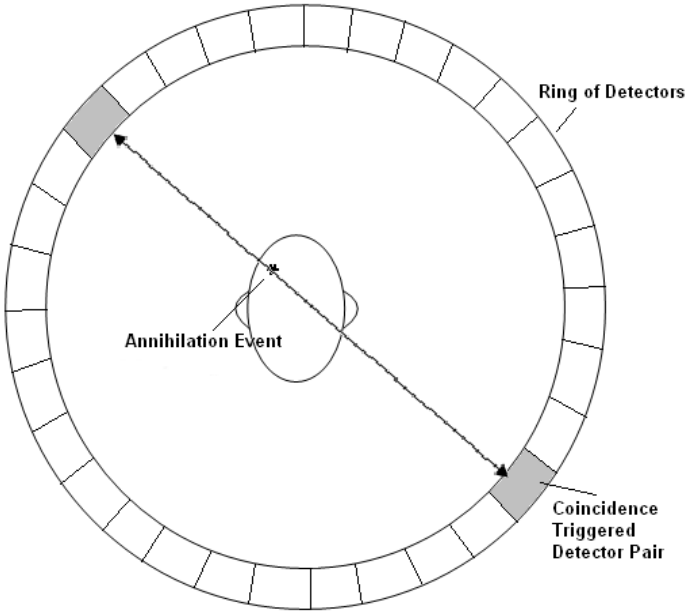

(a)

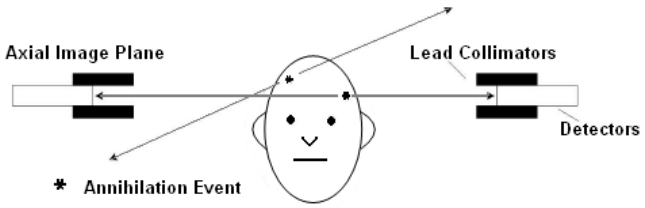

(b)

Fig. 2.1: Detection scheme for PET imaging. (a) Transaxial view of detection system. (b) The anterior view shows how only radio-nuclides in a particular cross-sectional plane will be detected by the rings of detectors [11].

In Fig. 2.1, the scintillation crystals are used to convert the energy of the γ-rays into light, which can be converted into the electronic signal by Photo Multiplier Tubes (PMT). The image is formed by analyzing the spatial distribution and the magnitude of the electric signals from each PMT. A large number of scintillation crystals are required for the detection of anti-parallel γ-rays which are placed in a circular arrangement around the patient and are

coupled to a smaller number of PMTs. Coupling each crystal to a single PMT would increase the scanner cost prohibitively, but would allow for the highest obtainable spatial resolution [5][8]. As the two γ-rays are formed simultaneously, they are detected within a specific time window, determined by location of the radio pharmaceutical within the body and the diameter of the detector ring [12]. The location of the two scintillation crystals that detect the γ-rays defines a line along which the annihilation must have occurred. This line is forming the basis of signal localization in PET. This signal localization accounts for the superior detection efficiency in PET than in SPECT, which requires the collimation of single γ-rays. The γ-ray energy of 511keV in PET is much higher than the energy of γ-rays in conventional nuclear medicine. This high energy means less attenuation of γ-rays occur in tissue. This is a second feature resulting in the high sensitivity of PET. The spatial resolution in PET depends on the number and size of individual crystal detectors and is normally within the range of 3mm - 5mm [13][14].

2.2.2. Computed Tomography

The technique of X-ray CT was invented in 1972 by Godfrey Hounsfield. Allan Cormack had independently completed earlier work on the mathematics of this technique and in 1979 they were jointly awarded the Nobel Prize in Medicine [15].

To obtain an image from a thin slice of tissue, the X-ray beam is collimated to give a thin beam. To produce a 1D projection the total number of X-rays that are transmitted through the patient is recorded by means of detectors which are situated opposite the X-ray

source. The 2D distribution of tissue attenuation coefficients within the slice determines the signal intensities in this projection. The X-ray source and the detectors are then rotated by a certain angle and the measurements repeated, continuing until sufficient data has been collected to reconstruct an image with high spatial resolution [8][16][17].

CT is used for a wide range of clinical conditions, one of the most important applications being the investigation of head trauma. It is also useful for the diagnosis of many abdominal diseases and for the detection of pulmonary disease [17]. CT provides geometric superiority and slightly increased spatial resolution over MRI, however, CT exposes the patient to high doses of radiation and may be invasive when the administration of contrast agents is required [18]. Examples of CT imagery are shown in Fig. 2.2.

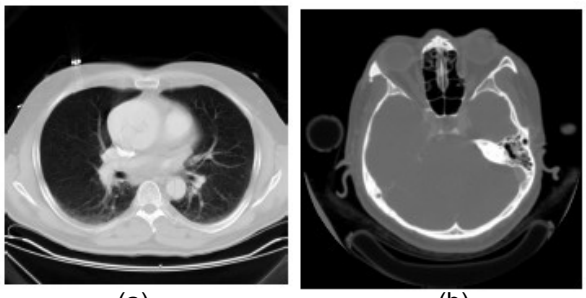

(a) (b)

Fig. 2.2: CT images (a) Transaxial CT lung slice. (b) Transaxial CT head slice [19].

CT is a medical imaging device which combines in a single gantry system for both PET and an X-Ray, so that images acquired from both devices can be taken sequentially, in the same session from the patient and combined into a single superposed image [18].

PET/CT has revolutionized many fields of medical diagnosis, by adding precision of anatomic localization to functional imaging, which was previously lacking from pure PET

imaging. For example, in oncology, surgical planning, radiation therapy and cancer staging have been changing rapidly under the influence of PET/CT availability, to the extent that many diagnostic imaging procedures and centres have been gradually abandoning conventional PET devices and substituting them by this scanner type. Although the combined device is considerably more expensive, it has the advantage of providing both functions as stand-alone examinations, it can be assumed as two devices in one [19].

While a CT scan provides anatomical detail (size and location of the tumour, mass, etc.), a PET scan provides metabolic detail (cellular activity of the tumour, mass, etc.). Fig. 2.3 illustrates an example comparing PET/CT scans with both PET and CT scans.

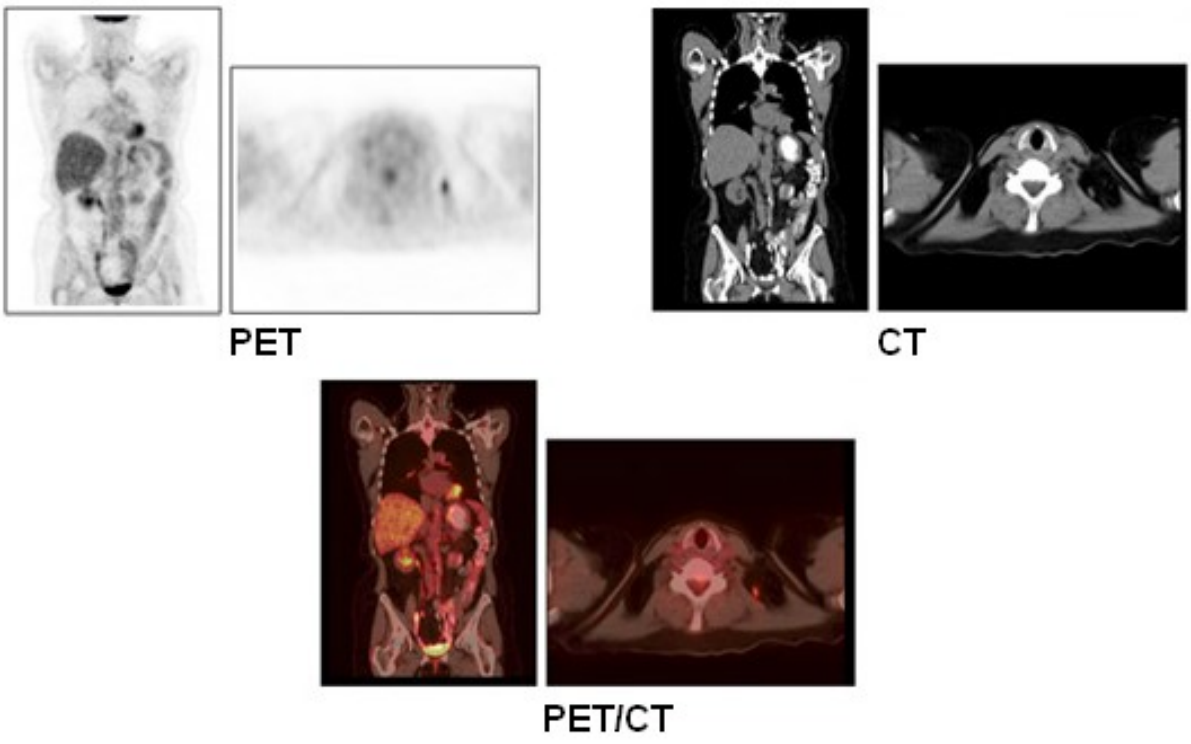

Fig. 2.3: An example illustrates the benefits of using PET/CT

2.2.3. Magnetic Resonance Imaging

In July 1977, the first MRI exam ever performed on a human being took almost five hours to produce one image. The images were quite ugly compared to today's standards. Dr. Raymond Damadian and colleagues worked for seven long years to reach this point. They named their original machine Indomitable to capture the spirit of their struggle to do what many said could not be done.

The basic design used in most MRI machines is a giant cube, the cube in a typical system might be 7 feet tall by 7 feet wide by 10 feet long (2 m by 2 m by 3 m), although new models are rapidly shrinking. There is a horizontal tube running through the magnet from front to back known as the bore of the magnet [20].

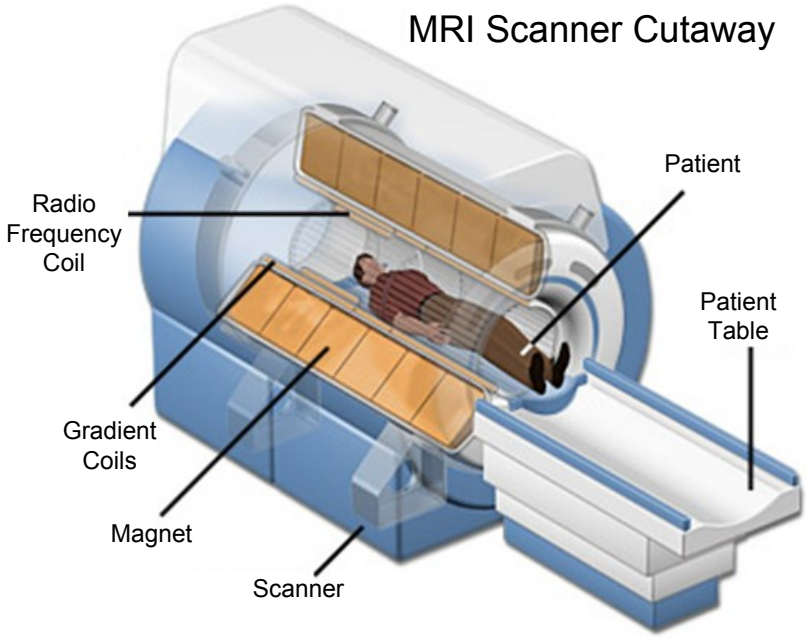

Fig. 2.4: Basic design of MRI scanner [20]

The lying patient slides into the bore on a special table, the patient goes in head first or feet first. MRI scanners vary in size and shape, and newer models have some degree of openness around the sides, but the basic design is the same (Fig. 2.4). Once the body part to be scanned is in the exact centre or isocentre of the magnetic field, the scan can begin.

Doctors use an MRI because it is one of the limited ways to see inside your body without to cut you open. An MRI system can create axial images as well as images in the sagittal plane and coronally or any degree in between, without the patient ever moving. If you have ever an X-ray, you know that every time they take a different picture, you have to move. The three gradient magnets discussed earlier allow the MRI system to choose exactly where in the body to acquire an image and how the slices are oriented. Fig. 2.5 defines the three main axis that can be acquired from MRI.

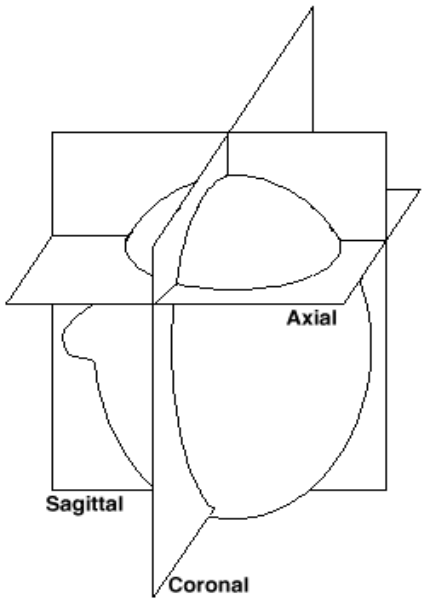

Fig. 2.5: Axial, coronal and sagittal slices

2.3. 3D volume reconstruction

Image reconstruction is the process of mapping the radio activities as a function of location for parcels or bits of tissue and will be constructed and plotted (converting the 1D protection to cross sectional image). The image plane formed between two crystals in the same ring (n: Direct plane) or between two crystals in adjacent rings (n-1: Cross plane) produces 2n-1 image planes. Coincidence events can be grouped into projections images (called sinograms). If the septa between crystals removed, the number of planes will be *n* x *n* which produces the 3D. There are two main ways for reconstruction [27]:

- **Filtered Back Projection (FBP):** FBP has been frequently used to reconstruct images from the projections. This algorithm has the advantage of being simple while having a low requirement for computing resources.
- **Iterative expectation-maximization algorithms:** These algorithms are now the preferred method of reconstruction. It is a better noise profile and resistance to the streak artifacts common with FBP, but it has higher computer resource requirements than the FBP. It requires the projection matrix specification to link unobserved images to the observed projection counts.

There are two approaches to reconstruct data from PET scanner: (1) Treat each ring as a separate entity, so that only coincidences within a ring are detected, and the image from each ring can then be reconstructed individually (2D reconstruction). (2) Allow coincidences to be detected between and within rings, then reconstruct the entire volume together.

3D techniques have better sensitivity because more coincidences are detected and used, and therefore less noise, but are more sensitive to the effects of scatter and random coincidences, as well as requiring correspondingly greater computer resources [23].

The image reconstruction process is influenced by several features such as the Signal to Noise Ratio (SNR) which is due to many variables including radio, time tissue attenuation, gamma camera sensitivity and others; Contrast to Noise Ratio (CNR) is also a feature which affect to an image reconstruction process. Partial resolution is the last feature; it is due to the distance travelled by positron, the ring diameter and the crystal sizes.

2.4. Visualization and Analysis Software Applications

Many applications and software's can be used for analyzing the proposed system. This section discusses a number of utilities used to visualize and analyze the medical image datasets considered in this research for segmentation and acceleration.

2.4.1. MATLAB

MATLAB® is a numerical computing environment and a fourth-generation programming language developed by MathWorks; MATLAB® allows matrix manipulations, plotting of functions and data, implementation of algorithms, creation of user interfaces, and interfacing with programs written in other languages.

MATLAB® was created in the late 1970s by Cleve Moler, the chairman of the computer science department at the University of New Mexico [28]. He designed it to give his students access to LINPACK and EISPACK without having to learn Fortran. It soon spread to other universities and found a strong audience within the applied mathematics community. In 1983 MATLAB® has been written in C and MathWorks has been founded in 1984. These rewritten libraries were known as JACKPAC. In 2000, MATLAB® was rewritten to use a newer set of libraries for matrix manipulation (LAPACK) [29].

In 2004, MATLAB® had around one million users across industry and academia [30]. MATLAB® users come from various backgrounds of engineering, science, and economics, MATLAB® is widely used in academic and research institutions as well as industrial enterprises.

Matlab® has been used in this research for analyzing the data input or the medical images. A lot of built in functions for digital image processing are available with Matlab® especially in the latest versions after 2007. Matlab® digital image processing toolbox is able to perform a large various image processing tasks, and Digital Imaging and Communications in Medicine images (DICOM) can be analyzed without any conversion to other extensions. Therefore, Matlab® can be considered as one of the best programs that have been used for medical imaging.

Matlab® facilitate the process of analyzing achieved results from the implemented techniques in this thesis. The proposed medical image segmentation system has been implemented using simple Matlab® instruction and validated using the toolboxes included in Matlab®.

2.4.2. Amide

AMIDE stands for Amide's a Medical Image Data Examiner. This program is a tool for viewing and analyzing volumetric medical imaging data sets, and has been designed from the ground up with support for multi-modality imaging. Amide is a powerful freeware visualization tool which is able to convert medical images from many scanner specific image formats into analyze. The most important property in Amide program is the ability of showing the three main orthogonal views for any dataset from any acquisition system.

An important thing to realize when working with AMIDE is that the program will try to abstract away the underlying digital format of the data as much as possible. AMIDE presents the digital data to you in analog format so that you do not have to worry about the underlying digital format. Whenever possible, units are given in terms of real world units (e.g. mm's, seconds), and most operations are not constrained by the discrete nature of the underlying data. For example, data in AMIDE is viewed in terms of "slices", not fixed image planes. These slices can be taken from the data set at arbitary angles, and can be of any thickness (they are not constrained to be integer multiples of the underlying voxel size). You may be used to looking at medical images in terms of voxels and integers, but remember that the object or subject scanned is an item in the real world, and AMIDE tries to recreate this analog signal for you.

Amide provides a tree view of the study data; this is located on the left side of the window which is listing all the objects in the study (Fig. 2.8). The tree structure shows how movements will be propogated to other objects in the study. For instance, if a data set is rotated, all of its children will be correspondingly rotated.

Objects in the tree can be selected for display by left clicking on the name of the object. Middle clicking on a data set will make that data set the active data set. The active data set is designated by being highlights, and when a function is chosen that can logically apply to only one data set.

Object modification dialog boxes can be brought up by right clicking on the corresponding object. ROI's can be added by right clicking on the blank area of the tree, or shift-right clicking on one of the objects. Further information about the Amide software tool for multimodality medical image analysis can be found in [31].

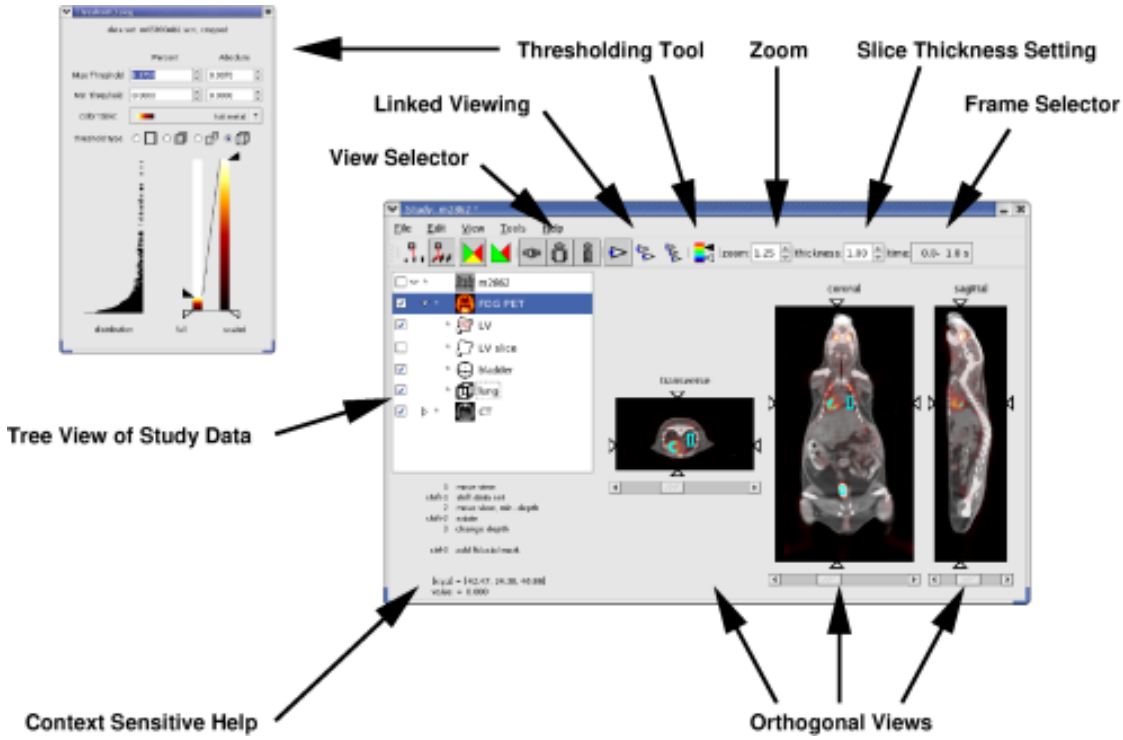

Fig. 2.6: Amide main window components [31]

2.5. Summary

The work presented in this chapter is an overview of modern medical image acquiring machines and utilities for visualizing and analyzing the output of these machines. The process of generating medical data from the medical image acquiring systems has been explained and the software applications used in this thesis research to analyze and validate the system have been introduced.

Chapter 3

Review of Related Literature

3.1. Introduction

The aim of this chapter is to provide a summary of the recent methodologies employed for medical image segmentation, although focusing on the literature related to imagery with medical significance. In some sections it has been necessary to introduce work which has not been applied within this context. This work has been used in other applications but will be employed in this thesis as medical image segmentation methods.

In section 3.2, techniques used for medical image segmentation have been summarized, and used in this thesis to evaluate the proposed system performance, this include a review of work utilizing thresholding, clustering methods, Markov random field models and multiscale techniques. In section 3.3, reviews of related literature of the proposed techniques in similar segmentation systems and some other systems have been presented. Section 3.4 introduces the procedures of measuring the implemented techniques performance. Summary is given in section 3.5.

3.2. Volumetric medical image segmentation

Several techniques which have been used previously with medical image segmentation are introduced in this section.

3.2.1. Thresholding

Thresholding is the simplest method of image segmentation. From a grey scale image, thresholding can be used to create binary images [32], scalar images can be segmented using thresholding approaches by partitioning image intensities. This methodology attempts to determine an intensity value that can separate the signal into a desired number of classes. Segmented images can be achieved by classifying all pixels with intensities larger than the threshold value into one class, and all others into another.

In many applications, the threshold values selection can be done depending on the histogram. Multi-thresholding occurs when more than one threshold value are determined [33]. During thresholding process, individual pixels in an image are marked as “object” pixels if their value is greater than the threshold value (assuming an object to be brighter than the background), otherwise; as background pixels (this convention known as threshold above). Variants which include threshold below is opposite of threshold above [32].

Hard thresholding technique is a boolean filter [33]; it is the simplest precursory technique for image segmentation. This methodology attempts to determine an intensity value that can separate the image $g(x,y)$ into two parts [34]. All pixels with intensities $f(x,y)$ larger than the

threshold value *T* are allocated into one class, and all others into another class. As illustrated in equation (3.1), applying hard thresholding technique on an image either resets the input to zero or keeps it without any changes [35].

$$g(x,y) = \begin{cases} f(x,y) \; if \;\; f(x,y \geq \;\; T) \\ 0 \qquad\quad if \;\; f(x,y < \;\; T) \end{cases} \tag{3.1}$$

Hard thresholding process is less complex than soft thresholding (equation 3.2), where pixels that have values greater than threshold value do not change in hard thresholding [36]. Soft thresholding replaces each pixel which has greater value than the threshold value by the difference between the threshold value and pixel value, and adds the sine of the pixel value [33]. This makes the process more complicated and increases the processing time for the algorithm. Fig. 3.1 illustrates a segmented medical brain slice from an MRI scanner using hard and soft thresholding techniques.

$$g(x,y) = \begin{cases} |f(x,y)| - t + sin\, f(x,y) \; if \; f(x,y) \geq t \\ 0 \; if \; f(x,y) < t \end{cases} \text{, t: is the threshold value} \tag{3.2}$$

Fig. 3.1: Thresholding technique for medical image segmentation at threshold value t = 180. (a) Original image, (b) Hard thresholding and (c) Soft thresholding.

Thresholding is called adaptive thresholding when a different threshold is used for different regions in the image. This may also be known as local or dynamic thresholding [33]. The key parameter in thresholding process is the choice of threshold values. Several methods for choosing a threshold exist; users can manually choose a threshold, or a thresholding algorithm can compute a value automatically, which is known as *automatic thresholding* [33].

Mean or median value would be also used for a simple thresholding method, for example, if the object pixels are brighter than the background, they should also be brighter than the average. In a noiseless image with uniform background and object values, the mean or median will work well, however, this will generally not be the case. A more sophisticated approach might be to create a histogram of the image pixel intensities and use the valley point as the thresholds. The histogram approach assumes that there is some average value for the background and object pixels, but that the actual pixel values have some variation around these average values. This may be computationally expensive, and image histograms may not have clearly defined valley points, often making the selection of an accurate threshold difficult.

There are many adaptive thresholding techniques; one of them can be applied when the pixels comprising ROI is darker than the average value of all pixels or the background pixels values, in this case inverse thresholding is the suitable adaptive thresholding [35][37]. Inverse thresholding reset pixels with values greater than the threshold value and illustrate the rest, this pixels are above the threshold value and may comprise ROI.

Sezgin and Sankur categorize thresholding methods into different groups based on the information manipulated from the algorithm [37]. Some of them are listed below:

- Histogram shape-based methods, for example, the peaks, valleys and curvatures of the smoothed histogram are analyzed
- Clustering-based methods, where the gray-level samples are clustered in two parts as background and foreground, or alternately are modeled as a mixture of two Gaussians.
- Object attribute-based methods search a measure of similarity between the gray-level and the binarized images, such as fuzzy shape similarity and edge coincidence.

Significant recent work used thresholding in medical imaging field, it was performed by a research group in the ***Departments of Radiation Oncology, Medical Physics and Nuclear Medicine, Cross Cancer Institute, Edmonton, Alberta, Canada*** [38][39]. These studies investigate the affect of threshold size on the segmentation and quantification of simulated tumours in PET scanners, for the staging and radiotherapy treatment planning of non-small-cell lung cancer. The segmented Phantom PET imagery regions are referenced to known volumes; this is quantitatively illustrate the influence of threshold, tumour size and background concentration in this application. The results from these studies are summarized in Fig. 3.2, where a dimensionless volume of 1.0 represents the ideal image target volume for a set of seven spheres of increasing size (sphere 1 has the smallest volume), and image threshold represents a percentage of the total image bit-depth. Results show that higher image thresholds are required to accurately render the smallest simulated tumours. Similar work was performed by another group from ***Universities Catholique de Louvain*** [40].

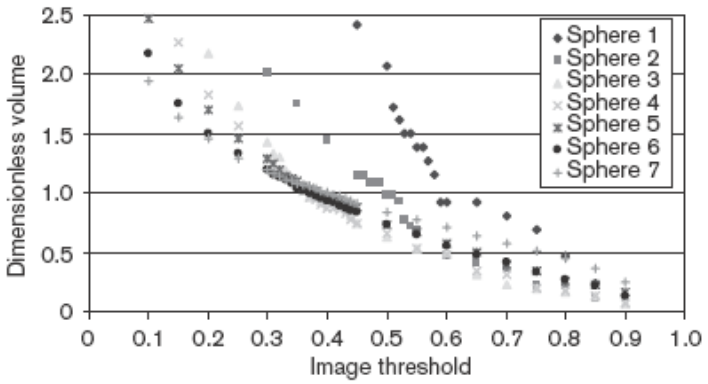

Fig. 3.2: Variation of dimensionless volume with image threshold and spherical tumour diameter [1][38].

The voxels of a certain object are not necessarily connected after thresholding because this technique does not consider the spatial characteristics of an image, thus causing it to be sensitive to noise and intensity fluctuations [41]. This means that the results are coupled too tightly with the thresholds used, where any change can completely alter the result of the segmentation. Furthermore, thresholding does not consider the spatial characteristics of an image, thus causing it to be sensitive to noise and intensity fluctuations. For this reason it cannot be easily applied to many medical imaging modalities. These drawbacks essentially corrupt the histogram of the image-making partitioning via the selection of more problematic appropriate thresholds [41].

Applying thresholding techniques is a very easy process and can be affected easily by surrounding noise. Thresholding techniques are often used as a preliminary step in computer vision systems. They have also been used in cardiac MRI tissue classification and in digital mammography [42][43][44]. Thresholding techniques have been used as pre-processing step and/or post-processing step with other segmentation techniques in this thesis.

3.2.2. Clustering

Clustering is essentially the process of organizing objects into groups according to their properties without the need of training data [1]. Clustering process classifies each group of pixels in an image into one class which has the same or similar properties; this class evaluates a specific part of an image [45]. Each class is highlighted in the segmented image to illustrate the image as a number of separated regions; ROI may be one of those regions.

Clustering overcomes the use of training data by iteratively alternating between segmenting the volume and characterizing the properties of each class, effectively training using the available data [35][45]. Clustering technique is based on multi-threshold values which can be set depending on the image histogram. *Amira et al*. used *K*-means method for segmenting medical volumes [34]; it is one of the most commonly used clustering procedures. *K*-means is also known as the ISODATA algorithm.

K-means clustering classifies *n* voxels into *K* clusters or classes (*number of clusters used to be much smaller than number of voxels*) [34]. This algorithm chooses the number of clusters (*K*) then randomly generates *K* clusters and determine the cluster centres. The next step is assigning each point in the volume to the nearest cluster centre and finally the new cluster centres recomputed. The two previous steps are repeated until the minimum variance criterion is achieved [34]. This approach is similar to the expectation maximization algorithm for Gaussian mixture in which they both attempt to find the centres of clusters in the volume. Its main objective is to achieve a minimum intra-cluster variance *V* which can be calculated according to the following equation:

$$V = \sum_{i=1}^{K} \sum_{x_j \in S_i} (x_j - \mu_i)^2 \qquad (3.3)$$

where *K* is the number of clusters, *S* = *1, 2, . . . K*, x_j is the pixels values and μ_i is the mean of all voxels in cluster *i*. Fig. 3.3 illustrates an example of segmenting a real CT slice by classifying the image into 6 different classes.

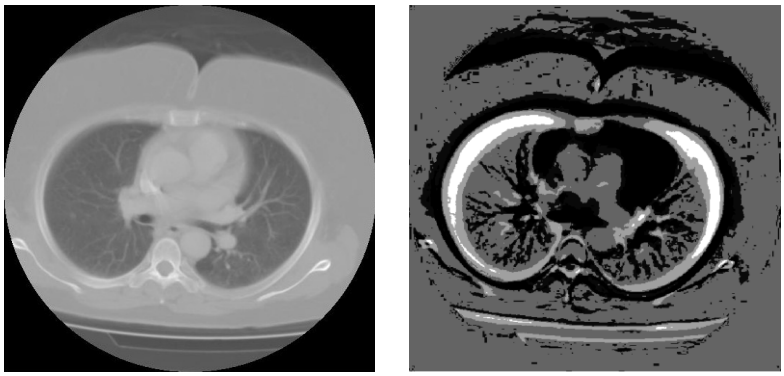

Original image Clustered image

Fig. 3.3: Image segmentation using classification technique.

There are some well known clustering procedures such as: fuzzy *C*-means clustering [46] and the Expectation Maximization (EM) algorithm [47][48][49]. Using fuzzy set theory, the *K*-means algorithm is generalized to allow for softer segmentation [50]. It is used also for MRI segmentation in the presence of intensity inhomogeneity [51]. The EM algorithm applies clustering principles under the assumption that the data follows a mixture of probability distributions, usually Gaussian. This approach alternates between the computation of

posterior probabilities and maximum likelihood estimates of specific statistical characteristics, such as the means and variances associated with the mixture model [47].

In this field, important research has been carried out by collaboration between ***The Departments of Biomedical Engineering and Information Technology, Helsinki University of Technology***, *and* ***Helsinki University Central Hospital, Finland*** [48]. The collaborators developed a contextual real segmentation system for functional Magnetic Resonance Imagery (fMRI) activated areas detection and segmentation using clustering techniques. This requires the computation of a Statistical Parametric Map (SPM) for the data. If the SPM value associated with a particular voxel adjusted to consider some spatial information, or differs from the expected non-activation value by more than a specific decision value; the algorithm places the voxel into the activation class. This two region segmentation algorithm uses the two class Iterated Conditional Modes (ICM) algorithm for spatial modeling. It is able to detect extremely small activation areas while it detects activations with higher probability than other thresholding techniques.

It is necessary with clustering to set an initial segmentation and to initiate the parameters. This means that the process is manual and requires a lot of preprocessing steps. Clustering algorithms do not directly support spatial modeling. Therefore, it is so sensitive to noise and spatial information loss. Clustering algorithms have one big disadvantage where the information about the neighbouring voxels is not involved in the clustering process. Therefore, the segmentation output neither accurate nor qualitative enough.

3.2.3. Markov Random Field Models

A Markov Random Field Model (MRFM) is a statistical approach that can be utilized within segmentation methodologies to model spatial interactions between nearby pixels. These local correlations between pixels are used as a mechanism for modeling various image properties. From a medical imaging perspective, this kind of analysis is useful as most pixels can be categorized into the same class as their neighbours. It is unlikely that any anatomical structure consists of only one pixel under MRFM assumptions [1].

As a MRFM is not specifically a segmentation method, it is often incorporated into other segmentation systems such as the *K*-means or fuzzy *C*-means algorithms under a Bayesian prior model [1]. Given the image data, the segmentation is achieved by maximizing the posteriori probability of the segmentation, obtained using iterative methods such as ICM or simulated annealing [1].

A recent work utilizing this statistical methodology for medical image segmentation has been done in ***The Department of Medical Image Computing, University Hospital Gasthuisberg, Leuven, Belgium*** [53]. A system based on previous research into tissue segmentation from MR brain imagery was developed to overcome the problem of partial volume voxels that contain a mixture of two or more tissue types [54]. A modified version of the EM is introduced to allow partial volume segmentation along the borders between tissues. Spatial interactions are then considered by applying a MRFM. The system is tested on both real and simulated data. Results obtained are promising; however, the group concludes that general robust partial volume segmentation of brain MRI requires statistical

models that describe the spatial distribution of brain tissues more accurately than currently available methodologies. An illustration of partial volume classification is given in Fig. 3.4.

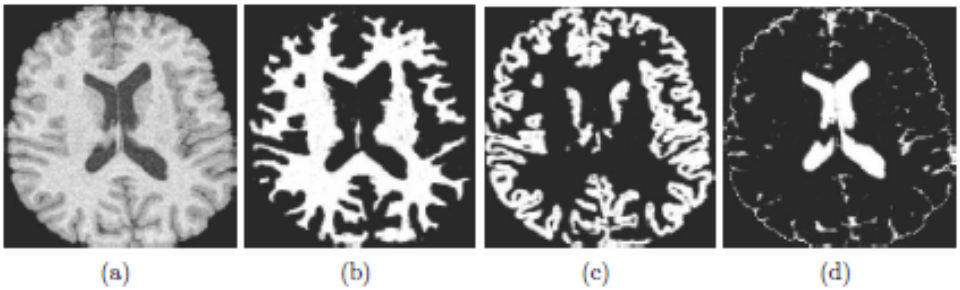

Fig. 3.4: Partial volume segmentation of a high resolution brain MRI. (a) Input data, (b) expected fraction of white matter, (c) grey matter, and (d) cerebrospinal fluid [1].

Problems associated with a MRFM include the accurate selection of the parameters controlling the strength of spatial interactions. Incorrect selection of this parameter may result in a loss of important structural detail and an excessively smooth segmentation. In a medical imaging context, the loss of anatomical detail is possible and areas of diagnostic significance may be incorrectly represented. Furthermore, these approaches typically require computationally intensive algorithms, and estimating the parameters is so difficult. Resulting segmentations obtained using this methodology are robust to noise and do not exhibit many disconnected regions which are apparent using non Markovian approaches.

3.2.4. Multiscale Segmentation

The use of wavelet or multiresolution theory can be used alongside segmentation approaches creating new systems which can provide a segmentation of superior quality to those segmentation approaches computed exclusively within the spatial domain [1].

Wavelet theory which is built on solid mathematical fundamentals uses well established tools such as quadrature mirror filtering, subband coding and pyramidal image processing. One of the most significant breakthroughs in this field occurred in the late 1980's when Mallat employed wavelet theory for multiresolution analysis [55]. This analysis enables the exploitation of signal or image characteristics associated with a particular resolution level, which may not be detected using other analysis techniques [1].

The use of wavelet theory in the segmentation field of biomedical imagery is utilized by collaboration between ***Faculty of Computing Sciences and Engineering, De Montfort University, Leicester, UK*** and ***Department of Computer Science, University of Warwick, Coventry, U.K*** [56]. An algorithm was developed for the unsupervised segmentation of hyperspectral cellular colon tissue images into regions associated with normal tissue cells and malignant cancerous tissue cells. The system works by utilizing a modified version of the standard wavelet texture analysis system. This is applied to the projection of the image data in the first principal component direction, to reduce the dimensionality of the hyperspectral imagery. The wavelet transform is effective in identifying different textures [57]. An image decomposed into its corresponding wavelet representation can present a variety of textures within the different decomposition subbands.

Multiscale methodologies are also employed for the segmentation of imagery with no medical significance. Interesting and important research has been accomplished by ***Image Communications Group, Centre for Communications Research, University of Bristol, UK***. *Hill et al.* investigate the use of the watershed transform for image segmentation [58]. As this transform is ineffective for the segmentation of textured image regions, a texture gradient is employed to alleviate this problem. Texture information is determined using a

Non-Decimated compleX Wavelet Packet Transform (NDXWPT). A marker algorithm is used in conjunction with the gradient image obtained to locate significant homogeneous textured or non-textured regions. These markers are used for the application of the watershed transform. In this system, a parameter minsize controls the levels of segmentation within an image and a suitably large value reduces the likelihood of over-segmentation. Some illustrations of this approach are shown in Fig. 3.5. The combined system, developed for content based image retrieval, provides effective texture and intensity based image segmentation. The results achieved using this system are contrasted with results obtained using the open source JSEG algorithm, developed at the ***University of California, Santa Barbara***. JSEG is an algorithm which separates the segmentation process into colour quantization and spatial segmentation. In the former, colours in the image are quantized to several representing classes which can be used for region differentiation [58]. A class map of the image is then formed by replacing image pixel colours with their corresponding colour class labels. The system proposes a criterion for good quality using the class map.

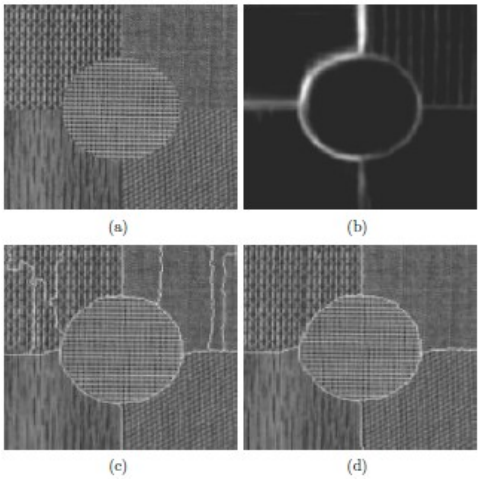

Fig. 3.5: (a) Original Image, (b) texture gradient of image, (c) segmented image using minsize = 300, and (d) segmented image using minsize = 1500 [1].

Although the wavelet based approaches proves promising results in many applications including image processing and segmentation, it is somewhat limited, it produces good results only when the derived first principal component projection covers more than 80% of the data variance. As well as there is a slow down for the segmentation process; ROI can be detected in any of the four wavelet quadrants at each decomposition level. The quadrant selection process is manual and could not be generalized as different quadrant perform better than the other with each specific data.

The most important problem with using wavelet transform for medical image segmentation is the point singularity property. Applying wavelet transform on images detects point of discontinuity accurately, but images and especially medical images contain higher dimensional singularities that wavelets fail to detect such as ridges (straight lines) and/or curves. Therefore, the wavelet transform is limited to be generalized as an accurate medical image segmentation technique.

3.3. Proposed Techniques Literature

In this section, the previous work related to the techniques used in the proposed system is introduced. This is not limited to the work implemented for medical applications; some other implementation of the proposed techniques for non medical applications is included.

3.3.1. Hidden Markov Models

A Hidden Markov Model (HMM) is a statistical model in which the system being modeled is assumed to be a Markov process with unobserved states [59].

In a regular Markov model, the state is directly visible to the observer, and therefore the state transition probabilities are the only parameters. In a hidden Markov model, the state is not directly visible, but the dependent state output is visible. Each state has a probability distribution over the possible output tokens. Therefore the sequence of tokens generated by an HMM gives some information about the sequence of states. Note that the adjective *hidden* refers to the state sequence through which the model passes, not to the parameters of the model; the model is still hidden even if the model parameters are known.

HMMs are used to characterize the statistical properties of a signal. They have been used successfully in speech and face recognition for a number of decades and are now being applied to medical imaging. The following is a list of some research teams who used HMMs in their systems:

Group [I] **A collaboration between "*Language and Media Processing Laboratory, University of Maryland, College Park, MD – USA*" and "*CUI - University of Geneva, Computer Science Department, Geneva – Switzerland*"** [60].

The main goal that the collaborators were working on is addressing the problem of constructing statistical models of images using HMMs developed in speech recognition. In

other words, how speech recognition techniques can be extended to image processing. They describe a method for learning statistical models of images using a second order hidden Markov mesh model. First, an image can be segmented in a way that best matches its statistical model by an approach related to the dynamic programming used for segmenting Markov chains. Second, given image segmentation, a statistical model (3D state transition matrix and observation distributions within states) can be estimated. These two steps are repeated until convergence to provide both segmentation and a statistical model of the image.

The collaborators also describe a semi Markov modeling technique, in which the distributions of widths and heights of segmented regions are modeled explicitly by gamma distributions in a way related to explicit duration modeling in HMMs. They propose a statistical distance measure between images based on the similarity of their statistical models for classification and retrieval tasks. The problem of learning their model of a given image is solved by putting the Viterbi algorithm and the probability estimations in an iteration loop [60]. The description of training method for acquiring statistical models of images using a hidden second order Markov mesh model was this collaborators main contribution.

Group [II] **A research team in "*College of Computer and Communication, Hunan University, Changsha - China*"** [61].

Recent researches have demonstrated the strong performance of HMMs applied to information extraction, the task of populating database slots with corresponding phrases from text documents [61]. It is well known that the training data coming from different

sources is probably different in their formats, although their contents are similar. In the previous information extraction researches, all the training data is mixed together to learn HMM parameters. But the training data as a whole is multi-component, and it is difficult for using statistical learning technique to find optimal model parameters [61].

This team presented in their work a new algorithm using HMM for information extraction based on multiple templates, which first clusters the training data into multiple templates based on the format, then learns model structure parameters from the clustered training data and model emission probability parameters from the initial training data.

Group [III] A collaboration between "*Dipartimento di Scienze Statistiche, Università Cattolica SC, Milano - Italy"* and *"Biomathematics & Statistics Scotland, Macaulay Institute, Aberdeen - UK*" [57].

Paroli and Spezia mentioned in [57] that the main problem in their segmentation research consists in estimating the unobserved realizations from the observed ones, given that parameters of the conditional distributions, which they assume to be Gaussian, are rising to Gaussian HMMs (GHMMs).

They apply their Bayesian inference and segmentation tools to digital images. Complex stochastic image segmenters are based on HMMs, which have the drawback of the cumbersome computation of the normalizing constant of the Gibbs density. Computational advantages can be obtained by replacing the hidden Markov random field with a hidden Markov chain, by transforming the 2D MRFM into 1D Markov chain through a Peano-Hilbert scan of the image; the segmented 2D image is then reconstructed by using

an inverse Peano-Hilbert scan. HMMs can cluster efficiently the observations, even when the number of groups is unknown and no classification threshold is fixed, this can be done by segmenting a sequence of pixel intensities

The collaborators made experiments on square synthetic images of size 128×128 pixels with two, three and four colours. By the Peano-Hilbert scan, the 2D image is transformed into a 1D image, and then pixel intensities are standardized. To validate the performances of the HMM, they make comparisons between any segmented image with the corresponding synthetic hidden image created for the various experiments.

3.3.2. Ridgelet Transform

In 1998, Donoho introduced the ridgelet transform [62]; Continuous Ridgelet Transform (CRT) can be defined from a 1D wavelet function oriented at constant lines and radial directions. Ridgelet transforms have been generating a lot of interest due to their superior performance over wavelets, while wavelets have been very successful in applications such as denoising and compact approximations of images containing zero dimensionalities.

In dimensions two or higher, wavelets can efficiently represent only a small range of the full diversity of interesting behavior. In effect, wavelets are well adapted for point discontinuity phenomena, whereas in dimensions greater than one, interesting phenomena can be organized along lines, hyper dimensions and other non point discontinuity structures for which wavelets are poorly adapted. Ridgelet analysis can effectively deal with line discontinuity phenomena in two dimensions. It encompasses a collection of tools which all

begin from the idea of analysis by ridge functions, which is based on the concepts of applying wavelet in the Radon domain.

Ridgelet transform has been used in many applications including image processing, a research team in ***Key Lab for Radar Signal Processing, Xidian University, Xi'an - China*** used ridgelet transformation to implement their imaging systems [63]. Linear feature detection is very important in image processing. The detection efficiency will directly affect the performance of pattern recognition and pattern classification. Based on the idea of ridgelet, this team presents a new discrete localized ridgelet transform and a new method for detecting linear feature in anisotropic images. They did some experiments to prove the efficiency of their proposed method.

For a straight line in an image, the group has been used Radon transform and Haar wavelet transform to implement ridgelet [63]. But for a curve, the detection algorithm is very complicated. Ridgelet is just a new analysis tool to answer some of the fundamental questions, such as the efficient approximation of objects with two- or higher-dimensional singularity. Ridgelet describes general functions as a superposition of ridge functions in a stable and concrete way. This team advanced a new localized ridgelet transform combined with dyadic wavelet transform to detect linear feature in an image in the frame of ridgelet analysis.

The team applied the new method to three images illustrated in Fig. 3.6: a basic straight line, a noisy V-shaped linear feature and a real image with linear feature. It can be seen from the corresponding experiment results (Fig. 3.7) that the line segments can be efficiently detected, and these segments are not integrated into a straight line, but the directions of the segments are similar or consistent; furthermore, the total length of these

segments is less than or equal to the length of the original straight line. The positions of the lines and the length of the lines which is the sum of every segment can be located and computed respectively hence an anisotropic image with distinct linear feature is given. Moreover, those parameters can be obtained at one time in this team proposed algorithm. Their experimental results showed that the new transform is more effective than its classical counterpart. This new implemented technique cannot be generalized on all images including medical images, as the curves in medical images are so tight and lacks to the ridges which are the best case for ridgelet transform.

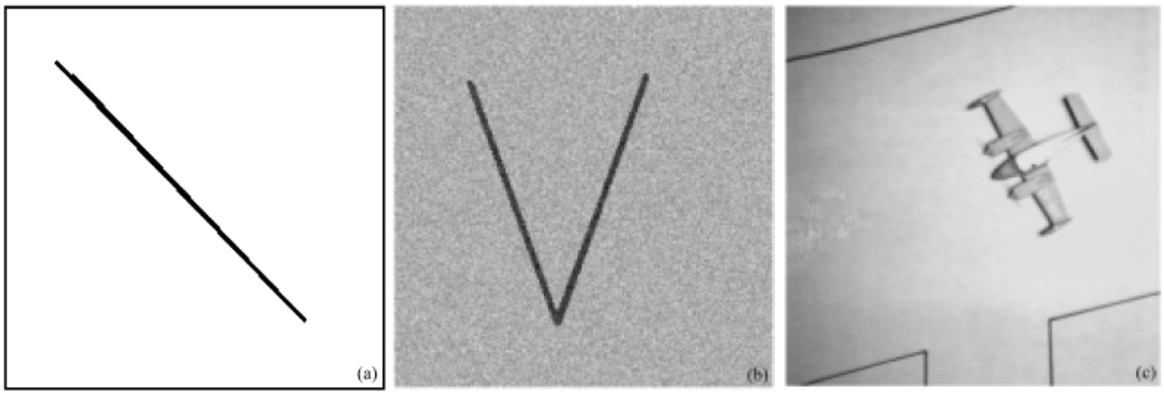

Fig. 3.6: (a) The basic straight line; (b) the noisy V-shaped linear; (c) the real image with linear feature [63].

Fig. 3.7: (a) Detection result of fig. 3.6 (a); (b) Detection result of fig.3. 6(b); (c) Detection result of fig. 3.6(c) [63].

In the field of image segmentation, a research team in the ***College of Electronic Engineering, Northwestern Polytechnical University Xi'an City, Shaanxi Province P. R. - China*** implemented such system [64]. This group implemented a new finite ridgelet transform based on the natural straight line, which can overcome the ridgelet drawback due to annoying wrap-around effect to the Finite Radon Transform (FRAT), and implement the Inverse Discrete Radon Transform (IDRT). The group employed the proposed algorithm for segmenting the Synthetic Aperture Radar (SAR) images and obtained satisfied segmentation result [64].

Due to the large noise in SAR images, it is necessary for eliminating the speckle when carrying out edge detection and segmentation. But this step will commonly depress the resolution of image. Otherwise, the optimally multi-resolution segmentation of AFRIT method does not need to eliminate noise when detection and segmentation, and it show obvious effect on extraction of objects with geometrical structure. Fig. 3.8 shows the results obtained by the method implemented by this group for SAR image segmentation.

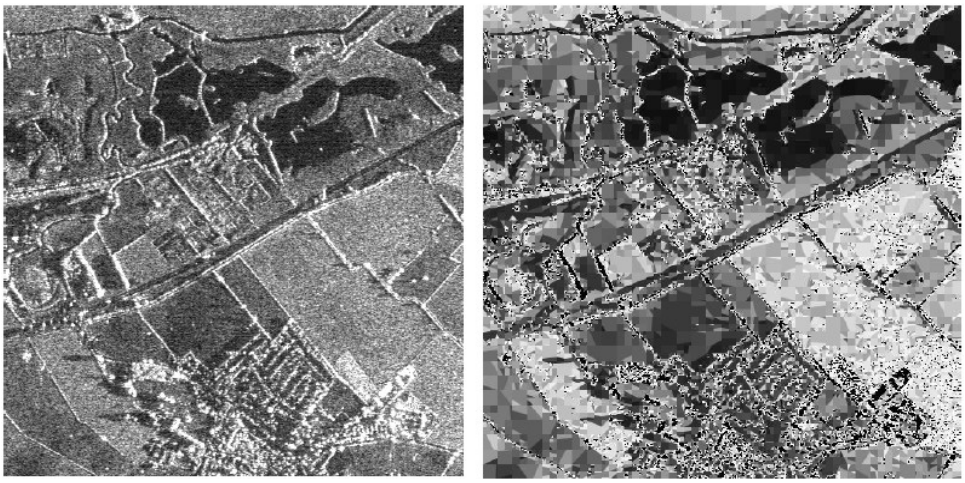

(a) Original image (b) Result of AFRIT segmentation

Fig. 3.8: Segmentation of SAR image using AFRIT method [64]

3.4. Segmentation Performance

Many techniques have been implemented worldwide for the purpose of medical image segmentation, and many methods have been used to utilize those techniques. In this section, some of the performance measurements methods that have been used in this thesis to validate the proposed techniques for real clinical applications are listed.

3.4.1. Computational Time

One of the main limitations of many medical image segmentation systems is the processing time. The time required to compile the segmentation techniques varies and not the same for all techniques. Considering the important movements toward real time systems; less computational time or processing time in the segmentation system will be much better to achieve this. In the implemented system case, real time processing may offer a straight away delivery of the patient results while he is waiting.

Computational time is the time required to segment the data inputs (or medical images), it is the time between acquiring this data from the scanner machine (PET, CT or MRI) until it will be illustrated segmented on the output screen. This can be calculated in the proposed system by capturing the exact time at the beginning and the end of each technique segmentation code, then subtract those times from each other after process completion.

3.4.2. Euclidean Distance

Euclidean Distance (ED) is the straight line distance between two single points. It can be used within the proposed system to validate results acquired for the predefined datasets. For example, the biggest ED between two points located on the edge of a sphere is the diameter of that sphere. It can be used with the real clinical data to quantify the cancer volume or the dimensionalities of ROI [65]. Equation 3.4 illustrates how to compute the distance between two pixels in medical volumes, given the coordinates in X, Y and Z planes.

$$ED = \sqrt{(x_2 - x_1)^2 + (y_2 - y_1)^2 + (z_2 - z_1)^2} \quad (3.4)$$

3.4.3. Dice Similarity Coefficients

Dice Similarity Coefficient (DSC) is a statistical validation metric used to evaluate the performance of both the reproducibility of manual segmentations and the spatial overlap accuracy of automated probabilistic fractional segmentation. The DSC value is a simple and useful summary measure of spatial overlap, which can be applied to studies of reproducibility and accuracy in image segmentation.

The value of a DSC varies from 0 indicating no spatial overlap between two sets of binary segmentation results to 1 indicating complete overlap [66]. As illustrated in Fig. 3.9, DSC measures the spatial overlap between two samples target regions (A and B). DSC value can be calculated as illustrated in equation (3.5), where ∩ is the intersection.

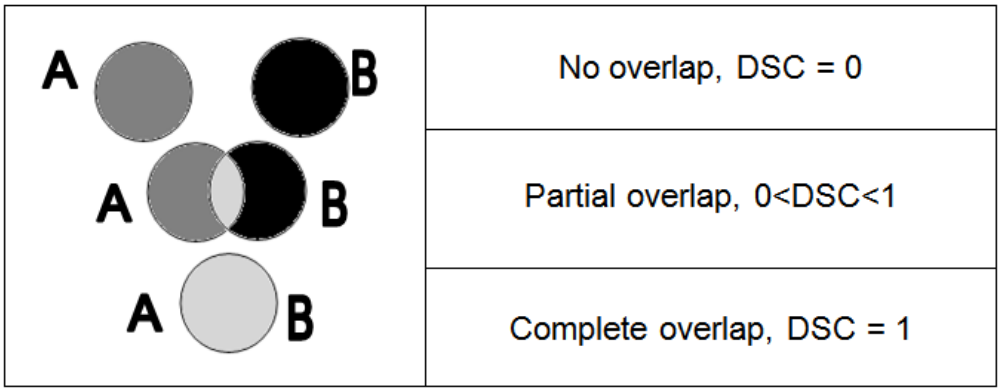

Fig. 3.9: DSC overlapping [64].

$$DSC\ (A,B) = 2 \times \frac{A \cap B}{A+B} \qquad (3.5)$$

3.4.4. Peak Signal to Noise Ratio

Signal to Noise Ratio (SNR) is also used to differentiate between the qualities of the proposed techniques. SNR is used in image processing as a physical measure of the sensitivity of an imaging system. Industry standards measure SNR in Decibels (dB) of power, and therefore apply the *20 log* rule to the peak SNR (PSNR) [67]. They measure and define sensitivity in terms of the ISO film speed equivalent; image quality is excellent when PSNR is 32 dB and if PSNR is 20 dB means acceptable image quality [67].

In this thesis PSNR has been used to measure the performance of some predefined real clinical data and proposed phantom data, it is mostly utilized in the eighth chapter of this thesis to validate the PET scanners sensitivity to its parameters and generalize them for medical image segmentation applications.

3.4.5. Mean Square Error

In statistics, Mean Square Error (MSE) of an estimator is one of many ways to quantify the difference between an estimator and the true value of the quantity being estimated. MSE measures the average of the square of the error. The error is the amount by which the estimator differs from the quantity to be estimated [68]. The MSE incorporates both the variance of the estimator and its bias. The MSE is equal to the sum of the variance and the squared bias of the estimator as illustrated in equation (3.4).

$$MSE(\hat{\theta}) = Var(\hat{\theta}) + (Bias(\hat{\theta}, \theta))^2 \quad (3.4)$$

where Var is the variance function and $Bias$ is the difference function between the estimator's expected value ($\hat{\theta}$) and the true value of the parameter being estimated (θ). MSE has been used in this thesis in few locations to measure the quality of the segmented images.

Each single technique mentioned in this chapter has at least one disadvantage, it is hard to find one optimum technique without any limitation. For example, HMMs prove efficient in many applications but require long computational time. This drawback of HMMs is not exist with some of the other techniques such as ridgelet, but ridgelet is so hard to be applied with real clinical medical image segmentation. A lot of curves exist in medical images, and those curves cannot be assumed as a group of ridges because of its small size.

As mentioned before, the main goal of this thesis is to implement a segmentation system which can use more than one of the available segmentation techniques to segment the input data. It is also provide a segmented output with the most accurate results and lossless segmentation. This can be achieved by using the new implemented techniques in this thesis with other available ones to cover each other weaknesses. And to come up with a solid, accurate and complete medical image segmentation system that deliver outputs in least computational time by accelerating the segmentation process using different accelerators.

3.5. Summary

This chapter has presented research utilizing recent techniques for medical imaging. For volumetric segmentation, all techniques are varying in their quality of segmenting medical volumes. Most recent work has focused on the adaptation of multiscale based encoding strategies including wavelet and higher dimensional transforms.

Automatic or semi-automatic segmentation is so important for cancer diagnosis and radiotherapy planning, statistical modeling including HMMs have been introduced in this chapter and will be implemented for the purpose of automatic medical image segmentation in the related chapter in this thesis. Other techniques such as thresholding, which are currently being investigated for PET image segmentation provide little anatomical information and the approach is neither robust to noise nor intensity fluctuations.

Many methods have been employed for medical image segmentation systems. Therefore, not all of the implemented techniques have been mentioned in this chapter. This

chapter covers the popular techniques in the field that have been used to build a strong background of the related literature for this thesis.

Some other algorithms, which have been employed in this thesis in parallel with the segmentation technique have, been implemented to achieve a more accurate system, those algorithms will be explained briefly in the related chapters.

Chapter 4

Multi-Resolution Analysis for Medical Image Segmentation

4.1. Introduction

Multi-Resolution Analysis (MRA) [69][70][71] has been successfully used in image processing specially with image segmentation, wavelet-based features has been used in various applications including: image compression [72], denoising [73], and classification [74]. Recently, finite ridgelet and curvelet transforms have been introduced as higher dimensional MRA tools [75][76].

This chapter is focusing on a robust implementation of MRA techniques to be employed in a medical volumes segmentation system, using features derived from the wavelet, ridgelet, and curvelet transforms of medical images obtained from a medical scanner. The rest of this chapter is as follows: the use of MRA using wavelets, ridgelets and curvelets transforms in the proposed system is illustrated in section 4.2. Sections 4.3, 4.4 and 4.5 describe the wavelet, ridgelet and curvelet transforms rspectively. Experimental

study and analysis for using MRA in medical image segmentation system has been illustrated in section 4.6. Finally, the summary and the discussion are in section 4.7.

4.2. Proposed System for Medical Image Segmentation using MRA

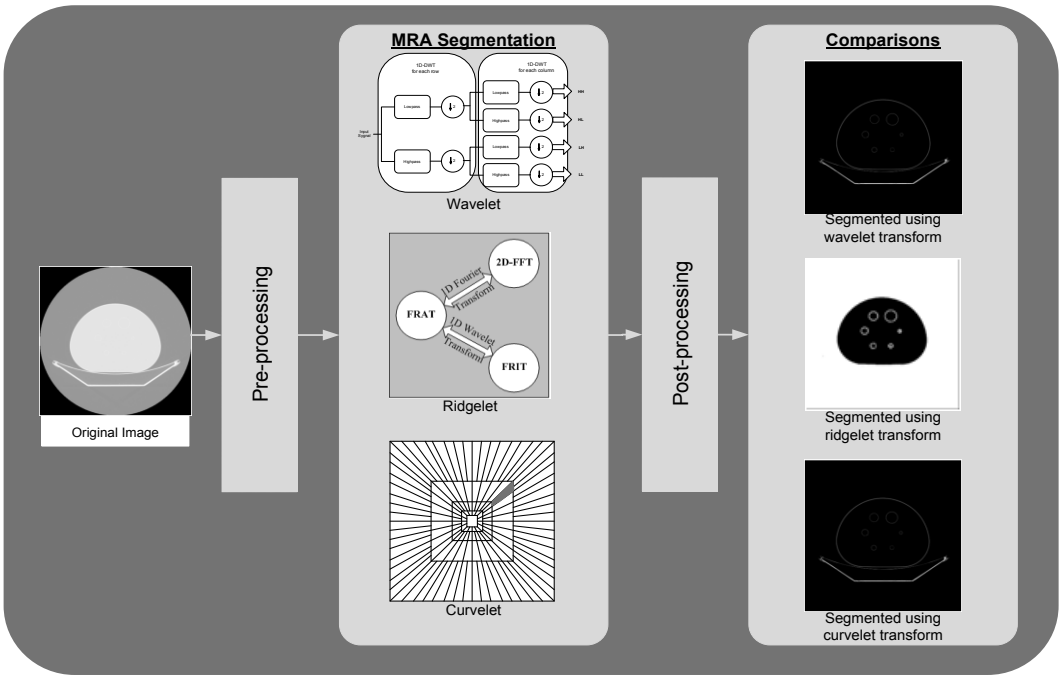

Fig. 4.1: MRA in the proposed medical image segmentation system.

The main aim of this research is to facilitate the process of highlighting ROI in medical images, which may be encapsulated within other objects or surrounded by noise that makes the segmentation process not easy. Fig. 4.1 illustrates the use of MRA in the proposed medical image segmentation system. Wavelet, ridgelet, and curvelet transforms are applied on medical images with other pre and post processing techniques to present segmented outputs and detected ROI in an easier and more accurate way.

4.3. Wavelet Transform

4.3.1. Discrete Wavelet Transform

In the last decade, wavelet transform has been recognized as a powerful tool in a wide range of applications, including image/video processing, numerical analysis, and telecommunication [77]. The advantage of wavelet is that it performs an MRA of a signal with localization in both time and frequency [55][78]. In addition to this, functions with discontinuities and functions with sharp spikes require fewer wavelet basis vectors in the wavelet domain than sine and cosine basis vectors to achieve a comparable approximation.

Wavelet operates by convolving the target function with wavelet kernels to obtain wavelet coefficients representing the contributions in the function at different scales and orientations. Wavelet or multi-resolution theory can be used alongside segmentation approaches, creating new systems which can provide segmentation of superior quality to those segmentation approaches computed exclusively within the spatial domain [56].

Discrete Wavelet Transform (DWT) can be implemented as a set of high-pass and low-pass filter banks. In standard wavelet decomposition, the output from the low-pass filter can be then decomposed further, with the process continuing recursively in this manner. According to [79], DWT can be mathematically expressed by equations (4.1) and (4.2):

$$a^j(n) = \sum_{i=0}^{L-1} l(i).\, a^{j-1}(2n-i), 0 \le n < N_j \qquad (4.1)$$

$$d^j(n) = \sum_{i=0}^{L-1} h(i).\, d^{j-1}(2n-i), 0 \le n < N_j \qquad (4.2)$$

The coefficients $a^j(n)$ and $d^j(n)$ refer to approximation and detailed components in the signal at decomposition level *j* respectively. The *l(i)* and *h(i)* represent the coefficients of low-pass and high-pass filters respectively.

DWT decomposes the signal into a set of resolution-related views. The wavelet decomposition of an image creates at each scale *j* a set of coefficient values *Wj* with an overall mean of zero. *Wj* contains the same number of pixels as the original image; therefore, this wavelet transform is redundant [80][81]. For images, Fig. 4.2 illustrates two different decompositions for transforming 2D matrices.

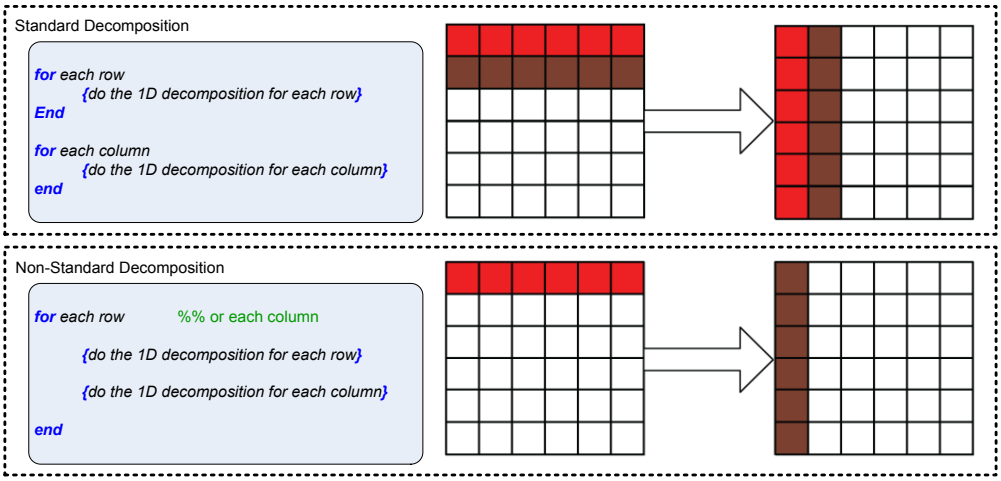

Fig. 4.2: 2D DWT filter decompositions

As illustrated in Fig. 4.2, 1D-DWT can be readily extended into 2D. In standard 2D wavelet decomposition, the image rows are fully decomposed, with the output being fully decomposed columnwise. In nonstandard wavelet decomposition, all the rows are decomposed by one decomposition level followed by one decomposition level of the columns [82][83]. Fig. 4.3 illustrates the filter structure of 2D-DWT.

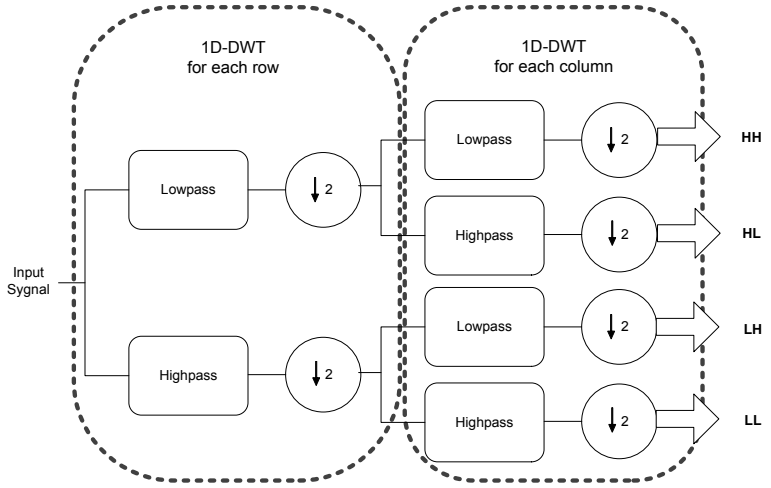

Fig. 4.3: 2D DWT filter structure

4.3.2. Discrete Wavelet Packet Transform

Wavelet Packet (WP) is a wavelet transform where the signal is passed through more filters compared to DWT based approach. Applying DWT or WP on images generates four coefficients; three of them are the detail coefficients and the remaining one is the average coefficient. It is worth mentioning that the first level of decomposition is the same for both DWT and WP. As illustrated in Fig. 4.4 and Fig. 4.5; the differences start being noticed from the second level of decomposition.

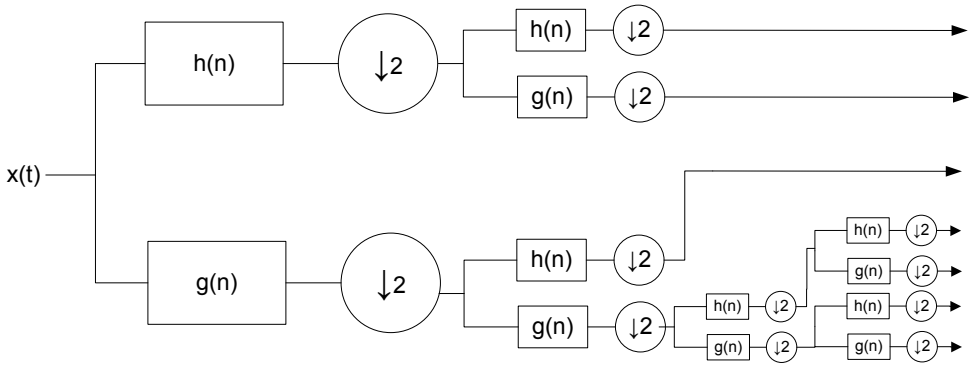

Fig. 4.4: Architecture of basic discrete wavelet filters (2 decomposition levels).

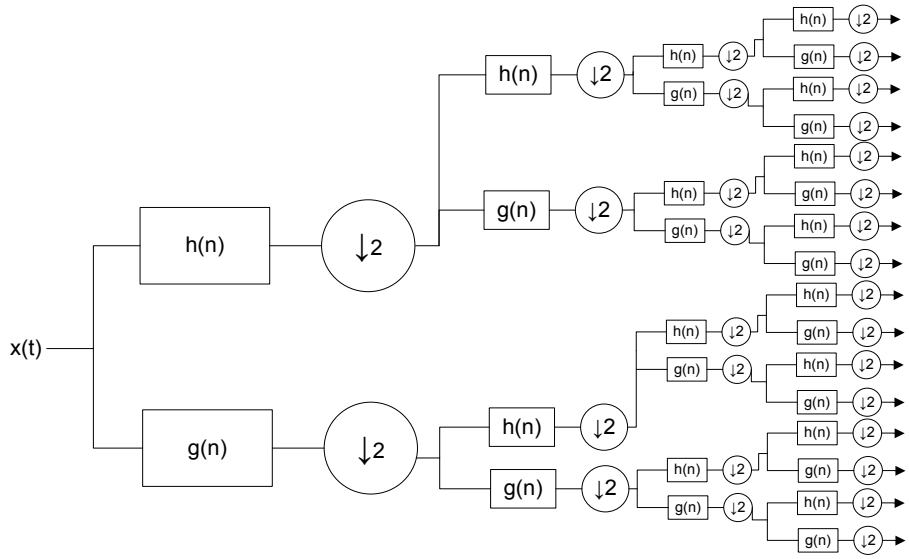

Fig. 4.5: Architecture of basic discrete wavelet packet filters(2 decomposition levels).

The differences between DWT and WP can be seen in the detail coefficients where the next or second decomposition of DWT is applied on the average quadrants from the previous level (Fig. 4.4). The next decomposition of WP is applied on all previous decomposition quadrants (Fig. 4.5).

The number of quadrants in DWT is increased linearly by 3 as the decomposition level is increased by 1 (replace the LL-filter output by its four transforms), as follows:

$$\textit{Quadrants No. at level } K = (\textit{Quadrants No. at level } K\text{-}1) + 3 \qquad (4.3)$$

Details quadrants from previous decomposition levels of WP are transformed; the number of quadrants is increased recursively by 4 as the level is increased by 1 (replace each filter output by its 4 transforms), as follows:

$$\textit{Quadrants No. at level } K = (\textit{Quadrants No. at level } K\text{-}1) \times 4 \qquad (4.4)$$

An example of applying DWT and WP on a phantom slice at different levels of decomposition is illustrated in Fig. 4.6, the average quadrants in both DWT and WP are the same, but the details quadrants are transformed in WP unlike DWT [81].

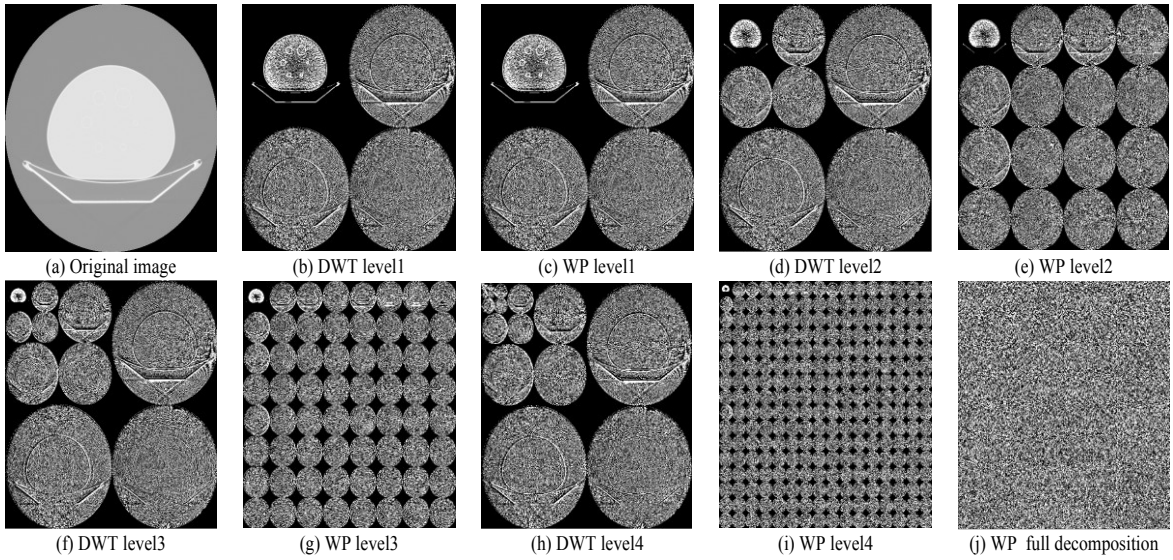

Fig. 4.6: DWT and WP for a phantom slice at different decomposition levels.

It can be seen from Fig. 4.6 (i) and Fig. 4.6 (j) that the transformed image quality is very bad and the quadrant sizes are very small. This adds limitations to the process of applying WP on medical images.

4.3.3. Wavelet Filters

Wavelet filter-banks are derived to suit the needs of specific applications [84][85][86]. In image processing, wavelet filters have been created to improve overall efficiency according to specific mathematical characteristics [87].

In subsequent sections, wavelet uses a set of filters to decompose images depending on filter coefficients and the number of those coefficients. The most popular wavelet filter is Haar Wavelet Filter (HWF) which takes the averages and differences from the low and high pass filters respectively. The Haar basis is used to test algorithm complexity due to its simplistic nature [81]. This function allows for the easy calculation of arithmetic operations within the decompositions.

Daubechies 9/7 filter is also a popular wavelet filter which can be used to test segmentation quality [84][88]. This filter is biorthogonal, has symmetric filter coefficients with a compact support and is highly regulated with four vanishing moments [89].

4.4. Ridgelet Transform

In 1998, Donoho introduced the ridgelet transform [62], CRT can be defined from a 1D wavelet function oriented at constant lines and radial directions. Ridgelet transforms [90][91][92] have been generating a lot of interest due to their superior performance over wavelets in compact approximations of images containing high dimensional singularities. Wavelets do not isolate the smoothness along edges that occurs in images [93], they are thus more appropriate for the reconstruction of sharp point- singularities than lines or edges. These shortcomings of wavelet are well addressed by the ridgelet transform; the functionality of wavelet has been extended to higher dimensional singularities, and becomes an effective tool to perform sparse directional analysis [62][69][94][95]. Generally speaking, wavelets detect objects with point singularities, while ridgelets are able to represent objects with line singularities.

4.4.1. Building Blocks

The ridgelet transform is computed in two steps: a calculation of discrete radon transform and then an application of wavelet transform [94]. The radon transform is also computed in two steps: a calculation of 2D Fast Fourier Transform (FFT) for the image and then an application of a 1D inverse Fast Fourier Transform (iFFT) on all radial directions of the radon projections. Then, 1D wavelet transform is applied restrict to radial directions going through the origin for three levels of decompositions [94].

Applying FRAT on an image can be presented as a set of projections of the image taken place at different angles to map the image space to projection space. Its computation is important in image processing and computer vision for problems such as pattern recognition and the reconstruction of medical images. For discrete images, a projection is computed by summation of all data points that lie within specified unit-width strips; those lines are defined in a finite geometry [94].

4.4.2. Finite Radon Transform

Depending on [95], Finite Radon Transform of a real function *f(l,j)* on the finite grid Z_p^2 is defined in equation (4.5):

$$r_k[l] = FRAT_f\,(k,l) = \frac{1}{\sqrt{P}} \sum_{(i,j)\in L(k,l)} f(i,j) \qquad (4.5)$$

Here, *L(k,l)* denotes the set of points that make up a line on the lattice Z_p^2 :

$$L(k,l) = \{(i,j) : j = k_i + l(mod p), \quad i \in Z_p\}, 0 \leq k < p \qquad (4.6)$$

$$L(p,l) = \{(l,j) : j \in Z_p\} \qquad (4.7)$$

To compute the K^{th} radon projection (i.e. the K^{th} row in the array); all pixels of the original image need to be passed once, and use *P* histogrammers one for every pixel in the row [56]. At the end, all *P* histogrammed values are divided by *K* to get the average values.

4.4.3. Finite Ridgelet Transform

Once the wavelet and radon transforms have been implemented, the Ridgelet transform is straightforward [69]. Each output of the radon projection is simply passed through wavelet transform before it reaches the output multiplier. As shown in Fig. 4.7, ridgelets use FRAT as a basic building block where FRAT maps a line singularity into point singularity, and the wavelet transform has used to effectively detect and segment the point singularity in radon domain. Fig. 4.8 illustrates a clinical chest slice from a CT scanner [96] in the last step before image reconstruction at different block sizes.

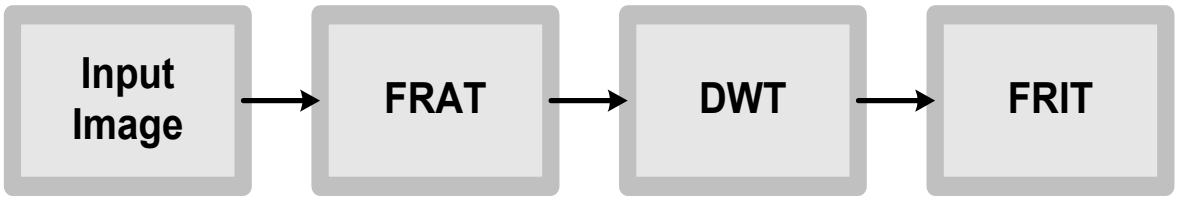

Fig. 4.7: FRIT block diagram

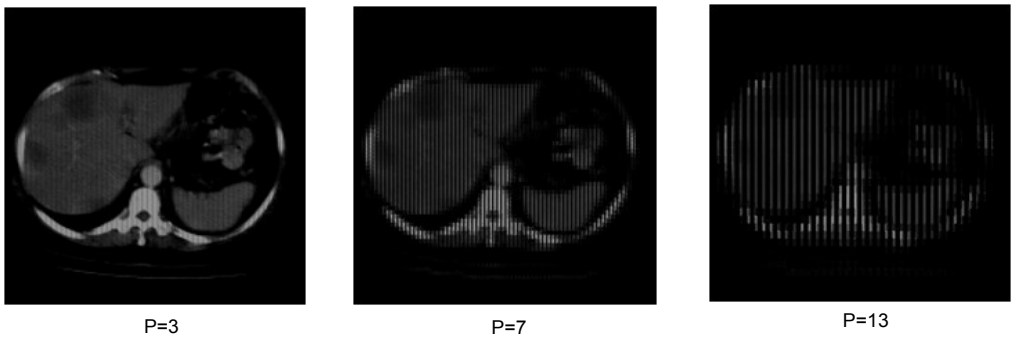

Fig. 4.8: Ridgelet transform for real CT images at block sizes (3, 7, and 13)

It can be seen from Fig. 4.8 that data loss percentage is increased as the prime number *P* getting bigger. This is due to averaging bigger groups of pixels together and unifying their values while *P* value is increasing. Fig. 4.9 illustrates the block diagram of applying ridgelet transform on a clinical example.

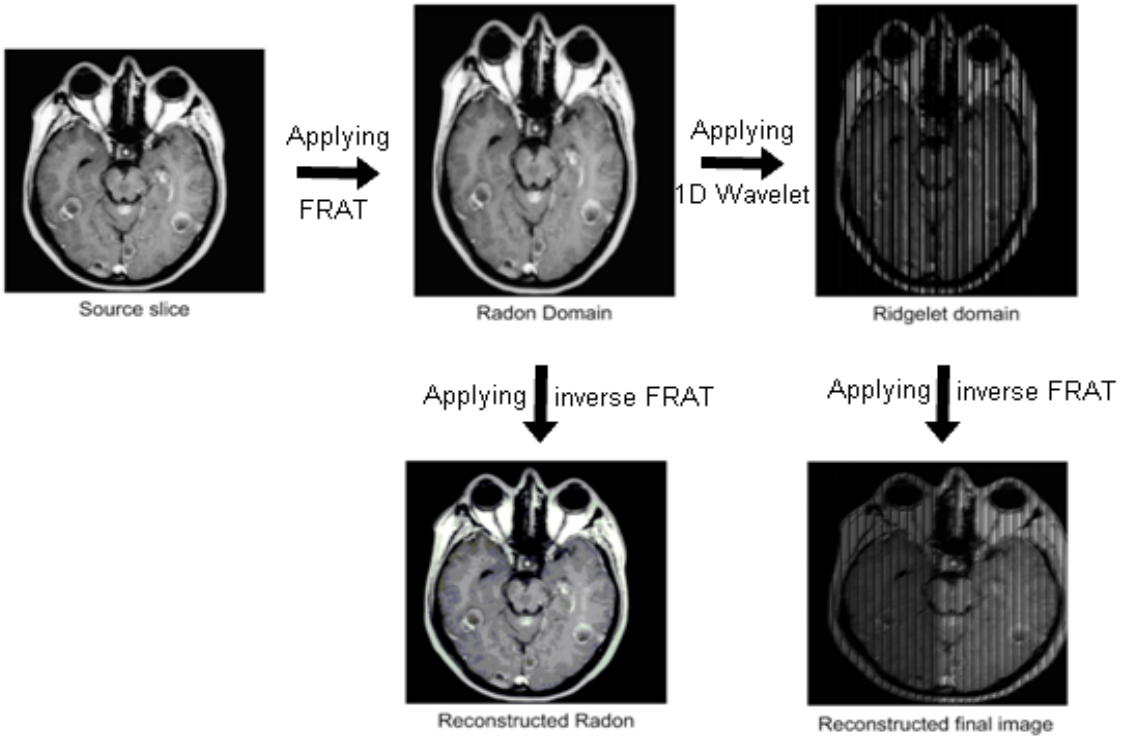

Fig. 4.9: Clinical example of ridgelet transform stages

Pixels visualization in ridgelet domain is close to their visualization in wavelet domain except that in wavelet domain pixels are visualized by point parameters *(x,y)* in the Cartesian grid (first part of Fig. 4.10), any pixels in the image performed as an entry in a 2D matrix. Those are visualized in ridgelet domain by line parameters *(β,θ)* where *β* is the intercept and *θ* is the angle. Second part of Fig. 4.10 illustrates the radial grid in ridgelet transform [69].

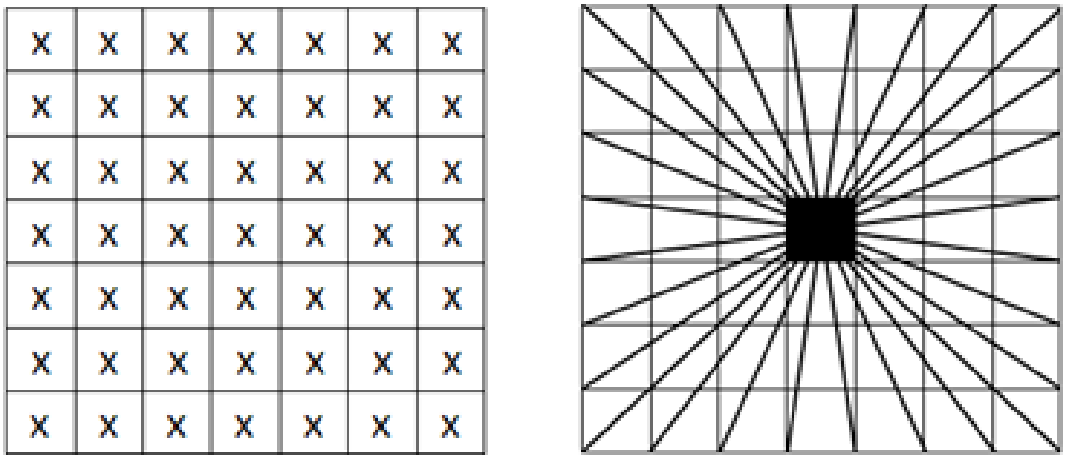

Fig. 4.10: Wavelet and ridgelet visualization parameters

4.4.4. Limitations

Segmentation results achieved by applying ridgelet transformation on medical images were not promising. Any medical image contains a lot of curves which comprise most of ROI and the other body obstacles. Those curves are still not singularity points after applying radon transform. Thus, wavelet transform cannot detect those singularities properly [69][97]. This explains why the ridgelet transformation is not suitable for segmenting most of medical images.

Ridgelet transform can be used in other applications where images contain edges and straight lines. Curvelet transform has been introduced here to solve this problem, it can detect higher singularities compared to wavelet and ridgelet transforms, and could be more suitable and reliable for medical image segmentation using MRA.

4.5. Curvelet Transform

The curvelet transform has gone through two major revisions. It was first introduced by Candés and Donoho in 2000 [90], who used a complex series of steps involving the ridgelet analysis of the radon transform of an image. Their performance was very slow hence researchers developed a new version which is easier to use and understand. In this new method the use of ridgelet transform as a pre-processing step was discarded thus reducing the amount of redundancy and increasing the speed considerably in the transform [90].

Curvelet transform is a new extension of wavelet transform which aims to deal with interesting phenomena occurring along curved edges in 2D images [77]. It is a high-dimensional generalization of the wavelet transform designed to represent images at different scales and orientations (angles). It is viewed as a multiscale pyramid with frame elements indexed by location, scale and orientation parameters with needle-shaped elements at fine scales. Curvelets have time-frequency localization properties of wavelets but also shows a very high degree of directionality and anisotropy, and its singularities can be well approximated with very few coefficients. As illustrated in Fig. 4.11, curvelet requires fewer coefficients for representation and the edge produced from curvelet is smoother than wavelet edge [90][95].

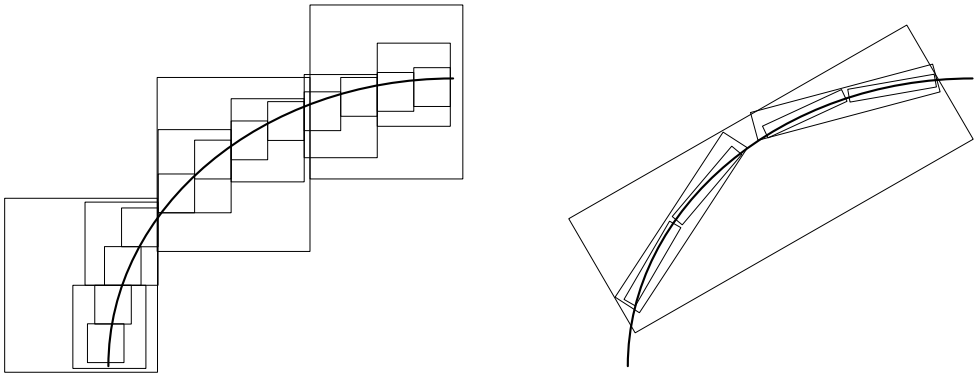

Fig. 4.11: An approximating comparison between wavelet (left) and curvelet (right) [90].

The newly constructed and improved version of curvelet transform is known as Fast Discrete Curvelet Transform (FDCT). This new technique is simpler, faster and less redundant than the original curvelet transform which based on ridgelets. According to *Candes et al.* in [77], two implementations of FDCT are proposed:

- Unequally-spaced Fast Fourier transforms (USFFT)
- Wrapping function.

Both implementations of FDCT differ mainly by the choice of spatial grid that used to translate curvelets at each scale and angle. Both digital transformations return a table of digital curvelet coefficients indexed by a scale parameter, an orientation parameter and a spatial location parameter. Wrapping-based transform is based on wrapping a specially selected Fourier samples, and it is easier to implement, analyze and understand.

The new implementation of curvelet transform based on Wrapping of Fourier samples takes a 2D image as an input in the form of a Cartesian array *f[m, n]*, where $0 \leq m < M$, $0 \leq n < N$, *M* and *N* are the dimensions of the array. As illustrated in equation (4.12), the outputs will be a collection of curvelet coefficients $c^D(j, l, k_1 k_2)$ indexed by a scale *j*, an orientation *l* and spatial location parameters k_1 and k_2 [95].

$$c^D(j,l,k_1k_2) = \sum_{\substack{0 \le m < M \\ 0 \le n < N}} f[m,n]\, \varphi^D_{j,l,k_1k_2}[m,n] \qquad (4.12)$$

Each φ^D_{j,l,k_1k_2} is a digital curvelet waveform, superscript *D* stands for "digital". These approach implementations are the effective parabolic scaling law on the subbands in the frequency domain to capture curved edges within an image in more effective way. As mentioned earlier, wrapping based curvelet transform is a multiscale pyramid which consists of several subbands at different scales. It is consisting of different orientations and positions in the frequency domain. At a high frequency level, curvelets are so fine and looks like a needle shaped element and they are non-directional coarse elements at low frequency level.

Figure 4.12 illustrates an image represented in spectral domain in the form of rectangular frequency tiling by combining all frequency responses of curvelets at different scales and orientations, where curvelets are needle like elements at higher scale. It becomes finer and smaller in the spatial domain and shows more sensitivity to curved edges as the resolution level is increased. Thus allowing to effectively capturing the curves in an image and curved singularities can be well-approximated with fewer coefficients.

In order to achieve a higher level of efficiency, curvelet transform is usually implemented in the frequency domain. This means that a 2D FFT is applied to the image. For each scale and orientation, a product of U_{jl} "wedge" is obtained, the result is then wrapped around the origin, and 2D IFFT is then applied resulting in discrete curvelet coefficients. Candes *et al* describe the discrete curvelet transform in [77] as illustrated in equation (4.12).

$$Curvelet\ transform = IFFT\ [FFT\ (Curvelet)\ X\ FFT\ (Image)] \qquad (4.13)$$

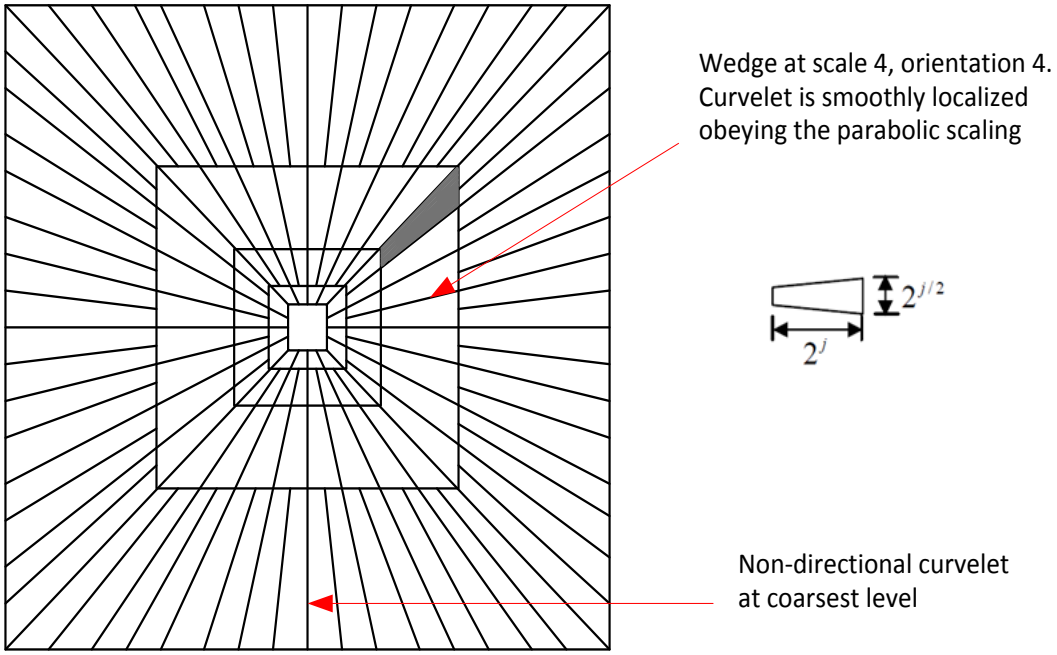

Fig. 4.12: 5-level curvelet digital tiling of an image [95].

The difficulty behind this is that trapezoidal wedge does not fit in a rectangle of size 2^{j} x $2^{j/2}$ aligned with the axes in the frequency plane, where the 2D IFFT could be applied to collect curvelet coefficients. The wedge wrapping procedure proposed in [77] uses a parallelogram with sides 2^{j} and $2^{j/2}$ to support the wedge data, the wrapping is done by periodic tiling of the spectrum inside the wedge and then collecting the rectangular coefficient area into the centre. The centre rectangle of size 2^{j} x $2^{j/2}$ successfully collects all the information in that parallelogram [98].

Fig. 4.13 illustrates the process of wrapping wedge where the angle θ is in the range ($\pi/4$, $3\pi/4$) and the rectangles have the same width and length as the parallelogram is centered at the origin [77].

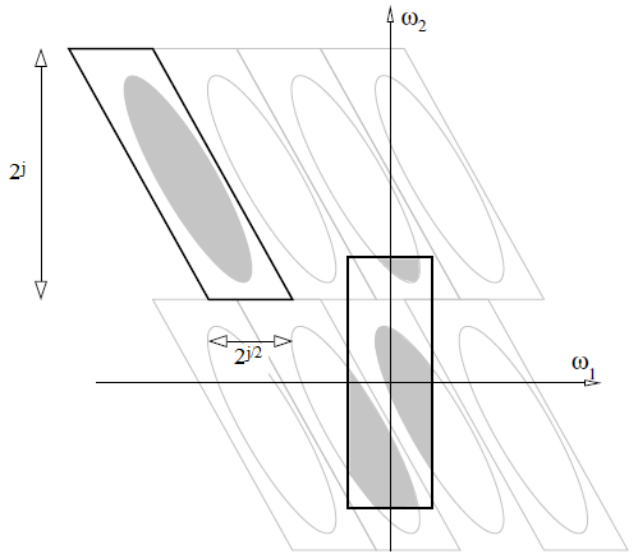

Fig. 4.13: Wrapping wedge data [79].

The following are the steps of applying wrapping based FDCT algorithm [77]:

Step 1: Apply the 2D FFT to an image to obtain Fourier samples:

$$\hat{f}[m,n], -\frac{n}{2} \leq m,n < \frac{n}{2}$$

Step 2: For each scale *j* and angle *l,* form the product:

$$\widetilde{U}_{j,l}[m,n]\hat{f}[m,n]$$

Step 3: Wrap this product around the origin and obtain:

$$\tilde{f}_{j,l}[m,n] = W\left(\widetilde{U}_{j,l}\hat{f}\right)[m,n]$$

Where the range for *m, n* and *θ* is now $0 \leq m < 2^j$, $0 \leq n < 2^{j/2}$, and $-\pi/4 \leq \theta < \pi/4$.

Step 4: Apply IFFT to each $\tilde{f}_{j,l}$, hence collecting the discrete coefficients $c^D(j,l,k_1k_2)$.

The curvelet transform is a multiscale transform such as wavelet, with frame elements indexed by scale and location parameters. Wavelets are only suitable for objects with point singularities, Ridgelets are only suitable for objects with line singularities while curvelets have directional parameters and its pyramid contains elements with a very high degree of directional specificity. The elements obey a special scaling law where the length and the width of frame elements support are linked using equation (4.14):

$$width \approx length^{2} \qquad (4.14)$$

Discrete curvelet transform in the spectral domain utilizes the advantages of FFT, during FFT both image and curvelet at a given scale and orientation are transformed into the Fourier domain. The convolution of the curvelet with the image in the spatial domain then becomes their product in the Fourier domain. At the end of this computation process, a set of curvelet coefficients are obtained by applying IFFT to the spectral product. This set contains curvelet transform coefficients in ascending order of the scales and orientations.

As illustrated in equation (4.13), the data acquisition geometry separates the curvelet expansion of the object into two pieces; this is explained in the following equation:

$$f = \sum_{n \in Good} \langle f, \varphi_n \rangle \, \varphi_n + \sum_{n \notin Good} \langle f, \varphi_n \rangle \, \varphi_n \qquad (4.15)$$

The first part of equation (4.14) can be recovered accurately while the second part cannot. What is interesting here is that one can provably reconstruct the recoverable part, the accuracy will be similar to that one achieved even if one had complete data. There is indeed

a quantitative theory showing that for some statistical models which allow for discontinuities in the object to be recovered, there are simple algorithms based on the shrinkage of curvelet biorthogonal decompositions, which achieve optimal statistical rates of convergence [90]. Fig. 4.15 illustrates the frequency response of curvelets at different scales and orientations for some test images using "***Curvelab (version: 2.1.2)***" in both domains [99].

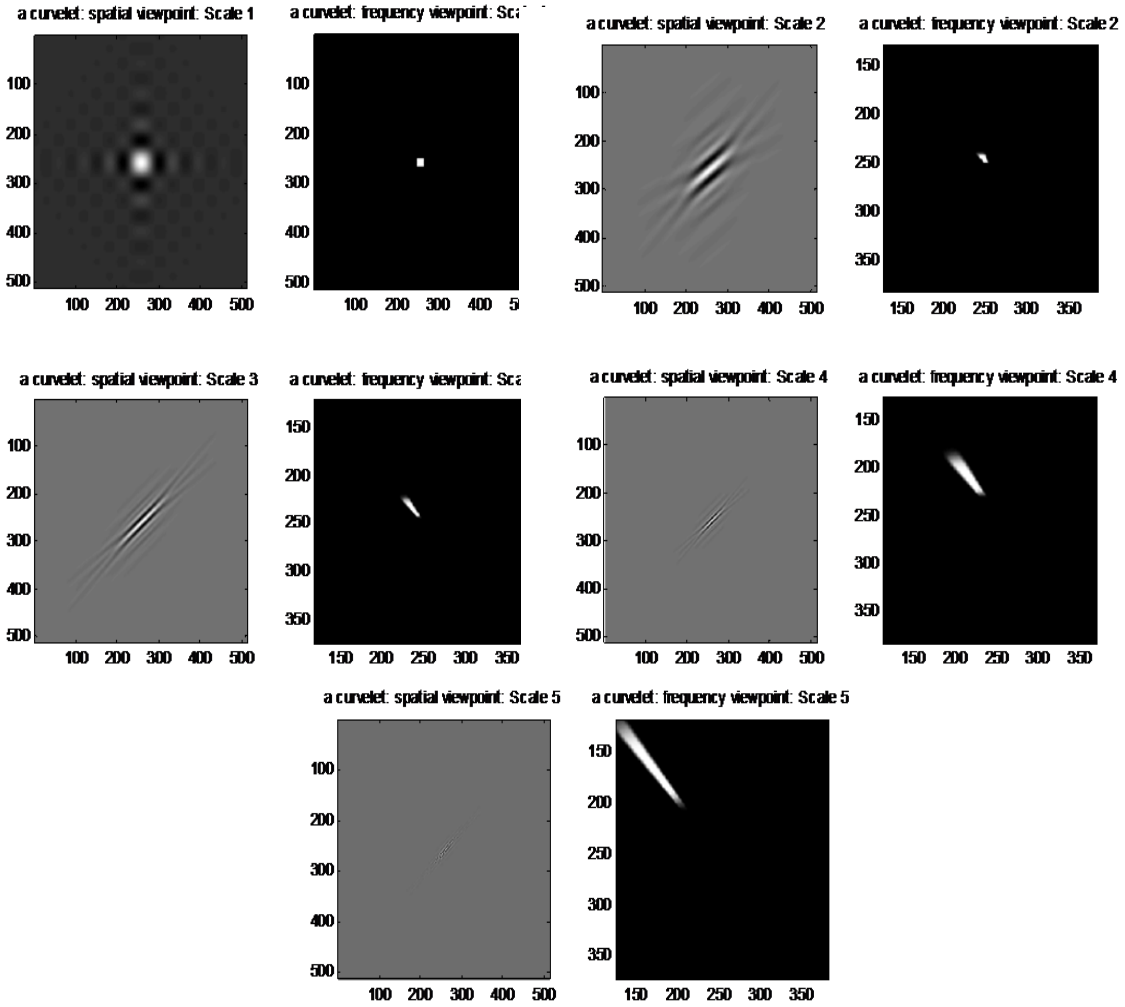

Fig. 4.14: Curvelets at increasingly fine scales from 1 to 5 (Spatial domain and Frequency domain) [99].

From Fig. 4.15, curvelets are non-directional at coarsest level. Fig. 4.15 illustrates a clinical data for human chest from CT scanner in spatial viewpoint and its curvelet coefficients in the frequency view point. In Fig. 4.15, the low frequency coefficients (coarse scale) are stored at the centre of the display. The concentric coronae (formed by black strips) show coefficients at different scales and the outer coronae correspond to higher frequencies. Each corona has four strips further subdivided in angular panels; each panel represents coefficients at a specified scale and orientation suggested by the position of the panel. Wedge wrapping is done for all the wedges at each scale in the frequency domain to obtain a set of subbands or wedges at each curvelet level, these sub-bands are the collection of discrete curvelet coefficients.

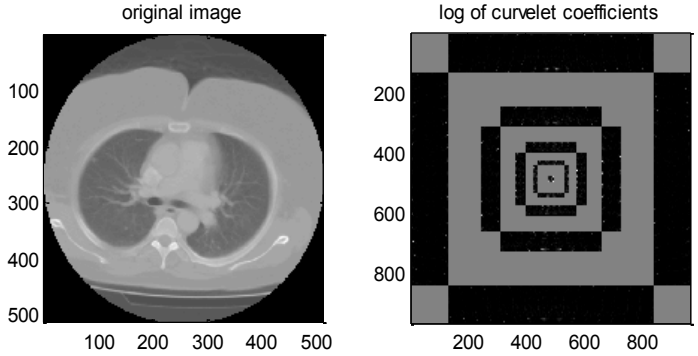

Fig. 4.15: Clinical slice for the human chest from a CT scanner in spatial (left) and curvelet coefficients (right).

4.6. Experiments and Results Analysis

The end users of the proposed system are the radiologists and specialists who analyse medical images for cancer diagnosis. The main radiologists' goal is to locate the cancer in medical images and detect its accurate size with the least errors. This process may be

affected by the noise surrounding ROI, which make the process of measuring the exact dimensions so hard. A proposed data set has been carried out with the MRA segmentation system to validate it for clinical applications. The data name is NEMA IEC body phantom which consists of an elliptical water filled cavity with six spherical inserts suspended by plastic rods of inner diameters: 10, 13, 17, 22, 28 and 37 mm [100] (Fig. 4.16).

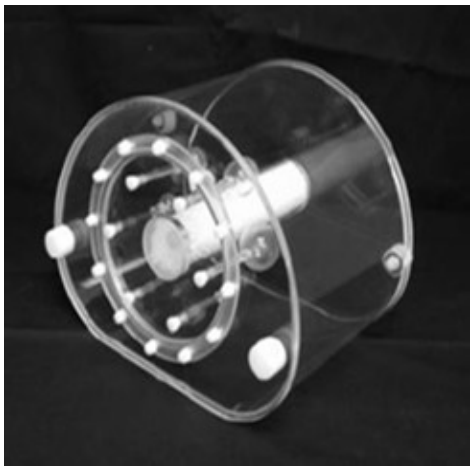

Fig. 4.16: NEMA IEC body phantom

4.6.1. Performance measurement metrics

Many techniques can be used for segmentation, and each technique has a different segmentation performance and quality compared to the others. As mentioned in chapter 3 - section 3.4; many performance evaluation techniques are available, but not all of them are suitable to judge on MRA performance for segmenting a predefined proposed phantom data. Euclidean distance is the best performance metric for evaluating the quality of segmenting NEMA IEC body phantom using MRA. Other performance metrics can be used instead of Euclidean distance to evaluate different factors.

4.6.2. Experimental results

Table 4.1 illustrates the SNR values of extracted features from NEMA IEC DATA SET in spatial domain, different levels of decomposition of wavelet domain and at different block sizes in ridgelet domain.

Table 4.1: Wavelet and ridgelet comparisons depending on SNR and processing time.

Domain	Wavelet			Ridgelet			Spatial
	Level 1	Level 2	Level 3	P = 5	P = 11	P = 31	
SNR (dB)	10.63	11.14	10.95	10.37	11.43	11.88	7.17
Time (sec)	0.23	0.24	0.50	71.5	29.91	10.01	1.18

It can be seen from Table 4.1 that small values of SNR have been obtained for all techniques; this is due to the noise from the acquisition systems itself. This noise will be a part of the medical image after the reconstruction of all slices. Relatively better SNR values can be achieved with the second level of wavelet decomposition and as the block size (p) is getting bigger with the ridgelet transform, where the transformed image is getting more similar to the original image. This can be assigned to the major limitation of using ridgelet transformation in medical image segmentation where ridges rarely exist in such data.

MRA transforms have been used with thresholding technique to segment the experimental data. Thresholding technique has been applied as a pre-processing step on the original images at threshold value (t=35) to remove as much artificial spam sequel produced from the scanners. The transform then applied to effectively represent objects with edges which

are the contours of the medical images followed by another thresholding at (t=7) to remove most of the remaining noise and facilitate the measurement process.

Fig. 4.17 illustrates the segmentation using curvelet transform. Fig. 4.17 (a) and Fig. 4.17 (c) illustrate the original images from a CT scanner, Fig. 4.17 (b) and Fig. 4.17 (d) illustrate the segmented phantom image and real chest image respectively using curvelet transform. As illustrated in Fig. 4.18, results of the proposed segmentation technique vary in terms of smooth reconstruction of the spheres. The curvelet transform segments the input image and removes artifacts from the image to exhibit smooth and optimal segmentation of NEMA phantom. Ridgelet transform detect ROI but does not give promising segmentation results due to the lack of ridges or straight lines in the tested data set. Wavelet quadrants are varying also in their quality; relatively, the best results have been achieved with the LL-filter output.

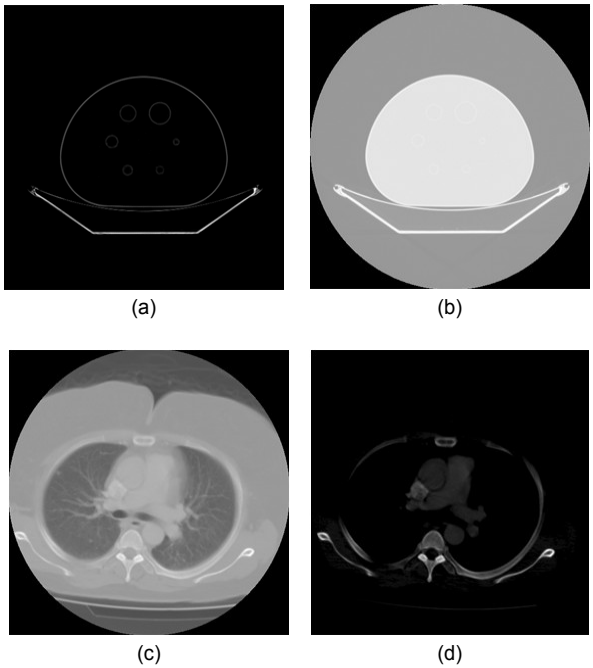

Fig. 4.17: Curvelet transform for segmentation. (a) NEMA IEC body phantom, (b) segmented phantom slice, (c) original real chest slice, (d) segmented real chest slice.

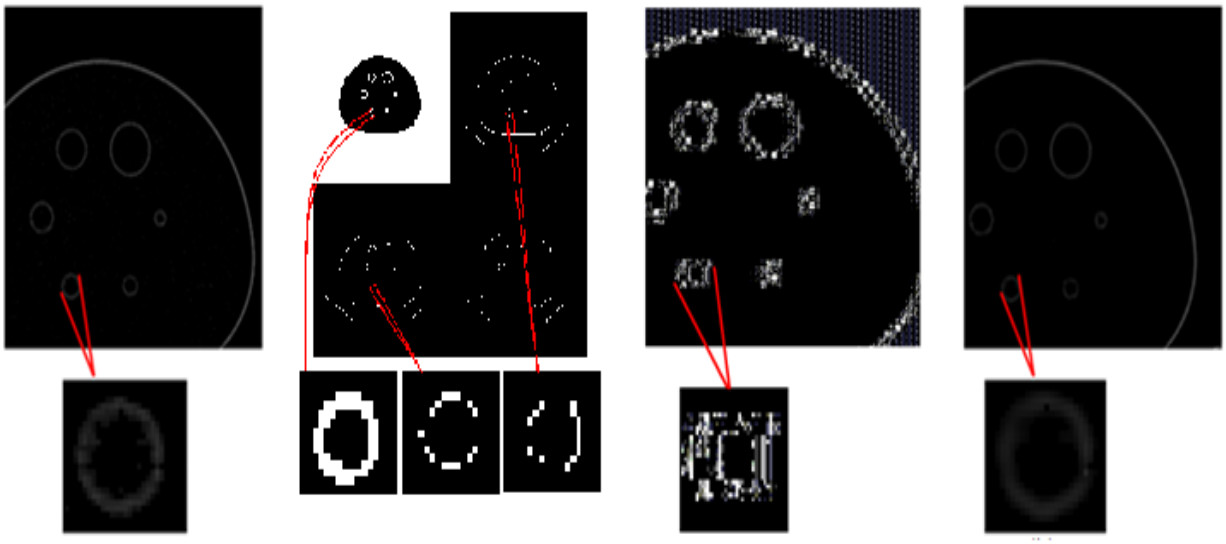

Fig. 4.18: Segmentation using conventional hard thresholding and curvelet-based segmentation. (a) Denoised spatial domain. (b) First level in wavelet domain. (c) Ridgelet domain. (d) Curvelet domain.

Table 4.2 illustrates NEMA spheres diameters error percentages measured using different multiresolution analysis techniques, and compared to previously implemented techniques. ED has been used to measure the spheres diameters and calculate the error percentages for each technique, sphere diameter error percentages have been calculated as follows:

$$error\ \% = \frac{Measured\ Diameter - Actual\ Diameter}{Actual\ Diameter} \times 100\ \% \qquad (4.16)$$

Table 4.2: The error percentages of spheres diameters measurements for NEMA IEC body phantom

Spheres (mm)			Error % for measured diameters					
			10	**13**	**17**	**22**	**28**	**37**
K-means [1]			-4.7	-4.0	-1.94	-1.86	-1.71	-1.7
MRFM [1]			-2.5	-3.0	1.4	1.31	1.28	1.27
Manual Clustering			5.9	5.08	2.94	2.45	1.79	0.35
Iterative Thresholding [101]			3.0	3.1	0.6	0.9	1.1	1.8
Wavelet	**Haar**	**Level 1**	-2.9	-2.46	1.35	0.82	0.29	0.05
		Level 2	-10.9	-6.67	3.88	-1.3	-0.76	-1.95
		Level 3	---	---	5.65	-18.2	2.57	-3.24
	Daubechies	**Level 1**	-7.43	-2.69	0.12	2.0	2.17	1.81
		Level 2	-5.2	0.15	-4.24	0.73	0.62	-0.11
Ridgelet			-10.93	-6.67	3.88	-1.30	-0.76	-1.95
Curvelet			2.65	1.62	1.07	-0.82	-0.33	-0.09

From Table 4.2, in the case of K-means clustering, tumour volumes are underestimated by approximately 5-6% in most cases, however, for the two smaller spherical inserts, with diameter of 10 mm and 13 mm, respectively, these underestimations are significantly greater. For the smallest sphere, more than a 13% volume discrepancy is recorded, with the K-means algorithm finding it difficult to quantify the tumour accurately. Sphere 2 volume similarly is massively underestimated (11.5%). Unlike K-means clustering, MRFM tends to overestimate the volumes of the spherical inserts, with the exception of Spheres 1 and 2.

Spheres diameters are reduced to the half with each decomposition level of wavelet transform. Three decomposition levels of DWT have been applied on NEMA phantom [100] using two different filters (Haar, Daubechies), and the measured diameters were doubled at each level to produce a fair comparison with the other available techniques. It can be seen that most of the error percentages were decreasing while the spheres diameter increasing, it is worth mentioning that there is no upper bound of the spheres diameters to keep the errors decreasing because the ROI becomes clearer and easier to be detected and measured properly. But tumours in real life are usually very small in the early stage cancer, and the problem is to detect those turnouts' tumours as soon as possible.

The two smallest spherical inserts are still underestimated in most of the techniques and got the largest error percentages. The large volumetric errors encountered using this acquisition exist as a consequence of the poor slice thickness setting selected for the scan. The 4.25 mm slice thickness causes large fluctuations in transaxial tumour areas to occur between image slices. This problematic characteristic occurs most notably with the smallest spherical inserts, where single voxel reallocation causes a large deviation in percentage error. In Fig. 4.19, the percentage error computed between the actual sphere volume and the volumes obtained using all methodologies for each of the six tumours inserts is plotted. It can be seen that all techniques are settled down according to the error percentages as the sphere diameters increased.

It can be also seen from Table 4.2 that acceptable error percentages have been achieved using ridgelet transform for the big spheres (22 mm, 28 mm, 37 mm), where the curves are not sharp and ridgelet detect it accurately as it close to be ridges. But for the small spheres, ridgelet weakness for medical image segmentation start appears clearly.

Curvelet transform overcomes the weakness of wavelet for segmenting sharp curves and detect the small spheres accurately with error percentages (0.82% - 2.65%). For the big spheres, errors achieved using wavelet transform are still better than those achieved using curvelet transform due to the sharpness of that spheres. But still very good results using curvelet transform and acceptable for clinical applications.

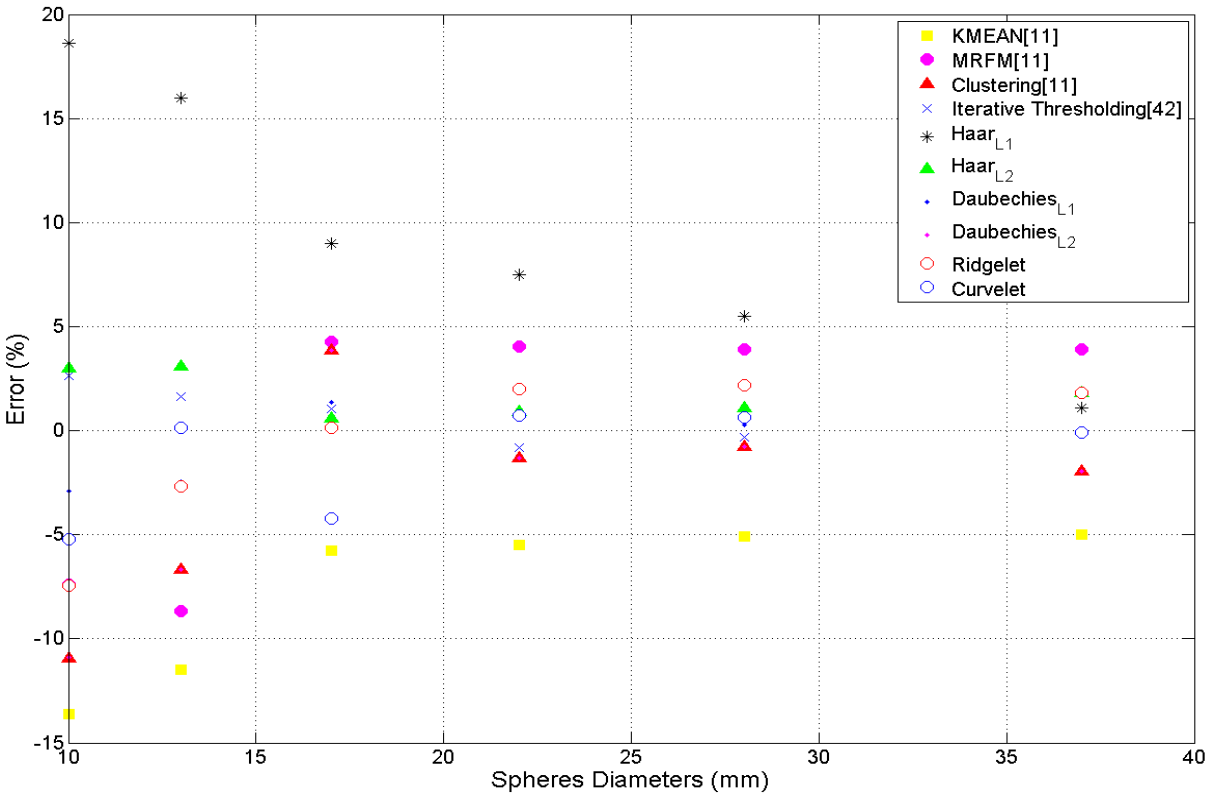

Fig. 4.19: Visual comparison for error percentages in Table 4.2.

PSNR and MSE have been also used to evaluate the quality of the proposed techniques. The original image has been contaminated with Gaussian white noise at σ=20% of the maximum intensity. Table 4.3 illustrates a comparison study of curvelet transform with the

other traditional transforms, comparison terms PSNR and MSE have been used to test the quality of the transformed image.

Table 4.3: Comparison of Curvelet, Ridgelet, and Wavelet denoising in terms of PSNR and MSE.

Image name	Curvelet Denoising		Ridgelet Denoising		Wavelet Denoising	
	MSE	PSNR (dB)	MSE	PSNR (dB)	MSE	PSNR (dB)
NEMA	41.67	31.93	108.78	26.14	101.12	28.08
Chest	58.8	30.44	152.45	23.55	147.63	26.44

From Table 4.3, it can be seen that the best results according to both PSNR and MSE have been achieved using curvelet transform. Wavelet transform performs better results compared to ridgelet transform in both validation metrics. Fig. 4.20 illustrates two noisy images and the denoised outputs using both wavelet and curvelet.

According to a study done by *Dettori* and *Semler* [95], the ridgelet-based descriptors had significantly higher performance measures in comparison to wavelet-based descriptors, with accuracy rates higher than any other wavelet based feature set for all individual organs. This is not surprising given the fact that the ridgelet transform is able to capture multi-directional features, as opposed to the wavelet transform which focus mainly on horizontal, vertical, and diagonal features. This can be generalized to most of the images except for medical scanners where the weakness of wavelet is not dominant in such images.

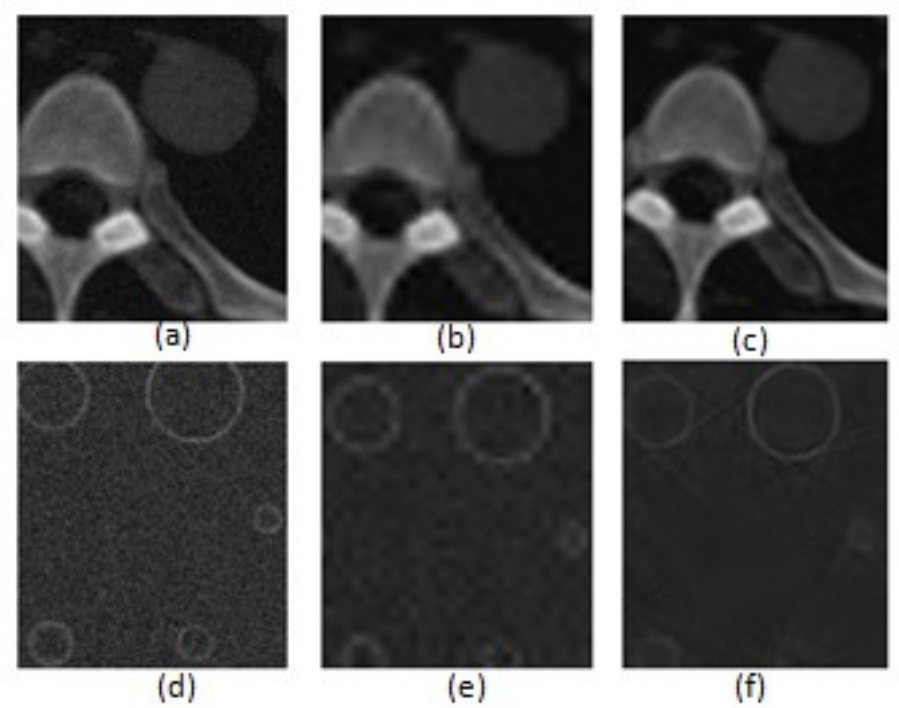

Fig. 4.20: MRA for image denoising. (a,d) Noisy images. (b,e) wavelet. (c,f) Curvelet.

Curvelet-based descriptors had an even higher performance in comparison to both the wavelet and ridgelet, with accuracy rates higher, respectively. The accuracy rate using curvelet transform is better, this is expected since the curvelet transform is able to capture multi-directional features in wedges, as opposed to lines or points as in the ridgelet or wavelet transform. The multidirectional features in curvelets are very effective in extracting the important features from medical images, and then segmented accurately.

As illustrated in the previous tables and figures, it can be seen that more efficient and smooth image reconstruction is achieved using curvelet transform. In terms of optimal reconstruction of the objects with edges and curves, curvelet-based techniques outperform the traditional wavelet and ridgelet transforms.

The algorithm presented in this chapter is able to classify normal tissues in CT scans with high accuracy rates. These hypotheses will be further tested and validated on different predefined clinical data sets in chapter 8 of this thesis.

4.7. Summary

Due to the changing shapes of organs in medical images, segmentation process using multiresolution analysis combined with thresholding and/or other techniques as pre- and post-processing step allows accurate detection of ROIs. Multiresolution analysis such as wavelet transform is extensively used in medical image segmentation and provides better accuracy in results. Curvelet and ridgelet transforms are new extension of the wavelet transform that aims to deal with interesting phenomena occurring along higher dimensional singularities. Though wavelets are well suited to point singularities, they have limitations with orientation selectivity hence do not represent changing geometric features along edges effectively. Curvelet transform exhibits good reconstruction of the edge data by incorporating a directional component to the traditional wavelet transform. Experimental study for using MRA in medical image segmentation has shown that curvelet based segmentation of the medical images not only provide good quality reconstruction of detected ROI, promising results are also achieved in terms of accurately detecting ROI and denoising process. Curvelet transform is a new tool and utilization of this technique; it is far from sufficient in the medical image processing area.

Chapter 5

Statistical Modeling for Medical Image Segmentation – Hidden Markov Models

5.1. Introduction

Markov model is a mathematical model of stochastic process that generates random sequences of outcomes according to certain probabilities [102]. A stochastic process is a sequence of orientation codeword's. HMMs have three types of topologies: Fully Connected, where all states can be reached from any other state such as Ergodic model. The second topology type is Left-Right (LR) model such that each state can go back to itself or to the following states. The last topology is Left-Right Banded (LRB) model in which each state can go back to itself or the next state only [69][102].

For block-based segmentation using statistical classification, an image is divided into blocks, and a feature vector is formed for each block by grouping statistics of its pixel

intensities [103][104]. Conventional block-based segmentation algorithms classify each block separately, assuming the independence of feature vectors.

Segmentation in MRFM is achieved by maximizing the posteriori probability of the segmentation depending on a given image data [105]. MRFM is an earlier version of the HMM, where states in MRFM are directly visible to the observer, and then the state transition probabilities are the only parameters [106]. HMM [107] are used to characterize the statistical properties of a signal. They have been used successfully in speech recognition and face recognition for a number of decades and are now being applied to medical image segmentation.

The segmentation using statistical modeling here is novel, as the use of the grayscale values for generating the observation sequence is new, it performs well in segmenting medical images and overcomes other implemented segmentation techniques.

In this chapter, statistical modeling using HMMs will be used to segment 2D medical images acquired form medical scanners. This segmentation technique is more automated compared to the techniques introduced in chapter 4 and proves promising results in medical image segmentation. The next section summarizes the background of using HMMs in general. The segmentation process of medical images using the proposed HMMs and its three stages has been illustrated in section 5.3, the steps that have been followed to implement HMMs have been also presented in this section. In section 5.4, experimental results of segmentation using HMMs have been illustrated. Finally, the work in this chapter has been summarized in section 5.5.

5.2. HMMs Mathematical Background

A hidden Markov model is one in which you observe a sequence of emissions, but do not know the sequence of states the model went through to generate the emissions. Analysis of hidden Markov models seeks to recover the sequence of states from the observed data. General and brief information on how to use HMMs in its all steps founded in the **Matlab® Statistics Toolbox™ 7** User's Guide with the following example:

Consider a Markov model with 2 states and six possible emissions. The model uses:

- *A red die, having six sides, labeled 1 through 6.*
- *A green die, having twelve sides, five of which are labeled 2 through 6, while the remaining seven sides are labeled 1.*
- *A weighted red coin, for which the probability of heads is 0.9 and the probability of tails is 0.1.*
- *A weighted green coin, for which the probability of heads is 0.95 and the probability of tails is 0.05.*

The model creates a sequence of numbers from the set {1, 2, 3, 4, 5, 6} with the following rules:

- *Begin by rolling the red die and writing down the number that comes up, which is the emission.*
- *Toss the red coin and do one of the following:*
- *If the result is heads, roll the red die and write down the result.*
- *If the result is tails, roll the green die and write down the result.*

At each subsequent step, you flip the coin that has the same colour as the die you rolled in the previous step. If the coin comes up heads, roll the same die as in the previous step. If the coin comes up tails, switch to the other die.

Markov chain is an edge labeled directed graph where each node represents a state, and the edge-label have probabilities of moving the state to the end of the directed edge [108][109]. When modeling a sequence of observation symbols, it is usual to use an LR HMM chain [107] (Fig. 5.1), which has only partial state transition matrix, such that $a_{i,j}=0$, $j<i,i> j+step$, where *step* is a constant usually equal to 1 or 2.

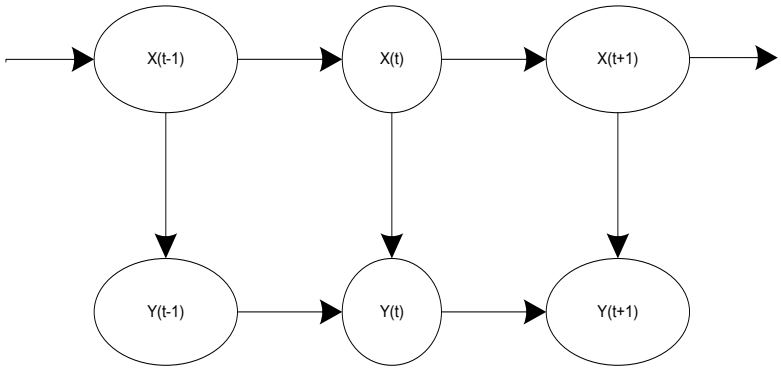

Fig. 5.1: LR Markov chain.

The diagram for the previous model has two states, red and green, as shown in the Fig 5.2. You determine the emission from a state by rolling the die with the same colour as the state. Transition to the next state determined by flipping the coin with the same colour as the state.

- The transition matrix is:

$$T = \begin{bmatrix} 0.9 & 0.1 \\ 0.05 & 0.95 \end{bmatrix}$$

- The emissions matrix is:

$$E = \begin{bmatrix} \frac{1}{6} & \frac{1}{6} & \frac{1}{6} & \frac{1}{6} & \frac{1}{6} & \frac{1}{6} \\ \frac{7}{12} & \frac{1}{12} & \frac{1}{12} & \frac{1}{12} & \frac{1}{12} & \frac{1}{12} \end{bmatrix}$$

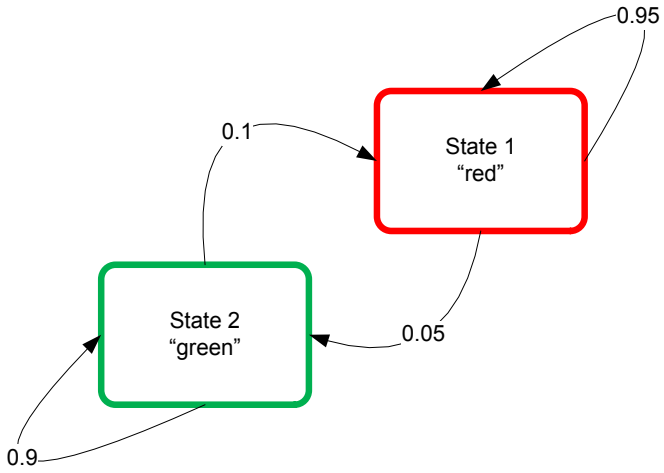

Fig. 5.2: HMM state diagram for the proposed model

The model is not hidden because you know the sequence of states from the colours of the coins and dice. Suppose, however, that someone else is generating the emissions without showing you the dice or the coins. All you see is the sequence of emissions. If you start seeing more 1s than other numbers, you might suspect that the model is in the green state, but you cannot be sure because you cannot see the colour of the die being rolled. Hidden Markov models raise the following questions:

- *Given a sequence of emissions, what is the most likely state path?*
- *Given a sequence of emissions, how can you estimate transition and emission probabilities of the model?*

- *What is the forward probability that the model generates a given sequence?*
- *What is the posterior probability that the model is in a particular state at any point in the sequence?*

These questions will be answered in section 5.3 where HMMs are used for segmenting 2D images.

HMMs represent a widespread approach to the modeling of sequences as they attempt to capture the underlying structure of a set of symbol strings. The use of HMM for shape recognition has not been widely addressed. Only few works have been found to have some similarities with this thesis proposed approach. At first, *He and Kundu* [110] utilized HMMs to model shape contours through Autoregressive (AR) coefficients. The use of circular HMM for recognition improving scaling and deformation robustness is proposed in [111][112].

HMM is basically a stochastic finite state automation, formally defined by the following elements [107]: a set of ***states*** $S=S_1,...,S_i,...,S_j,...,S_N$; a ***state transition probability distribution matrix*** $A = \{a_{i,j}\}\ 1 \le i, j \le N$ representing the probability to go from state S_i to S_j ; a set of ***observation symbols*** $V=\{v_1,v_2,...,v_k,...,v_M\}$, where v_k used to be a *d*-dimensional vector (in the case of discrete HMM); an ***observation symbol probability distribution*** or ***emission matrix*** $B=\{b_j(v_k),\ 1 \le k \le M\}\ 1 \le j \le N$, indicating the probability of emission of symbol v_k when system state is S_j ; an ***initial state*** probability distribution $\pi = \{\pi i\}\ 1 \le i \le N$, representing probabilities of initial states. For convenience, HMM has been denoted as a triplet $\lambda = \{A, B, \pi\}$, which uniquely determines the model [69].

As HMMs are one-dimensional in nature, a variety of approaches have been adopted to represent the two-dimensional structure of images:

- **One Dimensional Discrete Hidden Markov Model**

  One Dimensional Discrete HMM (1D-DHMM) is an approach for adapting HMMs to deal with 2D datasets [113][114]. This involves modeling an image using two standard HMMs, one for observations in the vertical direction and one for observations in the horizontal direction. During the segmentation phase, observations in both the vertical and horizontal directions are extracted and tested against HMMs that have been trained on vertical and horizontal observations, respectively.

- **Pseudo Two Dimensional Hidden Markov Model**

  The Pseudo Two Dimensional HMM (P2D-HMM) is a 1D HMM comprising super states to model the sequence of columns in the image [113]. Each super state is itself a 1D HMM, which models the blocks within the columns. In this approach, image columns evaluate a block of pixels which comprise superstates including Markov simplestates. This will briefly explained in section 5.3.

- **Low-Complexity Two Dimensional Hidden Markov Model**

  Low-Complexity Two Dimensional HMM (LC 2D-HMM) consists of a rectangular constellation of states, where both vertical and horizontal transitions are supported [113][115]. The complexity of the LC 2D-HMM is considerably lower than that in P2D-HMM; however, recognition accuracy is lower as a result.

5.3. Image Segmentation using HMM

The problem with 2D-HMM is the double dependency of $S_{i,j}$ on its two neighbours, $S_{i-1,j}$ and $S_{i,j-1}$, as illustrated in Fig. 5.3. This does not allow the factorization of computation as in 1D, where $S_{i,j}$ must only depend on one neighbour at a time. However, this neighbour may be the horizontal ($S_{i,j-1}$) or the vertical ($S_{i-1,j}$) [108][116]. P2D-HMM will be used in this research to implement the 2D HMM structure.

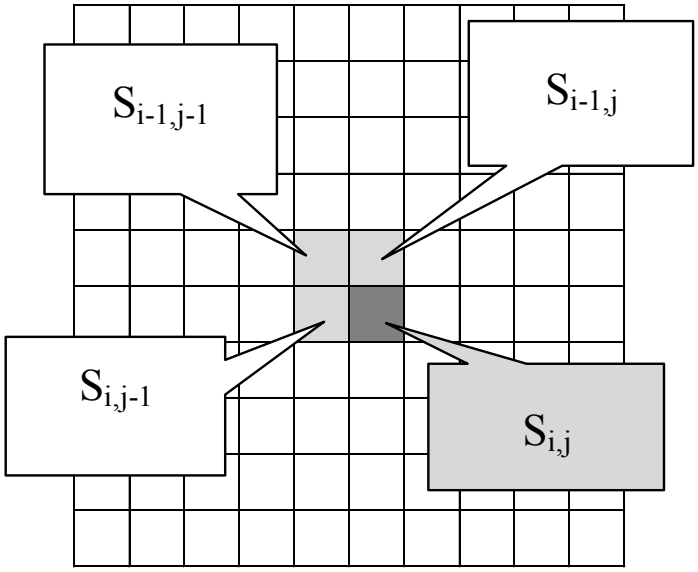

Fig. 5.3: Double dependency problem in 2D HMM segmentation.

Each slice is a 2D matrix which can be classified by an optimum set of states with maximum probability; these states are mapped into classes or segmented objects. The basic assumption of applying P2D-HMM on medical images is to use the embedded-HMM by

defining a set of Markovian superstates, within each superstate there is a set of simple Markovian states. The superstate is first chosen using a first order Markov state transition probability based on the previous superstate. A simple Markov chain is then used to generate observations in this superstate. Thus, superstates are related to rows (or any equal size blocks), and simple states are related to columns (or smaller blocks comprising the superstate) [69][113].

As mentioned in chapter 1, Matlab ® has been used in this research for analyzing the proposed techniques. The following steps are followed to implement HMMs segmentation using:

Step 1: Random state transition and emission probability matrices have been generated based on the number of states; these matrices have to fulfill the condition of HMMs probability matrices where the summation of each row indices values must equal to 1.

Step 2: Create the sequence of observations based on the gray scale values from the medical image.

Step 3: Using the guess matrices (randomly generated) and the observation sequence, a built in Matlab ® function (hmmtrain) is used to create the exact transition and emission matrices. This has been done based on the spatial correlation between the adjacent pixels.

Step 4: The most likely states along the image have been calculated by iterating viterbi algorithm. This has been calculated using a builtin Matlab ® function

(hmmviterbi), the function inputs are the exact matrices and the sequence of observations. And the output is a sequence of the most likely states.

Step 5: Based on the most likely states; each group of pixels that belongs to the same state are group together to form a segmented output image.

As mentioned in section 5.2, using HMMs for segmentation raise some questions to be answered. The following steps of applying HMMs will answer those questions:

5.3.1. Defining the initial states

To generate an observation sequence using HMM, an initial state must be chosen according to the initial state distribution; then an observation sequence should be chosen according to the probability distribution in the initial state [69][108]. Many feature selection techniques have been tested in medical images, and the best results were achieved using the grey-scale values of the medical image pixels to generate the probability distribution matrix. After defining the initial states, transition to a new state will take place according to the state transition matrix for the current state and depending on the sequence of observations.

5.3.2. Training HMM

HMM considers observations statistically dependent on neighbouring observations through transition probabilities organized in a Markov mesh. Training HMM for images is achieved by dividing the image into non-overlapping, equally sized blocks, from each of which a feature vector is extracted. Each block and its feature vector evaluates the observation which has its

own transition probability matrix. Training HMM produces an estimated state transition probability matrix and estimated emission probability matrix.

After building the observation sequence, the model parameters are estimated based on the blocks' statistics. These classes or states were determined using Viterbi algorithm, which depends on (1) *the sequence of observations*; (2) *estimated state transition probability matrix*; (3) *emission probability matrix* [104][117]. Finally, pixels which belong to the same class are grouped together to evaluate a segmented image.

5.3.3. Testing HMM

The feature vectors for a testing image are generated to find a set of classes with maximum posteriori according to the trained HMM. The feature vector for each block may be changed at every single state. Once the block state is known, the feature vector will be independent of the other blocks; any two blocks may be more likely to be in the same state if they have close intensities [118]. In other words, testing HMM will generate the state transition probability matrix and emission probability matrix for a given comparable data [108][118].

5.4. HMM Experimental Results

As mentioned in section 4.6, the end users of the proposed system are the radiologists and specialists who analyze medical images for cancer diagnosis. NEMA IEC body phantom has also been carried out with HMMs segmentations to validate it in clinical applications. HMMs can be applied for medical image segmentation in different ways and with different

transforms; each way has a different segmentation performance and quality. As mentioned in section 3.4; many performance evaluation techniques are available, ED and DSC have been used in this section for measuring the performance of using HMMs for medical image segmentation.

HMMs have been used in this thesis for medical image segmentation, which can be applied either in its spatial or multiresolution domain using wavelet, ridgelet or curvelet transforms. The weakness of HMMs is its long processing time, compared with the other available segmentation techniques. NEMA IEC body phantom has been utilized to perform the experimental study using HMMs and MRA for medical image segmentation, and the achieved results are illustrated in Table 5.1 regarding that equation 4.16 has been used to calculate the error percentages. The results have been measured on an HP Laptop with Intel Core i7 / 1.6 GHz processor and Graphic card NVIDIA® GeForce® GT 230M with 1GB dedicated DDR3 memory, and 4GB RAM.

Table 5.1: Performance diameter measurements error percentages of using HMMs and MRA for medical image segmentation.

diameters (mm)	10	13	17	22	28	37	Processing time (sec)
HMM (Spatial)	1.5	0.8	0.1	0.8	0.04	1.0	2007.3
HMM (Wavelet)	---	11.07	7.82	2.98	1.09	0.27	1321.1
HMM (Ridgelet)	---	---	---	---	---	2.41	5757.6
HMM (Curvelet)	1.03	0.69	0.43	0.27	0.11	0.07	1967.5

From Table 5.1, applying HMMs on NEMA phantom slice in ridgelet domain failed to segment ROI, where most of the spheres diameters could not be detected. As well as the long computational time problem which is five times more than the required time for applying HMMs on the slice in its wavelet domain. Transforming any image into ridgelet domain changes the comprising pixel specifications, as well as the dimensions of the image; this is due to the padding row added to each block. Therefore, very long computational time is required for segmenting an image in its ridgelet domain using HMM segmentation.

The image contains the least noise in the curvelet domain compared to other domains. Therefore, HMMs prove promising results with curvelet transform and segment the proposed phantom properly with more accurate results. Relatively, and according to the segmentation error performance, the accuracy of the proposed HMMs segmentations mentioned in Table 5.1 can be ordered from the best to the worst as: *HMMs with curvelet transform, HMMs in spatial domain, HMMs with wavelet transform, HMMs with ridgelet transform.*

Recalling the computational time for each method, segmentation using HMMs in wavelet domain requires the least processing time as the image size in this transform is reduced to half of its original size with each decomposition level. The images size in both spatial and curvelet domains are the same, but the difference in the computational time is due to the noise occurrence in the image where HMMs will be easier and faster if there is less noise. Therefore, computational time required for HMMs segmentation in curvelet domain is less than the required time in spatial domain. Fig. 5.4 and Fig. 5.5 illustrate the outputs of applying HMM on a slice from NEMA IEC body phantom and a real clinical data for human brain in their spatial domains.

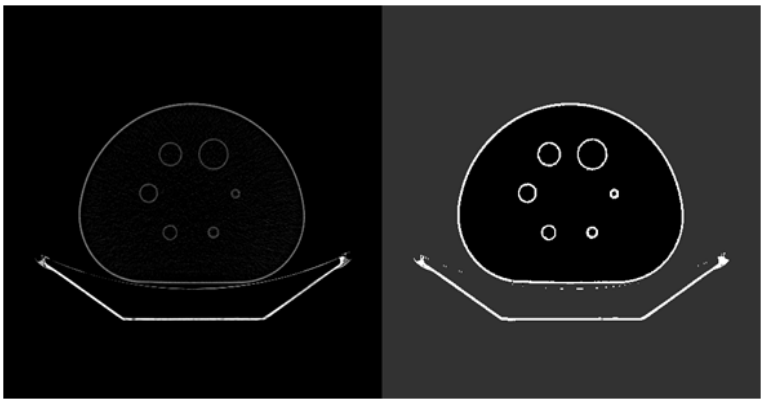

(a) (b)

Fig. 5.4: Segmented NEMA phantom slice using: (a) thresholding technique and (b) HMM.

(a) (b)

Fig. 5.5: HMM for Image Segmentation. (a) Original and (b) HMM.

It can be seen from Fig. 5.5 that different obstacles were merged such as bones and brain tissues; this merger is due to the number of HMM classes (states). HMMs decided that brain tissue and bones in Fig. 5.5 will be in the same class and gave them the same colour because just three HMM classes were used, but each obstacle will be in a separate class if the number of classes increased to be equal to the number of obstacles in the image. There are some available techniques that can be used to define the best number of classes in HMM such as BiC [1][103].

HMMs have been also applied on other clinical data for the human abdomen section illustrated in Fig. 5.6 in both spatial and ridgelet domains. The DSC values for the segmented slices have been measured and illustrated in Table 5.2 which evaluates the performance based on a manual segmented image.

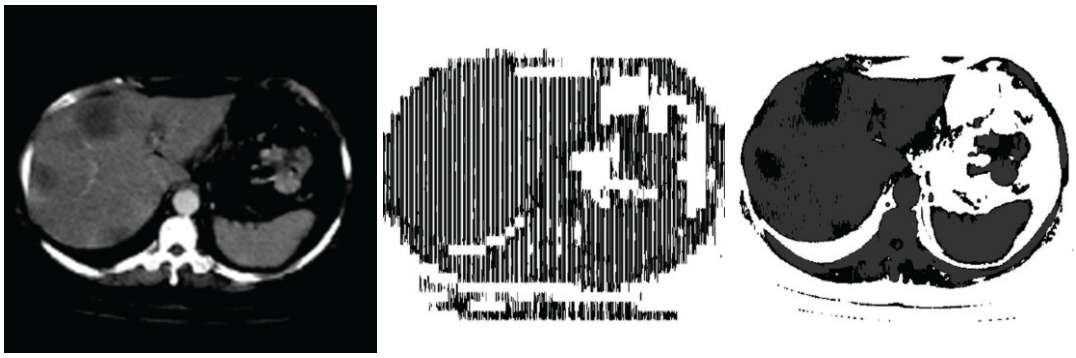

(a) (b) (c)

Fig. 5.6: Image Segmentation using HMM. Original (a), HMM on ridgelet (b), and HMM on spatial (c).

Table 5.2: Performance of using HMMs and MRA for medical image segmentation.

Type	Number of joint pixels	Number of all pixels	DSC value
HMMs in Spatial domain	212521	524288	0.8107
HMMs with Ridgelet transform	158905	524288	0.6062

From Table 5.2, better results have been achieved with HMMs in the spatial domain; this has been expected due to the change in pixels properties by applying ridgelet transform on an image. HMMs have been applied on the chest image after extracting the important features using curvelet transform (Fig. 5.7).

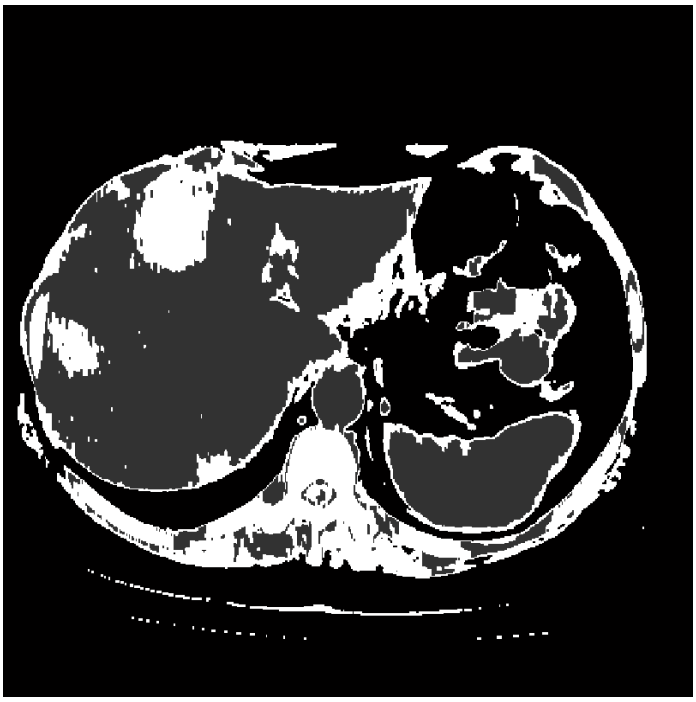

Fig. 5.7: image Segmentation using HMM and curvelet transform

Structural Hidden Markov Model (SHMM) is a modified version of Markov model which has been implemented by *Bouchaffra and Tan* [119]. We have implement and modify this new model to be suitable for segmenting medical images. Despite SHMM proves promising results and overcomes HMMs in many applications such as face recognition, its results for medical image segmentation were worse than the traditional HMMs and requires much more computational time for segmentation. Therefore, we decide not to use it in the proposed medical image segmentation system.

The algorithm presented in this chapter is able to classify normal tissues in medical scans with high accuracy rates. These hypotheses will be further tested and validated on different predefined real clinical data sets in chapter 8 of this thesis.

5.5. Summary

Promising results have been achieved with the statistical models using HMMs; Applying HMMs for medical image segmentation has a limitation which is the long computational time. HMM could be applied with different MRA transformations such as wavelet, ridgelet, and curvelet to improve the proposed system quality. It is worth mentioning that based on the experiments carried out on the specific medical data in section 5.4; HMMs can be classified as one of the ideal medical image segmentation techniques compared to the work done in this thesis using other methods.

Chapter 6

Medical Volume Segmentation using 3D Techniques

6.1. Introduction

3D volume is a 3D matrix whose indices represent samples of a certain physical quantity, 3D volumes may also be called volumetric images [3]. The most common way for generating a 3D data set in medical applications is from tomographic devices such as PET, CT, or MRI [3]. 3D volume segmentation is the process of partitioning voxels into 3D regions (sub-volumes), that represent meaningful physical entities which are more meaningful and easier to analyze, and usable in future applications. In medical applications, a stack of slices is produced from the source of the volumetric images which are the acquisition systems; each is a 2D medical image which performs a specific human body section. 3D volumes can be evaluated either by the volume they occupy or by their contouring edges.

The main goal in this chapter is to develop segmentation methods which can be applied directly to medical volumes acquired from the scanners without slicing them. The

output of applying these methods on 3D medical data will be a segmented volume which clearly visualizes OOI, these segmented output is easier to analyze and understand than the original scanner output data. Section 6.2 gives a general overview of 3D image processing. 3D wavelet transform and 3D HMMs for medical volume segmentation are introduced in sections 6.3 and 6.4 respectively. And a comparison between the proposed 2D and 3D segmentation techniques is illustrated in section 6.5. Section 6.6 includes a summary of the work implemented in this chapter.

6.2. Overview of 3D image processing

Any section in the human body can be performed by a stack of 2D medical images (slices), these slices are acquired from the acquisition scanners. All slices are grouped together using Matlab® code [120] to form a 3D matrix which evaluates the 3D medical volume.

Voxels' classification into objects is performed by requiring that voxels belong to certain range and share some predefined properties. Those voxels comprise a distinct or segmented OOI from the input volume [3]. Medical scanners are capable of slicing an object in a physical sectioning, 3D data set from those devices can be considered as a parallel slices stacked to form a 3D volume.

Nikolaidis mentioned in [3] that Volume Edge Detection (VED) is usually performed by convolving the volume with a set of 3D masks; each mask acts as a discrete approximation of the partial derivative with respect to a specific direction. VED techniques have not been used alone as a volume segmentation technique, because the use of VED

comes from the fact that edges are produced by the edge detection operators, and they do not form closed contours. Thus, other 3D techniques may be combined with VED to obtain better results.

There are several techniques to perform medical volume segmentation, of which thresholding approach is the simplest. If the values which evaluate the voxels that represent a specific object in the 3D data set are in a specific range without overlapping the background or any other object voxels' values range, thresholding technique will be the best way to segment such volumes [121].

Voxels whose intensity falls between two threshold values are assigned to the segmented object or OOI. The success of using thresholding as a segmentation technique is based mainly on choosing the threshold values; it is not easy to set them automatically. In many applications, the threshold values selection can be done depending on the basis of volume histogram. Spatial information is not taken into account in thresholding. Therefore, the voxels of a certain object are not necessarily connected. In other words, the OOI might be a number of completely separated sub-volumes.

6.3. 3D Wavelet Transform

Applying 3D-DWT is not easy; the difference between 2D images and 3D volumes is the third dimension (depth or Z-axis). The expected transform after applying one decomposition level of 3D-DWT is illustrated in Fig 6.1.

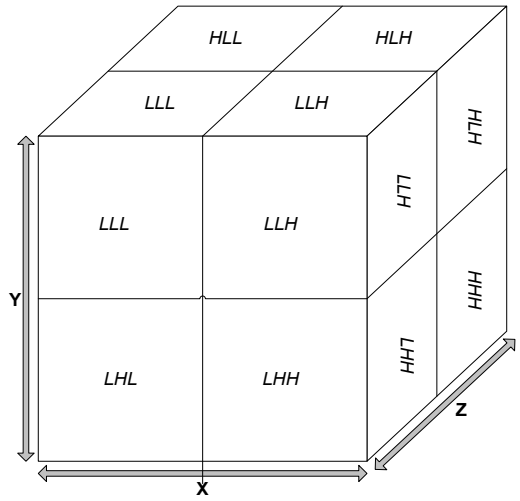

Fig. 6.1: 3D volume in wavelet domain.

Applying one level of 3D-DWT is the process of transforming the original volume into 8 octants in its wavelet domain. Mathematically, 3D-DWT is the process of applying 1D-DWT on each vector in Z-axis which has the same X-axis and Y-axis coordinates after applying 2D-DWT for all comprising frames. Algorithm 6.1 illustrates the 3D-DWT pseudo code, and the filter structure of 3D Haar wavelet transform is shown in Fig 6.2.

Algorithm 6.1: Pseudo code for 3D-DWT.

```
(1)   Load 3D data set into V
(2)   [x y z] = size(V)
(3)   for k = 1 to z do
(4)         apply 2D-DWT for each plane in Z-axis
(5)   end for
(6)   for i = 1 to x do
(7)         for j = 1 to y do
(7)               apply 1D-DWT for all vectors corresponding
                  to each pixel in XY plane
(10)        end for
(11)  end for
```

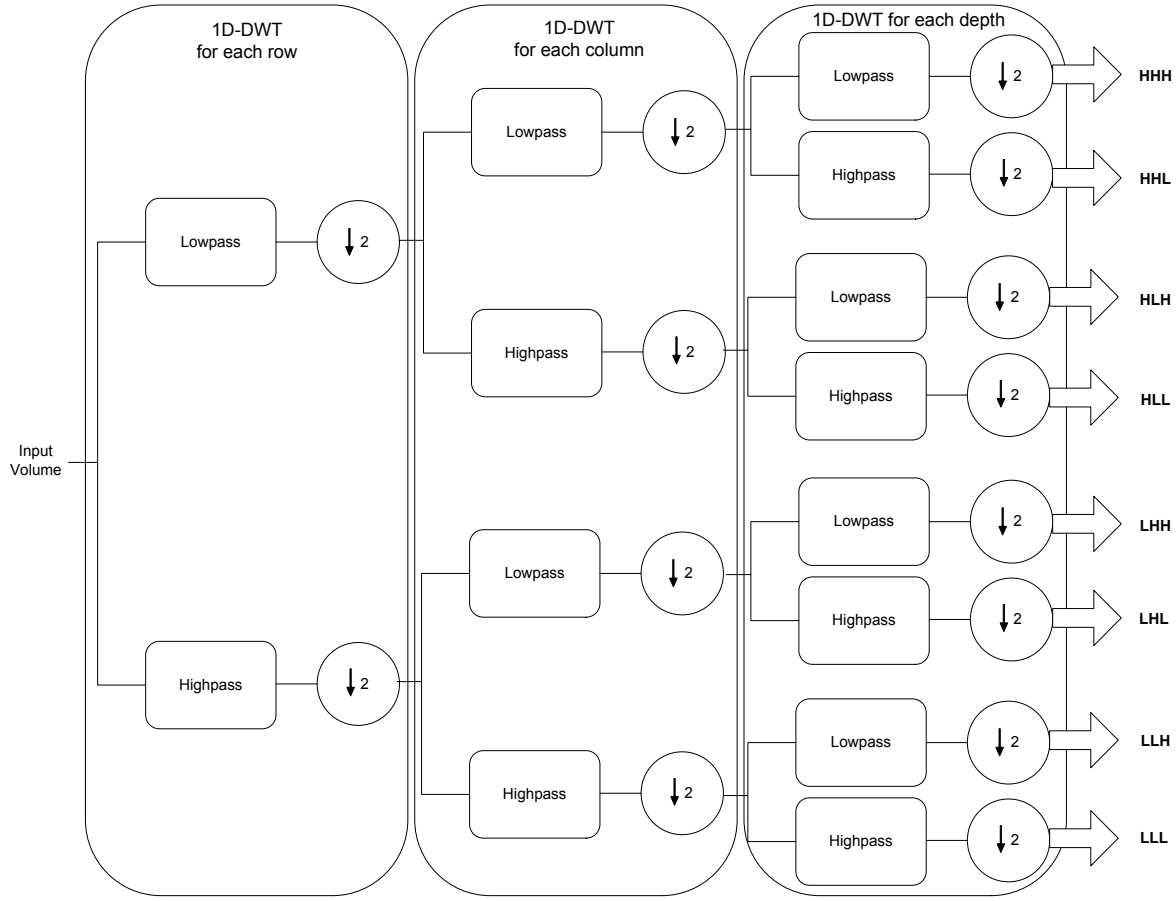

Fig. 6.2: Haar filter architecture for 3D-DWT.

Applying segmentation techniques on 2D slices requires more time compared to the time required in 3D volumes based approaches. For example, the required time to look for the best slice in NEMA IEC body phantom which includes the spheres in full diameters is not required in 3D volume segmentation processes. As well as real clinical data, ROI used to be clearly visualized in any slice and the required time to locate the specific slice that includes a clear view of the ROI is avoided using 3D segmentation techniques. The main drawbacks

for using 2D wavelets in medical image feature extracting is that the features occurred along z-axis are not extracted, where 3D wavelet solves this and extract those features properly.

Segmented volume for NEMA IEC body phantom using 3D-thresholding is illustrated in Fig 6.3(a), 3D-wavelet technique is applied on the same phantom data and the selected spheres are detected as illustrated in Fig 6.3(b). Another example of applying 3D-DWT on a real clinical CT images is illustrated in Fig 6.3(c).

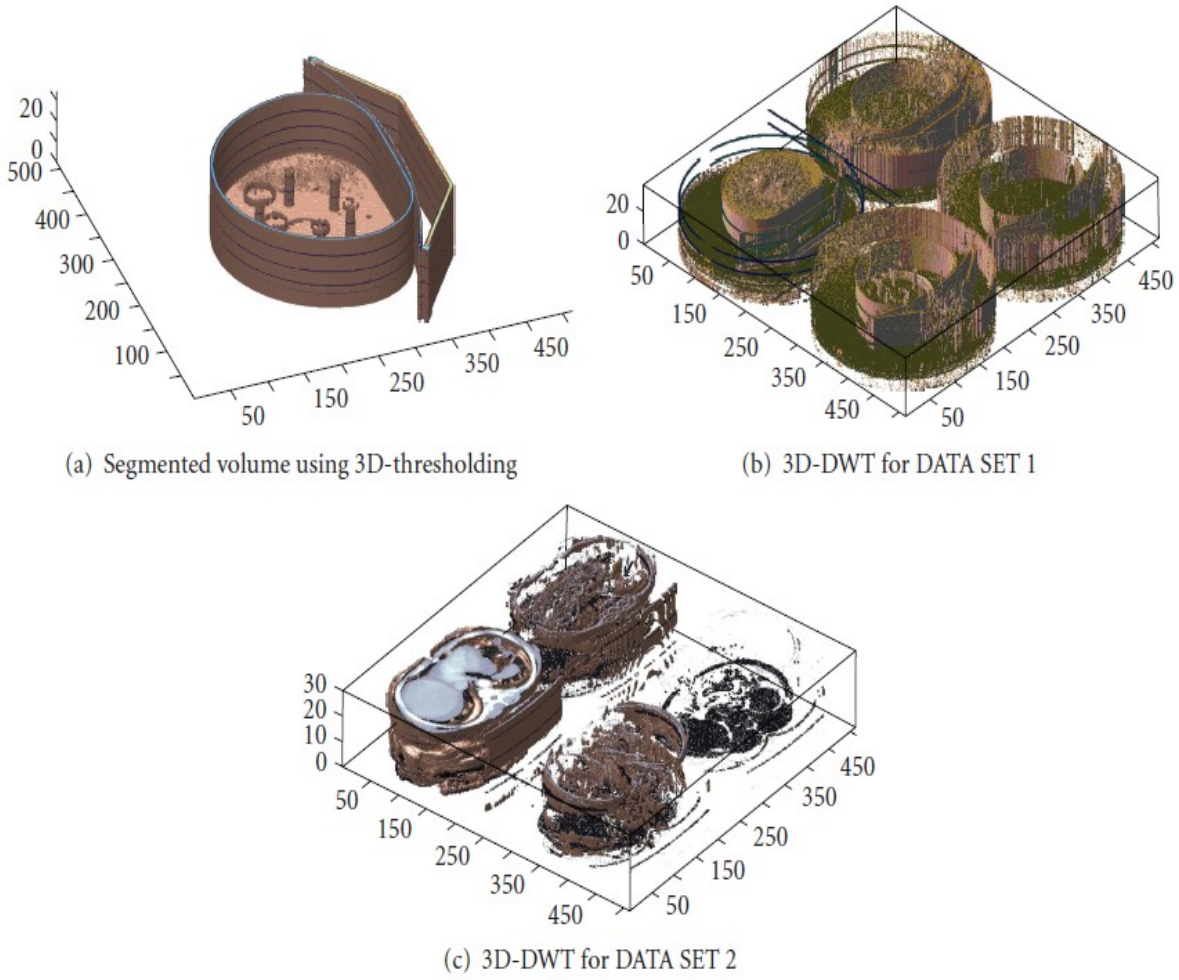

(a) Segmented volume using 3D-thresholding

(b) 3D-DWT for DATA SET 1

(c) 3D-DWT for DATA SET 2

Fig. 6.3: 3D segmentation techniques.

6.4. 3D Hidden Markov Model

Over the past years, HMMs have been explored as efficient statistical modeling techniques in speech, image and video understanding, because observed signals can be modeled through a first order Markov process. In this section, 3D-HMMs in its general form will be introduced.

Assume a 3D point $(i\ ,j\ ,k)$, where *i,j* and *k* are coordinates along the *X,Y* and *Z* axes respectively. A lexicographic order of the 3D point is defined in equation (6.11):

$$(\acute{\imath}\ ,\acute{\jmath}\ ,\acute{k}) < (i\ ,j\ ,k)\ ,if \begin{cases} \acute{k} < k \\ or \quad \acute{k} = k, \acute{\jmath}\ < j \\ \acute{k} = k, \acute{\jmath}\ = j, \acute{\imath} < i \end{cases} \tag{6.11}$$

The observed signal value at the point (*i,j,k*) has been denoted by $u_{i,j,k}$ and its hidden state by $s_{i,j,k}$. The model attempts to capture the statistical dependencies among 3D points through the state transition probability illustrated in equation (6.12) [122]:

$$P\{S_{i,j,k} = l | (S_{\acute{\imath}\ ,\acute{\jmath}\ ,\acute{k}}, U_{\acute{\imath}\ ,\acute{\jmath}\ ,\acute{k}}) : (\acute{\imath}\ ,\acute{\jmath}\ ,\acute{k}) < (i,j,k)\} = a_{p,m,n,l} \tag{6.12}$$

Where $(\acute{\imath}\ ,\acute{\jmath}\ ,\acute{k})$ are all points proceeding $(i\ ,j\ ,k)$ in the lexicographic order. Because of the Markov property, there are three preceding points p_1,p_2 and p_3 that affect the state of point $(i\ ,j\ ,k)$ as shown in the graphical illustration for the model in Fig 6.7. The hidden states of the three neighbouring points are $s_{i-1,j,k} = p$, $s_{i,j-1,k} = m$, $s_{i,j,k-1} = n$ separately.

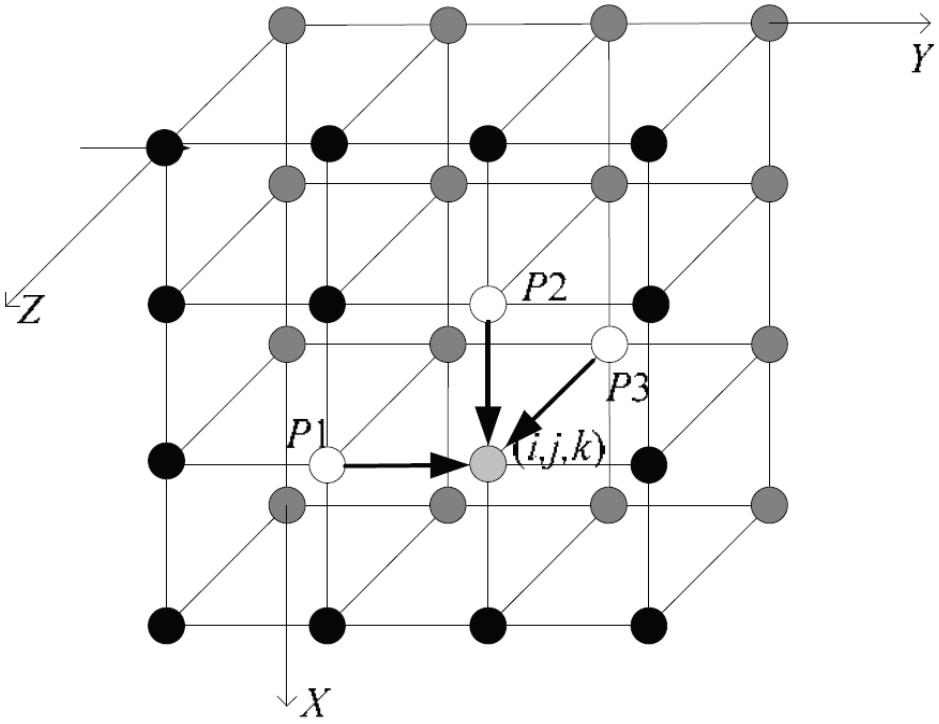

Fig. 6.4: 3D HMM graphical illustration [122]. *p1,p2,p3* are three neighbouring points that affect the state at (i,j,k).

An example of applying 3D-HMMs on a *64×64×8* sub-block contains the second biggest sphere (28 mm diameter) from NEMA IEC body phantom has been illustrated in Fig. 6.8. It can be seen that the sphere is properly detected but in a non-logical shape, it is close to be a cylinder rather than a sphere. This is due to the thickness of CT slice, according to the phantom description provided in [100], each pixel in the output images is equivalent to 1 mm^2, and the slice thickness of this data is 5mm. Therefore, if the sphere edge thickness is less than 5mm, the visualization will look like a cylinder. The surrounding objects seen in Fig. 6.8 are noise due to the scanner itself and HMMs classify them in the same class containing the 28 mm sphere.

Fig. 6.5: 3D HMM on 64 × 64 × 8 sub-block from NEMA IEC body phantom

In Fig. 6.8, the expected output was different than the illustrated one, this is due to many factors. The most important difference is the open top part in Fig. 6.8, this is due to the handles that fix the sphere in its exact location in NEMA IEC body phantom which is illustrated in Fig. 6.9(a). Fig. 6.9(b) illustrates the visualized NEMA phantom volume using Matlab® without any transformation.

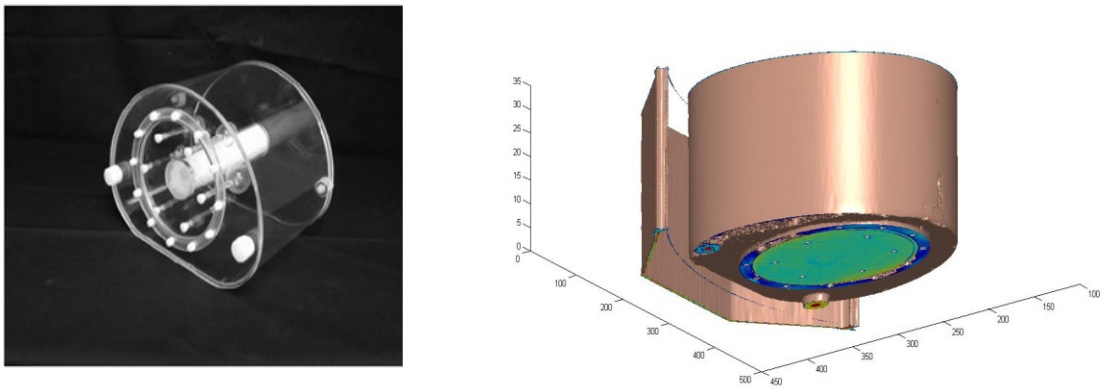

(a) (b)

Fig. 6.6: (a) NEMA IEC body phantom , (b) NEMA IEC body phantom after stacking all slices.

Slice thickness is playing a very important rule here; a group of layers from the original input volume has been replaced by one slice evaluating one of them. This leads to a big data and contouring loss in the segmented volumes and can be avoided by reducing the slice thickness during the body scan. In the example illustrated in Fig. 6.8, *64×64×8* sub-block from NEMA IEC body phantom has been segmented, and the input sub-block has been chosen manually. Choosing the best group of slices which evaluate sphere2 (28 mm diameter) is also important and can affect the output performance.

6.5. 3D Segmentation Techniques Comparison

Applying segmentation techniques on 2D slices requires more time compared to the time required by 3D volume-based approaches. The time required to look for the best slice that includes the spheres in full diameters is not required in 3D volume segmentation processes.

Segmented volume for the NEMA IEC body phantom presented in previous chapters using different 3D segmentation techniques has been illustrated in Fig. 6.6 and the selected spheres are detected. Table 6.1 compares the errors in spheres diameters using 3D segmentation techniques with the existing measurements using 2D techniques for slice number 19. ED has been also used here to measure the spheres diameters and calculate the error percentages for each technique, spheres diameter error percentages have been calculated according to equation (4.16). The inner diameter has been calculated with the 3D techniques based on the measured outer diameter and the spheres thickness.

Table 6.1: 3D segmentation Performance for measuring the error percentages for each slice diameter.

Diameters (mm)	10	13	17	22	28	37	Processing time
2D Wavelet	-2.9	-2.46	1.35	0.82	0.29	0.05	0.69 seconds
2D Curvelet	2.65	1.62	1.07	-0.82	-0.33	-0.09	12.6 seconds
2D HMM (Spatial)	1.5	0.8	0.1	0.8	0.04	1.0	2007.3 seconds
3D Thresholding	0.59	0.77	0.17	1.11	2.2	6.08	45.0 seconds
3D DWT	-2.67	-1.93	-0.74	4.75	3.37	0.77	280.3 seconds
3D HMM	1.01	0.71	0.54	0.27	0.03	<0.01	22080.6 seconds

It can be seen from Table 6.1 that 3D techniques overcomes the 2D techniques on average, especially for the 3D HMMs. The major problem of applying HMMs in it 2D mode or 3D mode is the long computational time which is much smaller using other available techniques. This is due to the training process in HMM, where each pixel used to be

compared with all other pixels to decide which class it is used to belong. HMMs overcome the other available techniques in two terms: (1) *The accuracy of HMMs in detecting objects and segmenting them properly with the least error.* (2) *HMMs are more automated compared to all available techniques, where no pre-processing or post-processing steps are required*.

This computational time problem is occurred also in the other 3D segmentation techniques such as 3D-DWT due to the large amount of data used. Chapter 7 illustrates acceleration methods for medical image segmentation techniques, this makes the process faster and the patients will be able to take their scan results directly after the scan.

6.6. Summary

MRA has proven promising results in chapter 4 including wavelets and curvelets transforms, these transforms segment the testing data properly. HMMs in chapter 5 overcome the other techniques especially for the automatic segmentation process. All the proposed 2D segmentation techniques were promising and can be applied in real clinical applications for segmenting human scans. 3D segmentation techniques introduced in this chapter to achieve more realistic and accurate results, where the 3D scans are illustrated as they are in real to facilitate the radiologists analyzing process.

A novel and sophisticated segmentation system was developed for 3D data segmentation in this chapter. The developed techniques within the system have been tested on NEMA IEC phantom data. The system used to quantify tumours within the data of predefined volumes, and these results were compared with those obtained from 2D

approaches such as curvelets. Statistical models using 3D hidden Markov models have been also investigated for segmenting medical volumes; the weakness of HMMs was its long computation time required for the calculation of their models which was much larger compared with the other evaluated techniques.

Real clinical validations and segmented medical volumes for patients diagnosed with cancer will be further analyzed in chapter 8 of this thesis.

Chapter 7

Medical Image and volume Segmentation Acceleration

7.1. Introduction

At present, segmentations are mainly performed manually by medical specialists. This task appears simple, but the reality is that an in-depth knowledge of anatomy and physiology is required. Essentially, the expert observes a particular image, determines borders between regions and classifies each region. This is commonly completed slice by slice for a 3D volume and lead to slow down the segmentation algorithms performance while images with large number of features such as medical images form a high dimensional data array. The measurement of dozens of features that represent data similarities causes the redundancy of information, which is one of the problems related to high dimensional data.

FR techniques provide efficient methods for simplifying multi-dimensional data by replacing a large number of variables with a smaller number of new variables that preserves most of the data's features and without that much of information loss [123][124]. FR in

medical image processing is a vital part of improving real-time performance of segmentation algorithms. It aims at reducing the size of medical images in terms of dimensionality; hence, it is an efficient way of reducing computational time and storage demands for image processing algorithms. 2D-FR techniques aim to reduce the coefficients of pixel values in a single image and the transformed image has reduced features [123].

In this chapter, different 3D segmentation techniques have been used for segmenting medical volumes in less computational time using different FR techniques, those FR techniques are used to reduce dimensionality of the testing volumes. The structure of this chapter is organized as follows: the mathematical background for the implemented FR techniques is presented in section 7.2. Section 7.3 presents the results and analysis of the proposed techniques. Finally, the work implemented in this chapter has been summarized in section 7.4.

7.2. Dimensionality and Feature Reduction Techniques

The use of FR techniques in this research aims to reduce the dimensionality of medical volumes. Many renowned FR techniques are available; some of them are highlighted in this section because of their simplicity and suitability in the proposed application.

7.2.1. Gaussian Pyramid Reduction

GPR is a hierarchical structure of low-pass filters, pixels comprising the upper levels in the Gaussian Pyramid are achieved by averaging pixels that comprising the lower level in the

pyramid [125]. The pyramid base (level 0) is an *m* x *n* matrix contains pixel values that indicate the intensity of the original image without any transformation.

As illustrated in Fig. 7.1, the upper levels are reduced or low-pass filtered versions of lower levels. Each value within level g_i is computed as a weighted average of values in level g_{i-1} within a *5* x *5* window [126].

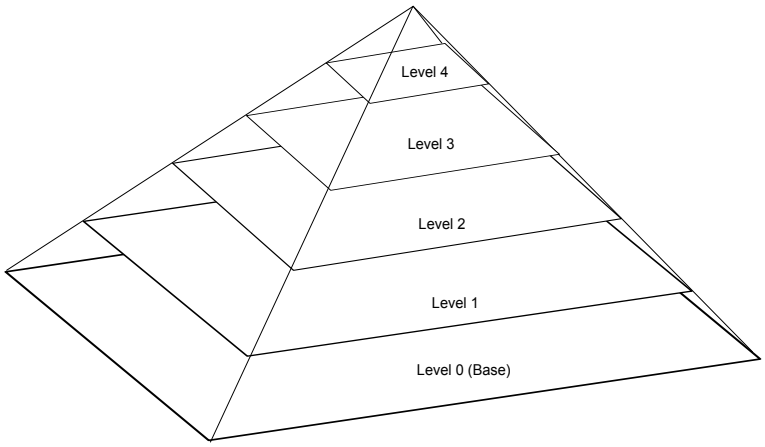

Fig. 7.1: Gaussian pyramid representation in spatial domain.

Fig. 7.2 illustrates the process of applying GPR in one dimension where each row of black squares represents nodes within one level of the pyramid. It can be seen that node spacing doubles from level to level while the same weighting pattern or kernel as described in [126] is used to generate all levels. This kind of reduction has been implemented and applied to the proposed datasets using Matlab®, the level-to-level averaging function is performed by a Matlab® built in function `REDUCE` which can be used as follow:

$$g_k = REDUCE\ (g_{k-1}) \qquad (7.1)$$

For a filter kernel *w[i,j]* of dimension *5* x *5* and reduction factor of 4, function `REDUCE` is applied to image *I* as illustrated in equation (7.2):

$$REDUCE\ (I)[i,j] = \sum_{m-1}^{5} \sum_{n-1}^{5} w[m,n] \times I[2i+m, 2j+n] \qquad (7.2)$$

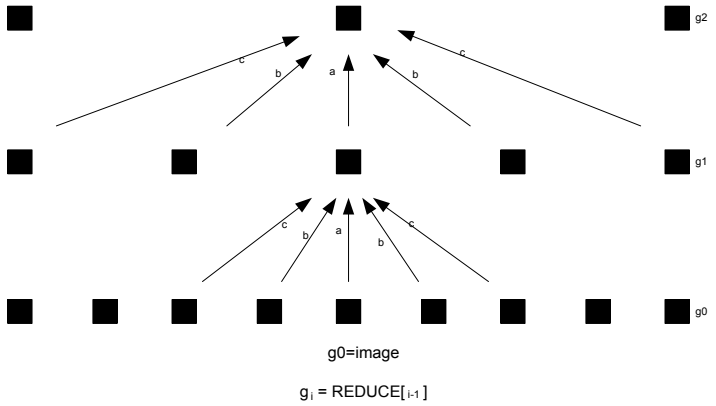

Fig. 7.2: 1D graphic representation of the Gaussian Pyramid reduction.

This technique reduces image dimensions at each level by half while retaining the most image features and allowing image processing algorithms to perform faster. Fig. 7.3 illustrates an example of applying the first and second levels of GPR on a real DICOM slice for the human body.

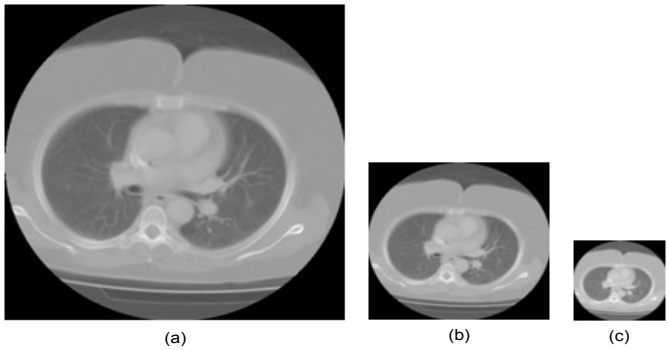

Fig. 7.3: (a) Original image (512 x 512), (b) First level of GPR (256 x 256), (c) Second level of GPR (128 x 128).

7.2.2. Discrete Wavelet Transform

DWT has been introduced in section 4.3 of this thesis as an MRA feature extraction technique and joined with pre-processing and post-processing steps to be a segmentation technique that can be applied for medical image segmentation and edge detection. DWT has proved promising results in image compression [127], face recognition [128] and many other applications including feature reduction. The low-pass filter output in 2D wavelet transform evaluates the averages of the image. In other words, this output is a similar version of the input image but with reduced dimensionality to the half.

Along with the conventional DWT applications in the field of medical imaging, DWT decomposition at different levels provide the capabilities of transforming high dimensional image into reduced dimensional image preserving most of the image features. Thus the decomposition method can be utilized as one of the robust dimension reduction techniques in image processing. The mathematical background of DWT and the use in medical images has been briefly introduced in section 4.3. Fig. 7.4 and Fig. 7.5 illustrate the output of 2D DWT and an example of DWT for reducing medical dataset features respectively.

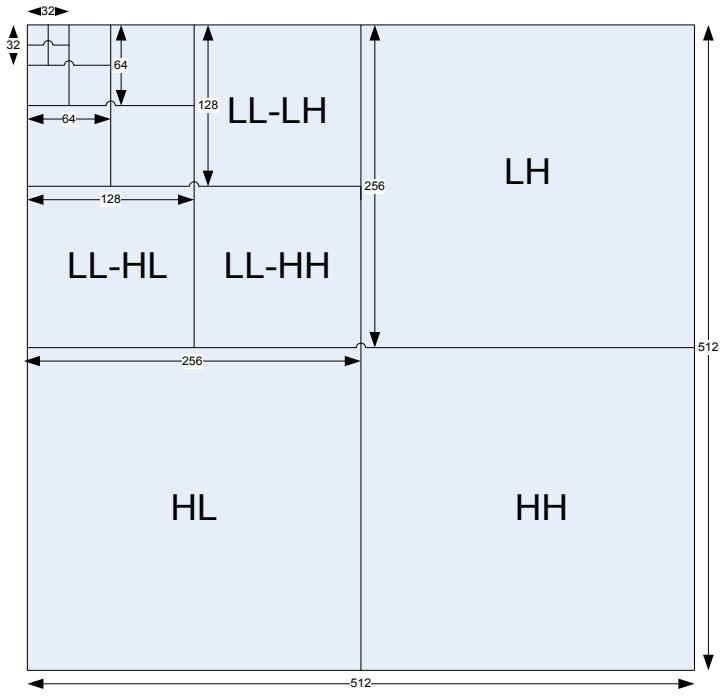

Fig. 7.4: After each single wavelet decomposition level, the image dimensions reduced by 50%.

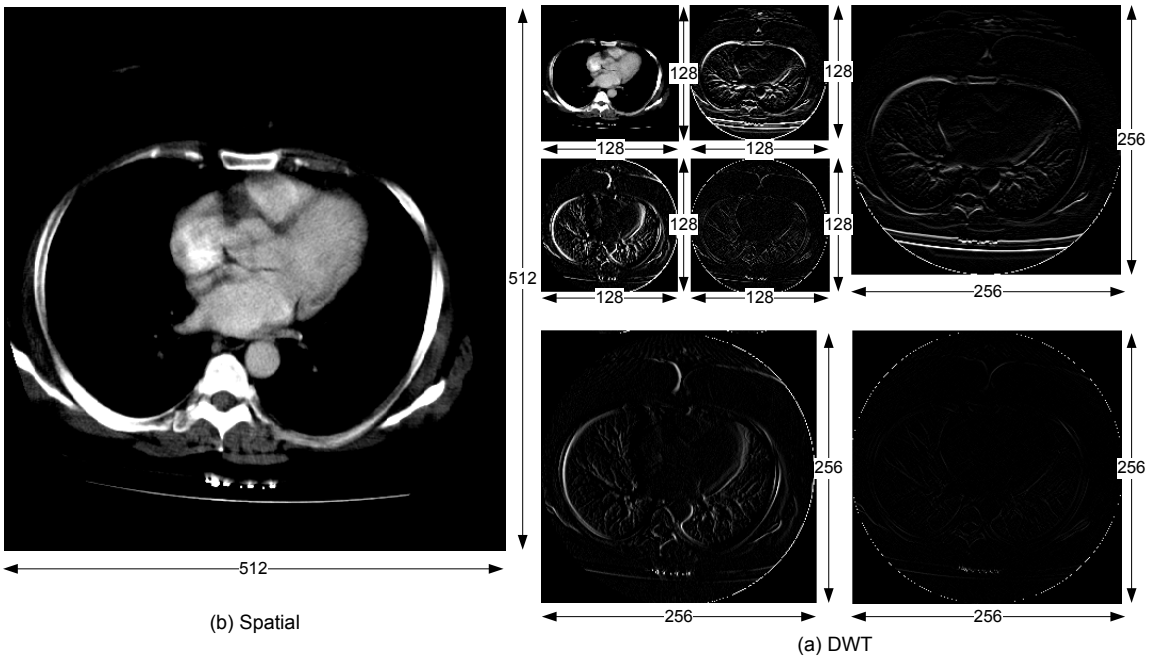

(b) Spatial

(a) DWT

Fig. 7.5: DWT for medical image feature reduction.

Looking at the second decomposition level output in Fig. 7.5 (LL filter output), it looks very similar to the input image with preserving the features to the original input. The dimensionality of the transformed output is equal to the quarter of the input image dimensions. This technique is very promising if looking into broader aspect of dimension reduction for 3D medical volumes. In more obvious way; 2D DWT can be used to reduce all comprising slices to smaller dimension and then construct the 3D volume. This can be applied but the third dimension or the number of slices will not be affected. 3D DWT can be used here with medical volumes to achieve the most utilized feature or dimensionality reduction with an accurate volume image, that retains most of the important features for anatomical study and faster for 3D processing.

7.2.3. Principal Components Analysis

Principal Components Analysis (PCA) is most conventionally used technique for dimensionality reduction in the field of image processing. It is widely used in face recognition for its ability to reduce the data set dimensionality while retaining as much characteristic features as possible. According to *Burt* and *Adelson* [126], PCA can be used in medical volume segmentation for a number of successive slices from an acquisition system. It can highlight the most important features in the first two eigenslices and the rest contains only least important features. PCA is a classical linear projection aiming at finding orthogonal principal directions of a data set by solving an eigenvalues problem. A small number of principal components are retained on a linear and low dimensional subspace while a large number of minor components are discarded [123].

An image can be represented by an *m* x *n* matrix of pixels values, each corresponding image is converted into a column vector (z_i) by concatenating successive rows transposed, where $(Z = z_1, z_2, ..., z_N)$ is the training set of N images and $\bar{z}$ is the mean image vector [5]. Recalling the standard definition of the covariance matrix:

$$R = \frac{1}{N}\sum_{i=1}^{N}(z_i - \bar{z})(z_i - \bar{z})^T = \Phi\Phi^T \qquad (7.3)$$

$$\bar{z} = \frac{1}{N}\sum_{i=1}^{N} z_i \qquad (7.4)$$

Let $(E = e_1, e_2, ..., e_r)$ be a matrix formed by *r* eigenvectors corresponding to the *r* largest eigenvalues. Only e_r eigenvectors should be chosen, which have the highest eigenvalues, the higher the eigenvalue (eigenslice) the more characteristic features of an image does the particular eigenvector describe. Images with low eigenvalues explain only a small part of features which can be omitted [129]. Therefore, the first eigenslices is regularly chosen for evaluating the set of input slices.

For a set of original images *Z*, the reduced feature vectors $(X = x_1, x_2, ..., x_N)$ are obtained by projecting them into the PCA-transformed space following the linear transformation illustrated in equation (7.5) where x_i is the result and *E* is the eigenvector in the corresponding mean adjusted data matrix:

$$x_i = E^T(z_i - \bar{z}) \qquad (7.5)$$

The method in equation (7.3) leads to extremely large and computationally challenging covariance matrices as the covariance matrix R has the dimensionality N^2 x N^2. This problem is solved by the scheme proposed by *Turk and Pentland* [130] in which the covariance matrix is calculated using the formula $R = \Phi\Phi^T$. The advantage of this method is that one has to evaluate only *M* numbers and not N^2. Usually, $M << N^2$ as only a few principal components will be relevant.

A group of images can be used as an example of applying PCA for dimensionality reduction. Each image is converted into a column vector *X* by concatenating successive rows transposed. According to the algorithm presented by *Gonzalez et. al.* [131], each image vector is stacked into a training matrix ($X=x_1,x_2,...x_5$). PCA is applied to the data *X* which returns principal components based on the eigenvectors corresponding to the highest eigenvalues. The following presents the implementation steps of applying PCA for image dimensionality reduction:

Step 1: As illustrated in Fig. 7.6, column vectors from all image matrices comprise matrix A.

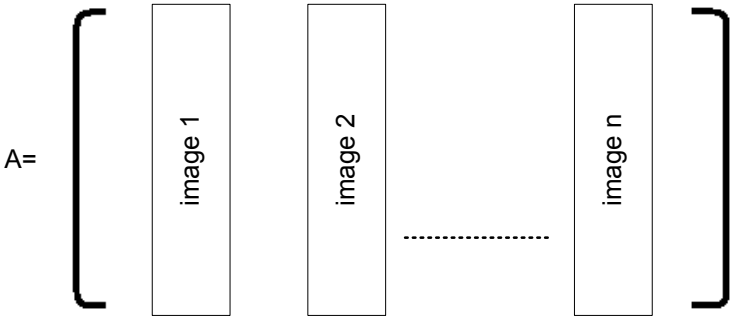

Fig. 7.6: Form a column vector matrix.

Step 2: Calculate mean image and subtract it from each image vector in A as illustrated in Fig. 7.7.

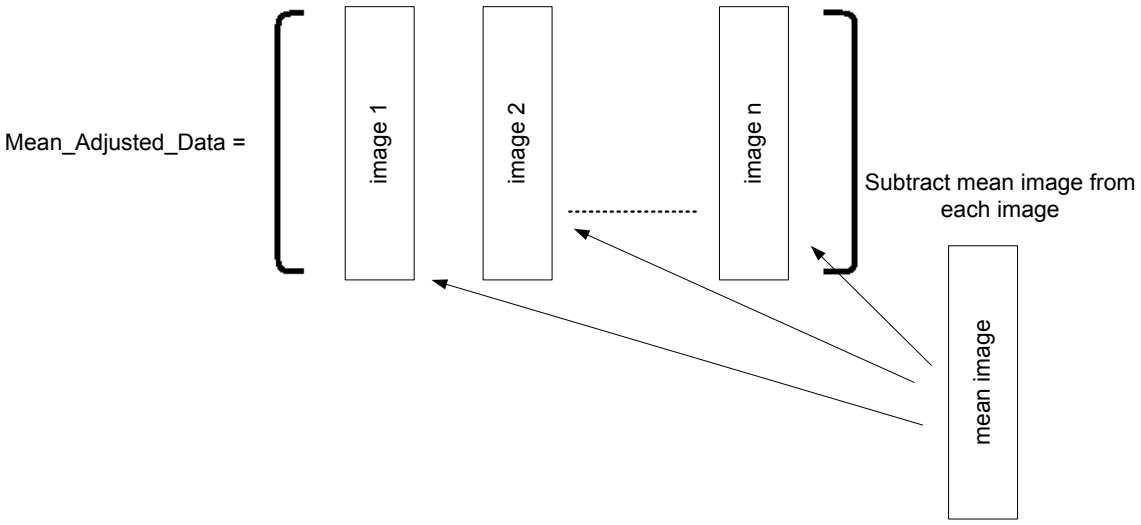

Fig. 7.7: Calculate the mean adjusted data.

Step 3: Calculate covariance matrix of mean adjusted data using equation (7.6):

$$\mathrm{Cov} = \mathrm{MeanAdjustedData}^{\mathrm{T}} \times \mathrm{MeanAdjustedData} \quad (7.6)$$

Step 4: Calculate eigenvectors and eigenvalues of the covariance matrix

Step 5: Select principal components using eigenvectors corresponding to the highest eigenvalues.

As mentioned before, Matlab® has been used in this research to acquire the results and validate the techniques; a built-in Matlab® command which is (`princomp`) has been used to calculate the principal components of a given data as follows:

```
[Coeff, Score, Latent] = princomp(A) ;
```

`princomp` command returns three variables: `Score`, `Coeff` and `Latent`:

- **`Score:`** The principal component `Score` is the representation of *A* in the principal component space. Rows of `score` correspond to observations and columns to components.

- **`Coeff:`** `Coeff` returns the principal component coefficients (eigenvectors). `Coeff` is a *p* x *p* matrix, each column containing coefficients for one principal component. The columns are in order of decreasing component variance.

- **`Latent:`** `Latent` returns the principal component variances (or the eigenvalues of the covariance matrix of A).

Fig. 7.8 illustrates an example of applying PCA on five DICOM slices from a CT scanner, it can be seen that the first principal component of the PCA transformed images has significant portion of contrast/feature details and it decreases rapidly from the second component or eigenslice in PCA domain. Image features are illustrated in Fig. 7.8 in decreasing order due to the eigenvalues of the input data.

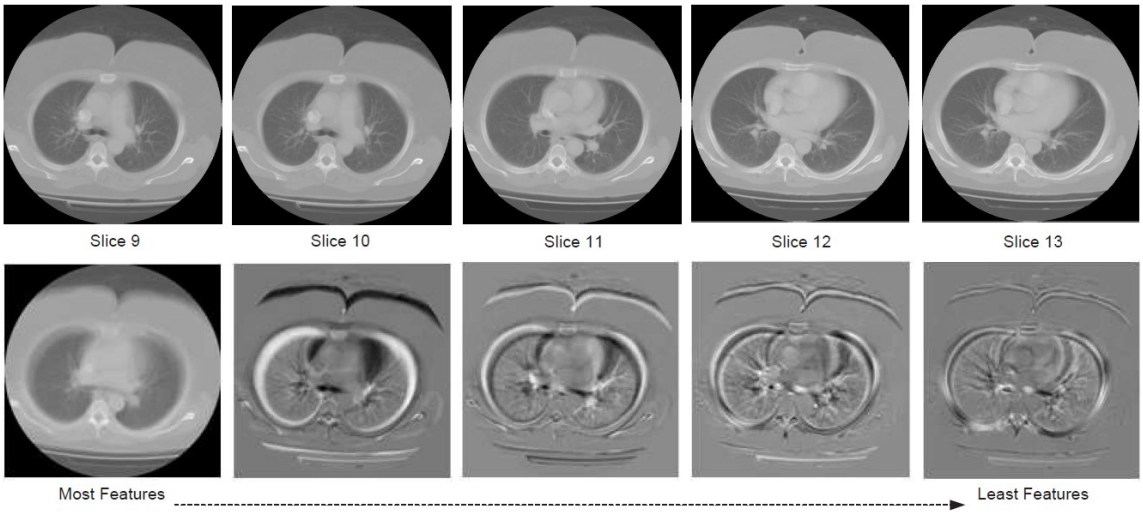

Fig. 7.8: PCA for 3D volume feature reduction

Table 7.1 illustrates the eigenvalues for each input image shown in Fig. 7.8 in their respective order. The first eigenvalue which represents PCA eigenslice 1 is very large due to the greatest data variance in the first principal component. One image will be selected to evaluate the whole group; the selection process has been done manually in this research

Table 7.1: Eigenvalues for all experimented images.

Slice 1	Slice 2	Slice 3	Slice 4	Slice 5
7.34e-04	1.27e-05	3.70e-06	1.46e-06	8.31e-07

7.3. Results and Analysis

The computational time of medical image segmentation is a very important issue, reducing it to the lowest value helps to make the segmentation system real time system. The long computational time problem has been mentioned in this thesis many times, it was long for

MRA including both ridgelet and curvelet transforms, and much longer with all the 3D segmentation techniques due to the huge amount of the tested data. HMMs in both 2D and 3D versions prove promising results and overcome the other techniques, but the weakness of HMMs was the long computational time for segmenting medical volumes.

One of the problems with high dimensional data is the redundancy of information through the measurement of dozens of features that represent the similarity of data. Many approaches have been used to solve the long computational time problem using different hardware and software accelerators.

FR reduction technique is one of the well-known software accelerators; it helps to reduce the computational time of the segmentation process by reducing the features of the experimented dataset. FR techniques provide efficient methods of simplifying multi-dimensional data. The reduced features images have reduced dimensionality hence it is an efficient way for reducing computation time and storage demands for medical image segmentation algorithms. For example, HMMs can be applied on a reduced dimensionality images instead of the full features volume to reduce the computational time.

Different experiments on different datasets have been carried out to validate the proposed FR techniques for medical image segmentation system. The proposed approach has been tested using the NEMA IEC body phantom which has been mentioned before as well as real CT chest data. All results have been measured using an HP Laptop with Intel Core i7 / 1.6 GHz processor and Graphic card NVIDIA® GeForce® GT 230M with 1GB dedicated DDR3 memory, and 4GB RAM.

7.3.1. 3D DWT Segmentation without Feature Reduction

3D wavelet technique is applied on the NEMA phantom and the included spheres are detected as illustrated in Fig. 7.9. Table 7.2 illustrates the spheres diameters errors using 3D DWT in spatial domain. Another example of applying 3D DWT on real CT images for the human chest data [96] is illustrated in Fig. 7.10 where the edges are detected and the comprising obstacles can be seen from different angles. The computational time for the first wavelet decomposition level of the chest volume is (280.26 seconds).

Table 7.2: Diameters percentages error using 3D-DWT on spatial domain for NEMA IEC phantom

Sphere Diameters	10 (mm)	13 (mm)	17 (mm)	22 (mm)	28 (mm)	37 (mm)
3D-DWT on spatial	-2.67	-1.93	-0.74	4.75	3.37	0.77

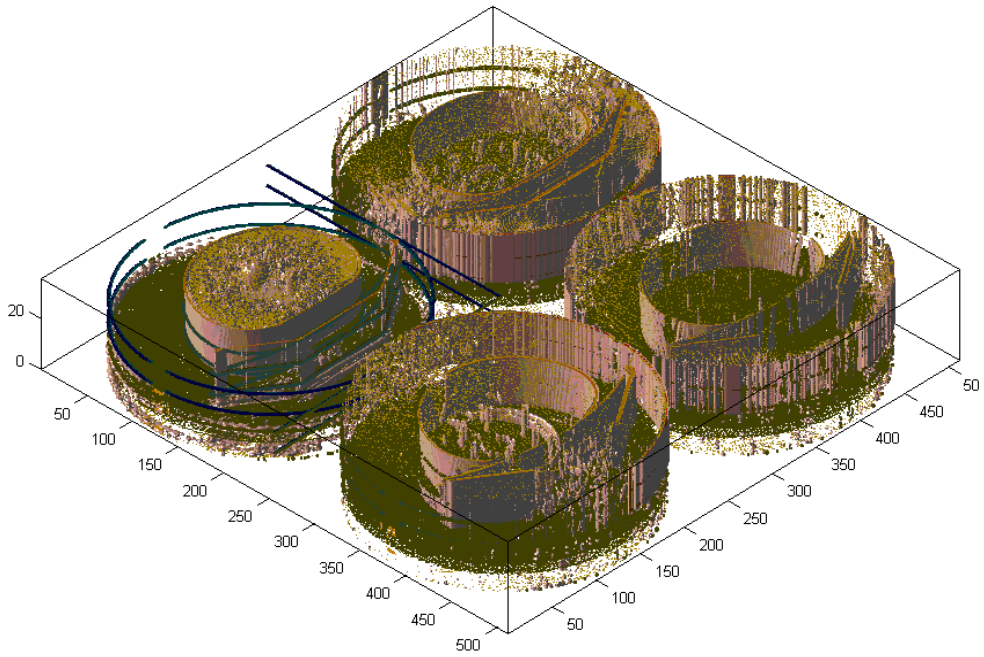

Fig. 7.9: Medical volumes in wavelet domain for NEMA IEC.

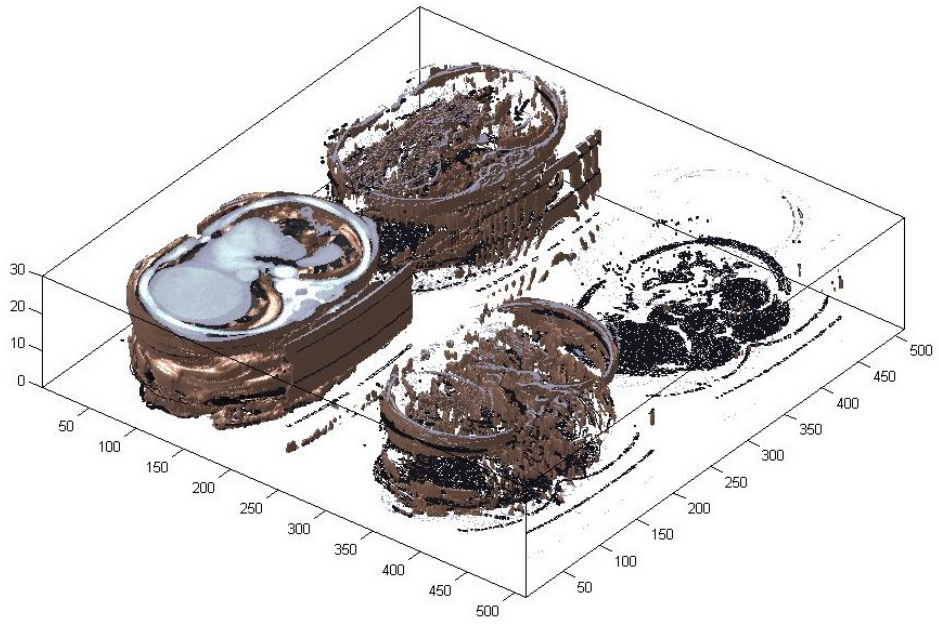

Fig. 7.10: Medical volumes in wavelet domain for real chest data.

7.3.2. 3D DWT Segmentation and PCA Feature Reduction

Fig. 7.11 illustrates real chest volume after FR using PCA followed by 3D DWT to explain how the reduced features volume looks like after reduction. The dimensionality has been reduced from *512* x *512* x *62* to *256* x *256* x *5* which is the dimensionality of the *LLL* wavelet filter output. PCA compresses each *7* slices together to produce one slice that includes most of their features.

The required computational time to apply 3D DWT on the reduced features volume using PCA is 168.38 seconds while PCA requires 3.3 seconds to reduce the dimensions. The overall time is 171.68 seconds which is less than the required time for segmenting the full features volume (280.26 seconds).

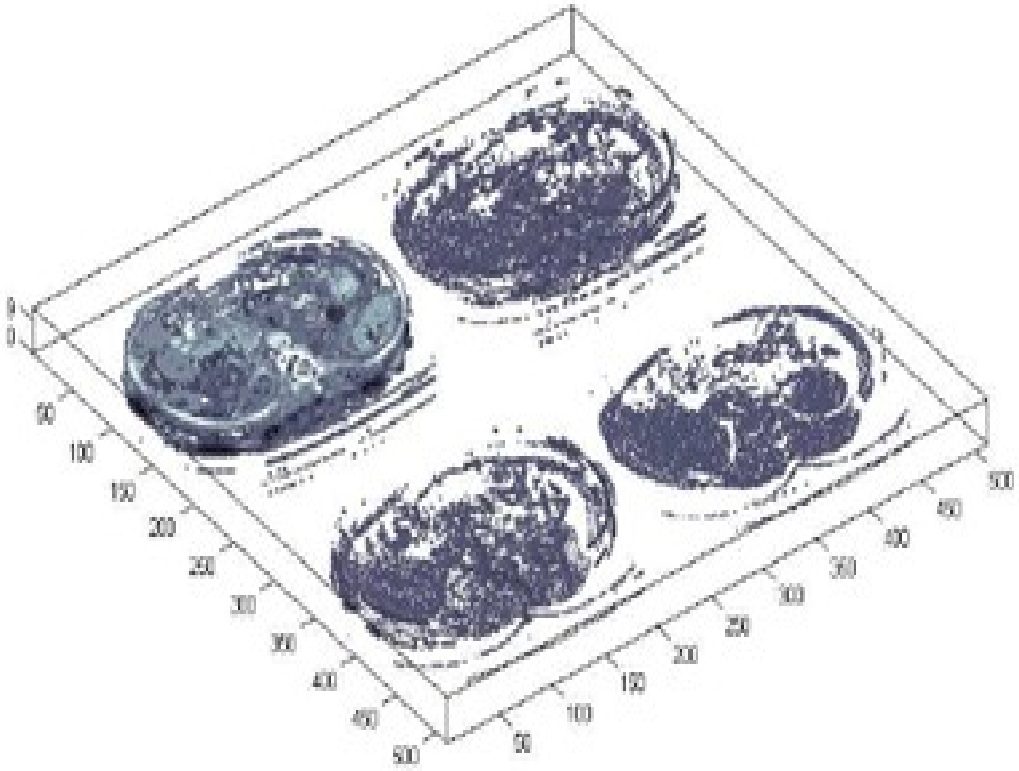

Fig. 7.11: Reduced feature chest volume after applying PCA followed by 3D-DWT.

According to the quality of the reduced features segmented volume using PCA, NEMA phantom has been tested and the detected spheres diameters have been measured. Table 7.3 illustrates the segmentation quality using 2D DWT after compressing the sub-volume in NEMA phantom which includes the whole spheres into one slice using PCA; this slice includes all the required features needed to measure the diameters (Fig. 7.12).

Table 7.3: Diameters percentages error using 3D-DWT on reduced volume using PCA

Sphere Diameters	10 (mm)	13 (mm)	17 (mm)	22 (mm)	28 (mm)	37 (mm)
2D-DWT using PCA	1.2	3.15	0.73	2.26	2.65	0.85

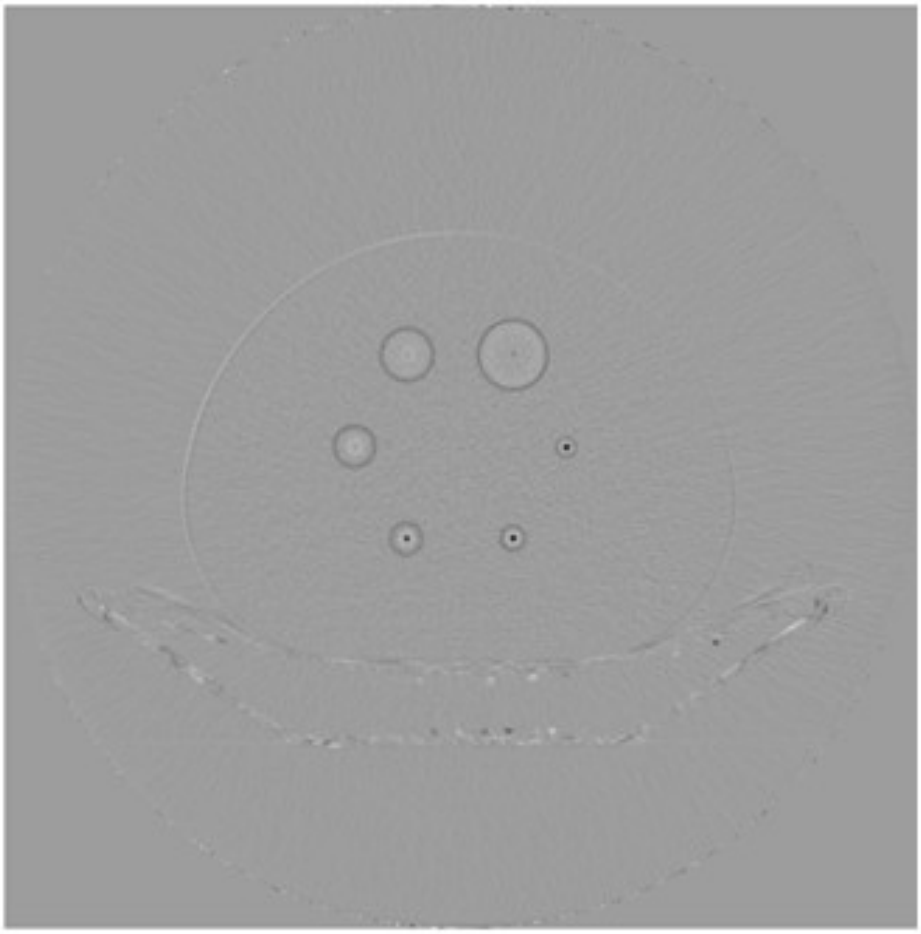

Fig. 7.12: The fifth PCA slice which includes most of the required features.

7.3.3. 3D DWT Segmentation and GPR Feature Reduction

The original dimensions for the real chest volume can be reduced using 2 levels of GPR from *512* x *512* x *62* to *128* x *128* x *62*, where each level of GPR reduce each slice dimensionality to the half, the output includes most of the features and without that much of data loss. 3D-DWT and thresholding technique can be then applied to the reduced features volume using GPR to segment the volume in less computational time.

Fig. 7.13 illustrates the real chest volume in wavelet domain with reduced features using GPR. The required computational time to apply 3D DWT on the reduced features volume using GPR is 67.20 seconds while GPR requires 22.25 seconds to reduce the dimensions. The overall time is 89.45 seconds which is much less than the required time for segmenting the full features volume (280.26 seconds).

One level of GPR has been also applied on NEMA phantom to reduce the dimensions from *512* x *512* x *35* to *256* x *256* x *35* as illustrated in Fig. 7.14. 3D DWT can be then applied to detect ROI and measure the diameters. Table 7.4 illustrates the error percentages of measuring the spheres diameters using 3D DWT and GPR.

Table 7.4: Diameters percentages error using 3D-DWT on reduced volume using GPR

Sphere Diameters	10 (mm)	13 (mm)	17 (mm)	22 (mm)	28 (mm)	37 (mm)
3D-DWT using GPR	3.85	2.69	1.41	1.05	0.94	0.93

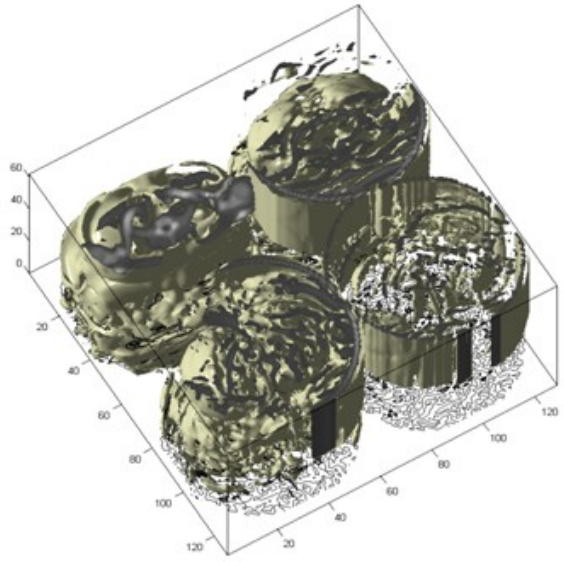

Fig. 7.13: 3D-DWT for real CT images after FR using GPR.

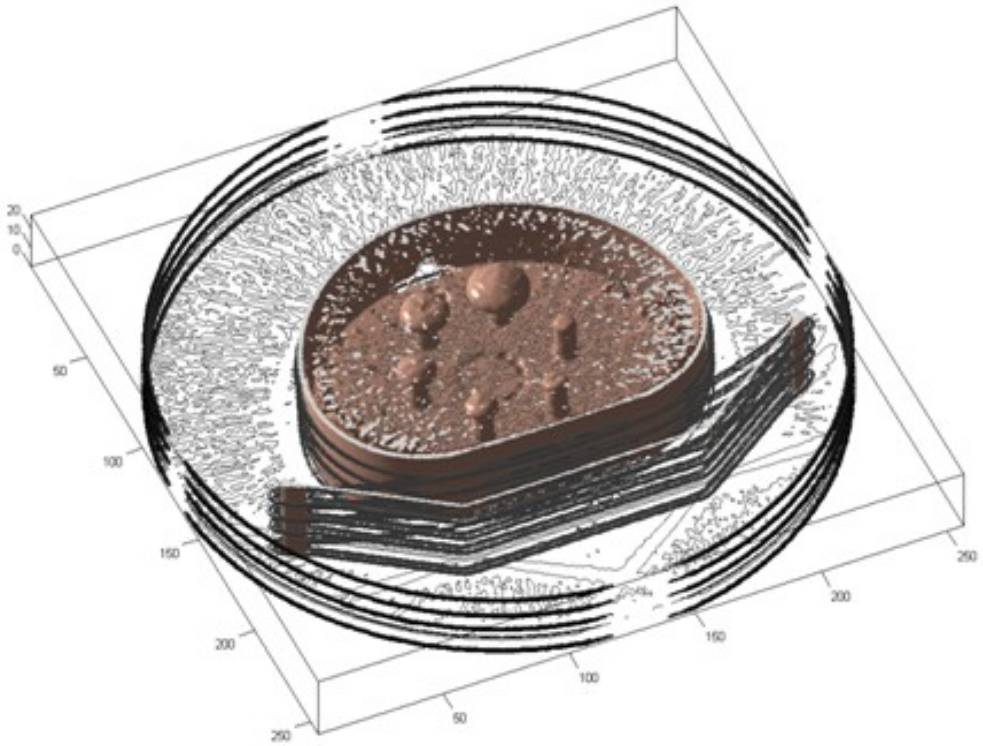

Fig. 7.14: Reduced features NEMA phantom using 1 level GPR.

7.3.4. HMMs Segmentation and PCA/DWT/GPR Feature Reduction

HMMs have been used to segment the reduced features images as illustrated in Fig. 7.15. Table 7.5 illustrates the required time for segmenting the reduced features real chest image using HMM for one slice. Applying 2-levels of DWT or GPR reduces the image dimensions into the quarter and the segmentation processing time into less than 2%. PCA is applied on 5 slices where ROI is predefined, HMM is then applied on the reduced features slice which includes all the required features instead of applying it on 5 slices.

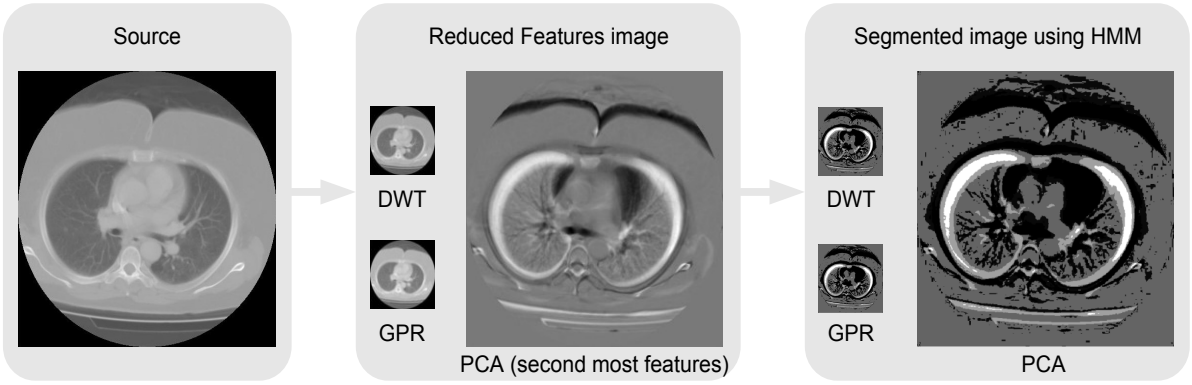

Fig. 7.15: Segmented images using HMM in different transforms

Table 7.5: Computational time using FR techniques (sec)

FR Technique	Time for FR	Time for HMM	Time for each slice	Time for full volume (62 slices)
Spatial domain	0	1355.24	1355.24	84024.9
DWT (2-levels)	0.695	22.17	22.87	1417.9
GPR (2-levels)	0.628	19.03	19.66	1218.9
PCA (5-slices)	0.957	1104.8	1105.76	13269.1

From Table 7.5, it can be seen that the best computational time is achieved using HMM on GPR, but GPR is affected by data loss problem as well as DWT at higher decomposition levels. PCA reduce the computational time by ~84% but still longer than the achieved time using the other FR techniques. The point is PCA can be generalized to be more efficient if applied on large number of slices such compressing the whole volume into one slice as in Fig. 7.12 where PCA compressing NEMA phantom into one slice to reflect the effects on the proposed system accuracy. Table 7.6 illustrates the segmentation quality using HMM after

FR techniques. Because of the overlapping in the spheres edges after compressing the volume into one slice using PCA, outer diameters have been measured instead of the inners, and inner diameters have been calculated based on the sphere edges thickness.

Table 7.6: NEMA diameters error percentages using HMM on reduced features volume with required time

Diameters	10	13	17	22	28	37	Time (sec)
HMMs on Spatial Domain	1.5	0.8	0.1	0.8	0.04	1	2007.3 (x 46 slices)
HMMs with 1 level of DWT	---	11.07	7.82	2.98	1.09	0.27	1321.1 (x 46 slices)
HMMs with 1 level of GPR	5.2	4.7	3.5	3.2	2.93	1.88	688.1 (x 46 slices)
HMMs with PCA (using outer diameters)	1.8	1.1	0.85	0.59	0.34	0.22	1108.1

From Table 7.6, it can be seen that accelerating the process is affecting the quality of the proposed system by different percentages. The errors achieved using both DWT and GPR reductions are higher than the spatial HMM but the required computational time is still less than 2/3 of the required time in spatial domain. Errors achieved using PCA and HMM are close to the spatial HMM and the required time is ~1.2% of what required in spatial domain, which is a very good accuracy and time reduction.

It can be seen from the previous sections that different computational times and spheres diameters' errors have been achieved using the proposed techniques. Table 7.7 illustrates a comparison study for the proposed techniques according to the quality of detecting ROI in NEMA body phantom and other available techniques.

Table 7.7: NEMA spheres diameters error percentages using the proposed techniques and other available techniques

Sphere Diameters	10 (mm)	13 (mm)	17 (mm)	22 (mm)	28 (mm)	37 (mm)	Time (seconds)
K-means [1]	-4.7	-4.0	-1.94	-1.86	-1.71	-1.7	---
MRFM [1]	-2.5	-3.0	1.4	1.31	1.28	1.27	---
3D Thresholding *	0.59	0.77	0.97	1.11	2.2	2.28	45.0 x 46
3DDWT-Spatial *	-2.67	-1.93	-0.74	4.75	3.37	0.77	280.3 x 46
2DDWT-PCA *	-1.2	-3.15	0.73	2.26	2.65	0.85	2.07
3D-DWT using GPR	3.85	2.69	1.41	1.05	0.94	0.93	53.7 x 46
HMM / Spatial Domain	1.5	0.8	0.1	0.8	0.04	1	2007.3 x 46
HMMs with DWT	---	11.07	7.82	2.98	1.09	0.27	1321.1 x 46
HMMs with GPR	5.2	4.7	3.5	3.2	2.93	1.88	688.1 x 46
HMMs with PCA *	1.8	1.1	0.85	0.59	0.34	0.22	1108.1

* ≡ *using outer diameters.*

From Table 7.7, outer diameters have been used in many cases such as 3D segmentation techniques and with the reduction using PCA. Therefore, the inner diameters error have been calculated based on the thickness of the spheres edges. All spheres diameters detected using 3D-thresholding were over estimated by (0.5-2.5 %) and the error was increasing while the sphere diameter increasing.

By using 3D wavelet transform for segmentation, spheres diameters are reduced to the half with each decomposition level of wavelet transform. First level of DWT has been applied on NEMA phantom in three different domains (spatial, PCA, and GPR) and the measured diameters were doubled to produce a fair comparison with the other available techniques. By applying one decomposition level of 3D-DWT on spatial domain and using the LLL filter output, underestimated percentages have been achieved for the three small spheres (10, 13, and 17 mm) and overestimated percentages for the three big spheres (22, 28, and 37 mm).

Outer diameters are also measured in the case of applying 2D-DWT on reduced features volume using PCA and over estimated results have been achieved for all spheres except (10mm and 13mm). Applying 3D DWT on the reduced features volume using GPR produce results which are completely opposite to 3D-thresholding technique where all measurements are under estimated and the error decreased while the spheres diameter are increased. In Fig. 7.16, the percentage error computed between the actual spheres diameters and the results obtained using all methodologies illustrated in Table 7.7 for each of the six tumours inserts is plotted.

7.4. Summary

Different FR techniques have been implemented to accelerate the segmentation process for medical volumes and speedup the computations of the slowest system block. FR is a key part in image processing that reduces the curse of dimensionality hence proving an efficient

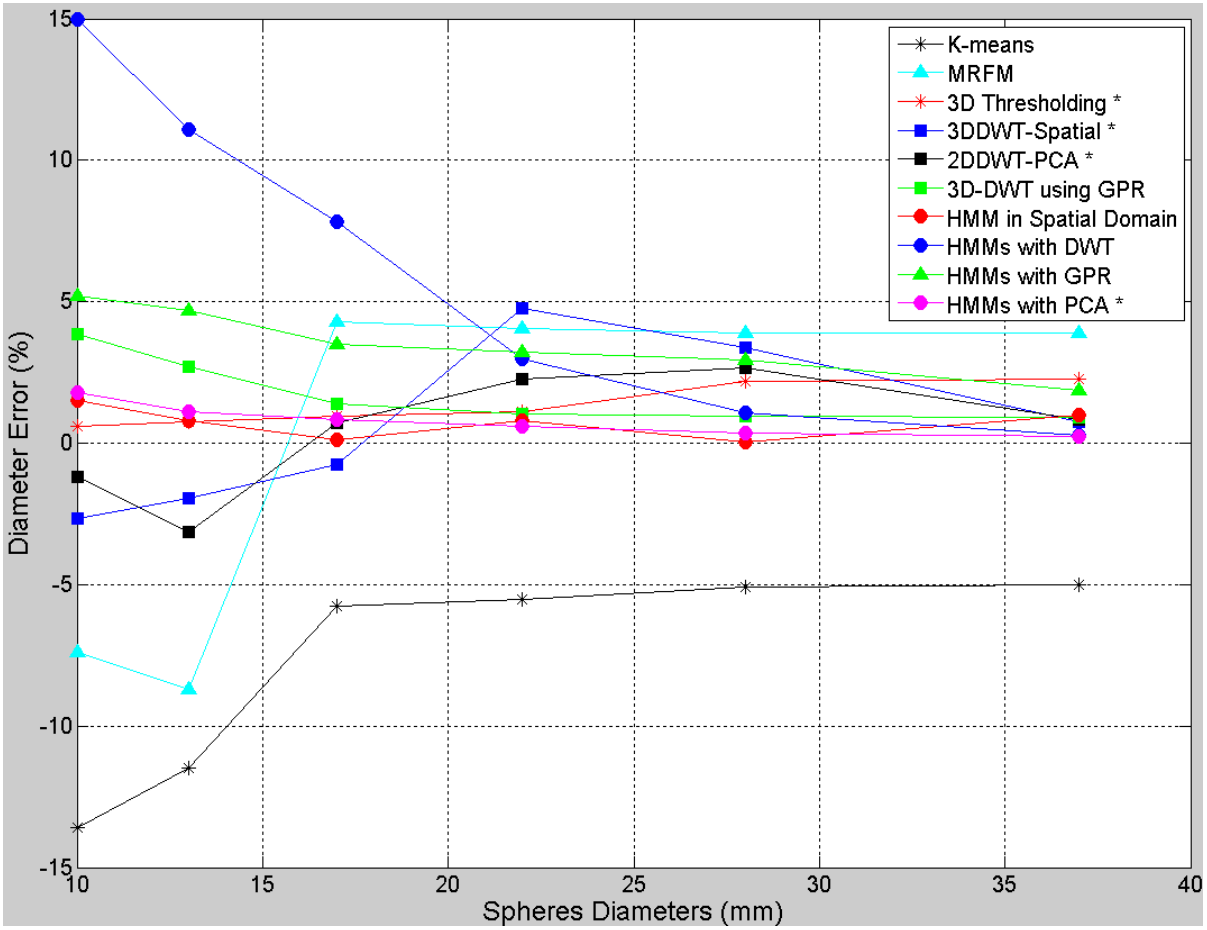

* = *using outer diameters.*

Fig. 7.16: The percentage errors, computed between the actual spheres diameters

solution for the real-time performance of the segmentation algorithms. Hardware implementations of medical image segmentation algorithms require reduced dimensional data as well as low storage requirements. PCA and GPR techniques show promising results in terms of reducing computational times for medical image segmentation. Based on this performance, these techniques are applied on medical volumes which are significantly reduced the processing time for segmenting the proposed data.

Applying 3D-DWT on the spatial domain detect the ROI in less error percentages and more computational time compared to applying it on the reduced features volumes using PCA or GPR. Error percentages in those techniques are close to the errors in spatial domain. GPR requires less computational time compared to PCA, but the problem in GPR that data loss will start appearing from the second GPR level, where PCA reduction is safe from this problem.

HMMs yield very good segmentation results and overcome many other techniques, the limitation of using HMMs in medical image segmentation system is the delay in delivering results to the next block in the system. This problem is due to the slowest step for applying HMMs for segmentation which is training the model to get the most likely states. FR techniques can be applied here to surmount this issue and accelerate this process by reducing the amount or the dimensionality of the training dataset.

Chapter 8

System Validation for Real Medical Applications

8.1. Introduction

Medical imaging is one of the fastest growing areas within medicine at present, both in the clinical setting in hospitals and in Research and Development (R&D). The importance of medical imaging for patient management is growing steadily. Medical imaging plays an increasingly important role in treatment and diagnosis. Diagnostic and therapeutic medical imaging benefits the patient through more rapid and precise disease management, fewer side effects, and improved outcome. Furthermore, medical imaging benefits the health care system through improved efficiency and more cost-effective solutions.

The end users of the proposed system are the radiologists or doctors who analyze the scanner output and give their reports based on the information from the scan. Radiologists use medical imaging technology to diagnose and treat medical conditions; they have been used for medical purposes for over a century and remain a cornerstone of the

medical field. The proposed system should achieve three overarching objectives: improved patient outcome, time-efficient health care, and commercialization of useful innovations. These objectives increase the competitiveness of health-related industries and businesses. It is intended that physicians use the information gained through the proposed system to treat and monitor injuries and diseases while cancer and other medical conditions are also treated with radiological technology through the use of concentrated radiation doses.

This chapter's goal is to validate the implemented techniques in this thesis using clinical datasets and real applications. The remainder of this chapter is as follows: the next section illustrates the effects of sensitivity factors on PET scans, this have been tested and generalized using the proposed system. The proposed segmentation techniques' quality has been validated using real clinical datasets in section 8.3. Section 8.4 includes a system validation based on a survey filled in by the end users of the proposed system. The work will be summarized in section 8.5.

8.2. PET Scanner Sensitivity Analysis

The work in this section has been done in collaboration with ***Paul Strickland Scanner Centre, Mount Vernon Hospital, London, UK***. One of the main problems in PET scanner is the reconstruction of the original radioisotope distribution within the patient, using the projections of data acquired from the scanner detectors at different angles. A statistical image reconstruction technique called Ordered Subset EM (OSEM) is used. In OSEM, a crude image estimate is initially generated and the corresponding estimated projection data is calculated, and then compare these with the real measured projection data. Then, the

image estimate is updated based on the ratio or difference between measured and estimated projections. This process is repeated for a number of iterations until satisfactory convergence of the algorithm is established. This technique is relatively fast as it splits the estimated and measured projections into subsets and updates the estimated image before the next subset commences. A full iteration has taken place if all subsets have been considered.

Some large volumetric errors encountered using the acquisition systems exists due to a wrong choose of those systems variables, such as the consequence of the poor slice thickness setting selected for the scan. The 4.25 mm slice thickness causes large fluctuations in transaxial tumour areas to occur between image slices. This problematic characteristic occurs most notably with the smallest human objects, such as the lesion in its early stages or the smallest spherical insert in NEMA IEC body phantom, where single voxel reallocation causes a large deviation in percentage error.

Collaboration with *Paul Strickland Scanner Centre in Mount Vernon Hospital* was established to come up with standards of using the PET scanner variables in the area of medical imaging. NEMA IEC body phantom was also used experimentally here, because of its similarities to the real clinical data. The phantom was scanned in different environments with different scanner variables in each time, and then the best slice evaluating the actual spheres' size will be segmented.

2D or 3D imaging is a misnomer; the acquired data is reconstructed into 3D volumes with either data acquisition mode. 2D or 3D instead refers to the use of collimators to limit the signal to detectors (2D), or with no collimators (3D), whereby all signals are acceptable.

In 2D imaging, a uniform response across the detectors to emitted radiation occurs which is to be desired, and many signals were rejected. 3D imaging mode greatly increases the sensitivity of the PET scanner (>5 times typically) compared to 2D imaging. The detector response in 3D is not uniform but more *peaked*. For adequate sampling, this requires more bed positions to be scanned for the same body sections. In 2D acquisition mode, a patient may be scanned in five or six bed positions as they pass through the PET scanner, but in 3D mode, seven or eight beds might be required.

However, the PET system must be able to cope with the additional scattered radiation that degrades image quality. In addition the scanner must be able to cope with the extra signals being emitted from the patient. So, dead time (time required to process information) must be managed properly to avoid paralysis of the system. Furthermore the increased signal received will also contribute to a form of noise called *randoms*, which is directly proportional with the square of the signal on opposing detectors.

In PET-CT scanning the collaborators routinely acquire a whole body scan with their fixed PET detectors as the patient moves through the scanner. The PET detectors correspond to a bed position of 16 cm, and a series of bed positions allow the entire body to be scanned. Each static bed position is scanned for a fixed time; their default is 4 minutes per bed position (see Fig. 8.1).

Clinically, the collaborators in Paul Strickland Scanner Centre routinely use a standard 2D imaging protocol with a 4min scan time per bed position, using OSEM reconstruction utilizing two iterations and 30 subsets. In 3D scanning, which they use in specific circumstances with no collimator, their OSEM reconstruction employs five iterations and 32 subsets as routine, with a 4min scan per bed acquisition.

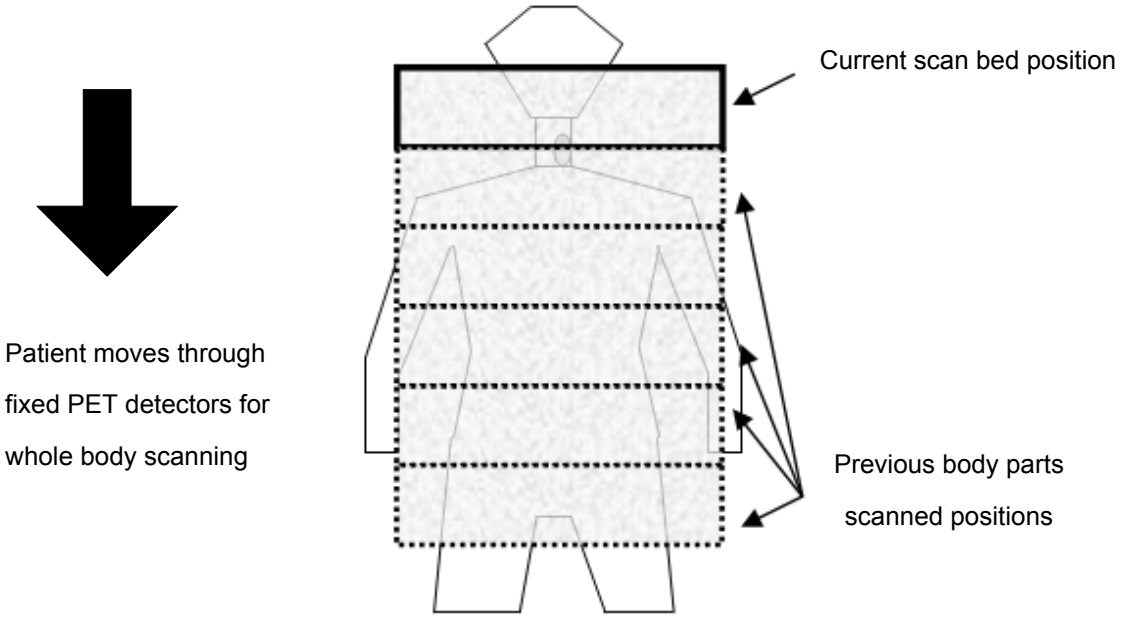

Fig. 8.1: PET scanning procedure (time per bed section).

The collaborator aims to investigate the efficiency of our proposed system for segmenting lesions of different sizes (represented by spheres in the NEMA IEC body phantom), in a clinically realistic setting of relative activity levels and lesion diameters. The influence of the sphere size is investigated in both 2D and 3D, with OSEM reconstruction of varying iterations for a fixed 4min, 3min and 2min scan time/bed. This clinically realistic study was expected to optimize the capability of developed proposed system for future clinical lesion detection with lesions of varying size and under different clinical environments.

Segmentation using curvelet transform was chosen for this experiment, and was applied in parallel with multi-thresholding and classification techniques to classify the spheres in a separate class from the other comprising objects at least noise included. The

experiment was evaluated based on the ratio between the spheres area to the other area of the scanned slice. The actual spheres area can be calculated according to equation (8.1), given that the spheres diameters are 10, 13, 17, 22, 28, 37 mm.

$$S_{Original} = \frac{1}{4}\pi \sum_{r\in\{a\}} r^2 \quad ,\{a\} = \{10,13,17,22,28,37\} \tag{8.1}$$

Where $S_{Original}$ is the actual area of all six spheres together. The scan resolution can be acquired from *Amide* software where each pixel size is *4.6875 × 4.6875* mm and each slice size is *128 × 128* pixels. The overall slice area and the ratio between both areas can be calculated according to equations (8.2) and (8.3) respectively; SBR is the spheres to background ratio.

$$A_{Original} = 128 \times 128 \times 4.6875 \times 4.6875 = 360000\ mm^2 \tag{8.2}$$

$$SBR = \frac{S_{Original}}{A_{Original} - S_{Original}} \times 100\% = 0.702\ \% \tag{8.3}$$

Table 8.1 illustrates the results for a sample data provided from the collaborator for different scanner variables. It can be seen that the SBR percentages varies based on the scanner variables used. To explain the effects of those variables on the output image, Fig. 8.2 illustrates the changes in the quality of the segmented image based on the scanners variables.

Table 8.1: Spheres to background ratio (SBR) for different variable samples

2D / 3D	Time / bed section	Iteration	SUB	SBR (%)
2D	2 min	1	30	0.46
2D	2 min	3	30	0.36
2D	2 min	5	30	0.31
2D	2 min	10	30	0.24
2D	2 min	30	30	0.22
2D	3 min	1	30	0.56
2D	3 min	5	30	0.59
2D	3 min	7	30	0.58
2D	3 min	10	30	0.55
2D	3 min	20	30	0.53
2D	4 min	3	30	0.55
2D	4 min	5	30	0.54
2D	4 min	15	30	0.42
2D	4 min	20	30	0.36
2D	4 min	30	30	0.31
3D	2 min	1	32	1.1
3D	2 min	3	32	0.76
3D	2 min	7	32	0.71
3D	2 min	10	32	0.69
3D	3 min	1	32	1.02
3D	3 min	3	32	0.77
3D	3 min	10	32	0.71
3D	3 min	15	32	0.68
3D	4 min	1	32	1
3D	4 min	3	32	0.74
3D	4 min	10	32	0.68
3D	4 min	30	32	0.64

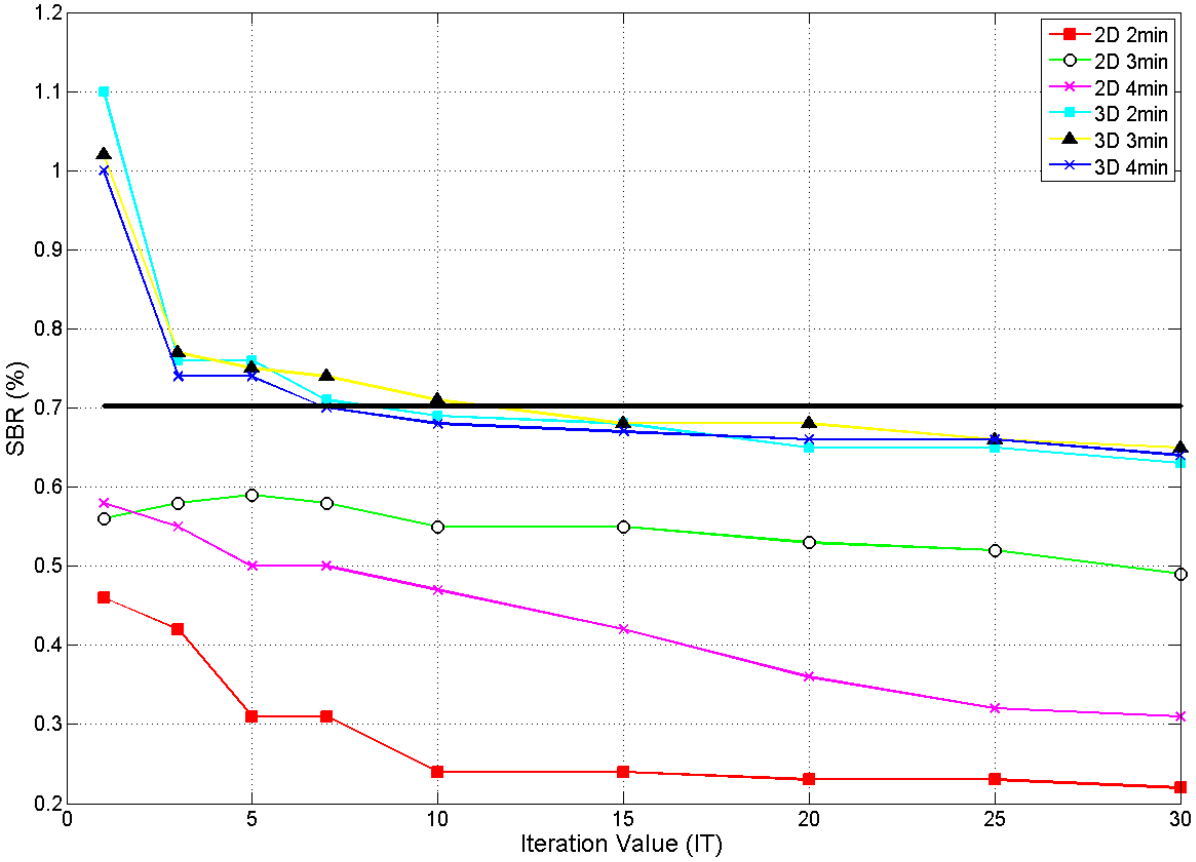

Fig. 8.2: Scanner variables effects on the segmented image

It can be seen from Fig. 8.2 that 3D scans produce closer SBR percentages than 2D for all iterations except at IT = 1. It can be noticed that the area evaluating the spheres decreases as the IT value increases for both 2D and 3D and for all bed section scanning times. These results match the expectation of the radiologists at Paul Strickland Scanner Centre. The segmented results achieved at IT =10 are illustrated in Fig. 8.3.

Other datasets with different scanning time per bed section were also tested with attenuation correction and without attenuation correction. Table 8.2 illustrates the SBR of these datasets.

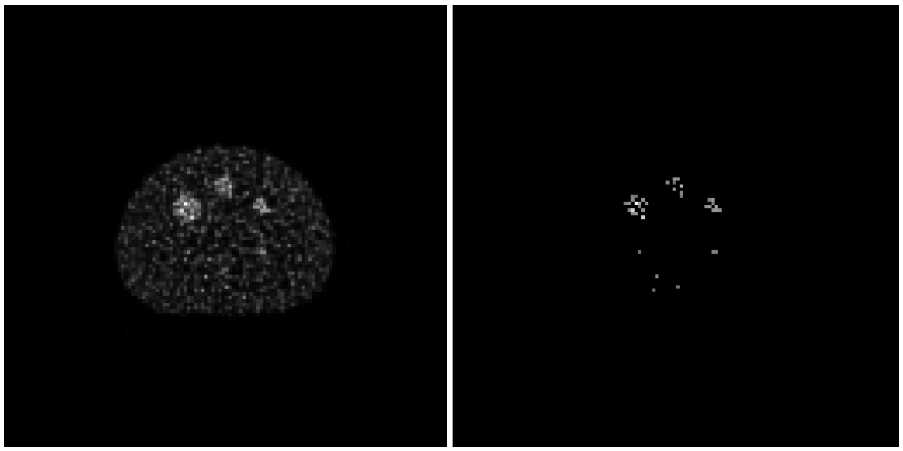

Fig. 8.3 (a) IT =10, Time = 2 min, Collimator : 2D (Left), Segmented (Right)

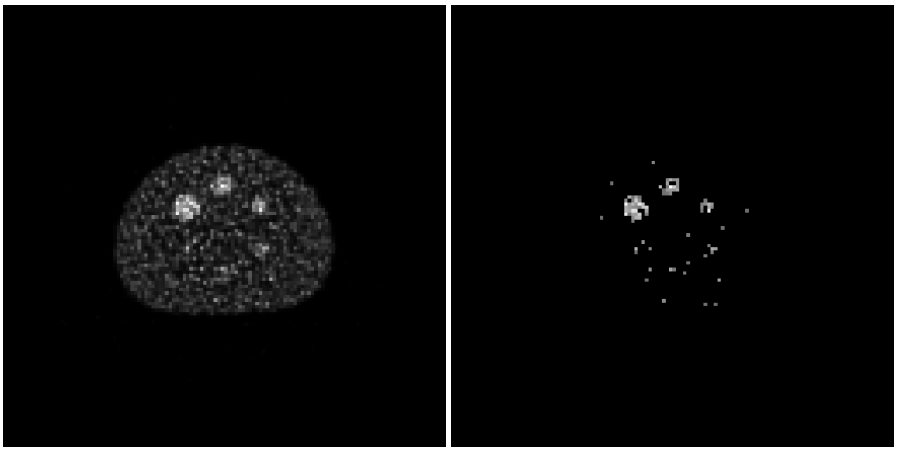

Fig. 8.3 (b) IT =10, Time = 3 min, Collimator : 2D (Left), Segmented (Right)

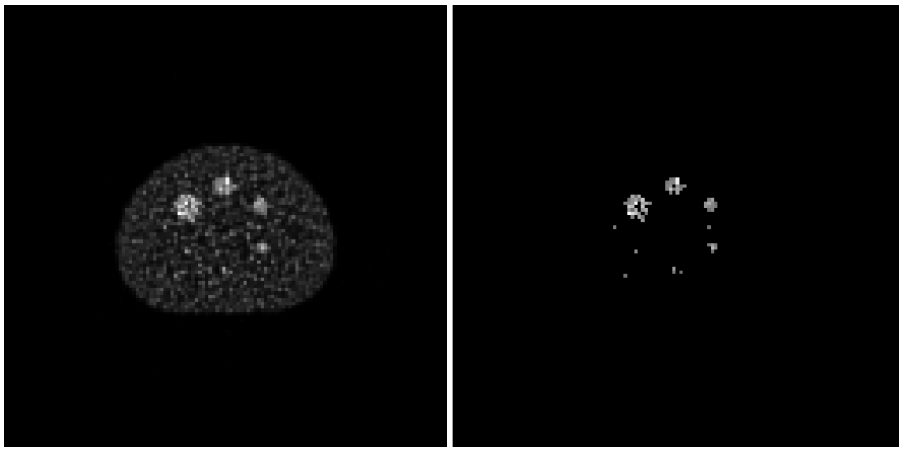

Fig. 8.3 (c) IT =10, Time = 4 min, Collimator : 2D (Left), Segmented (Right)

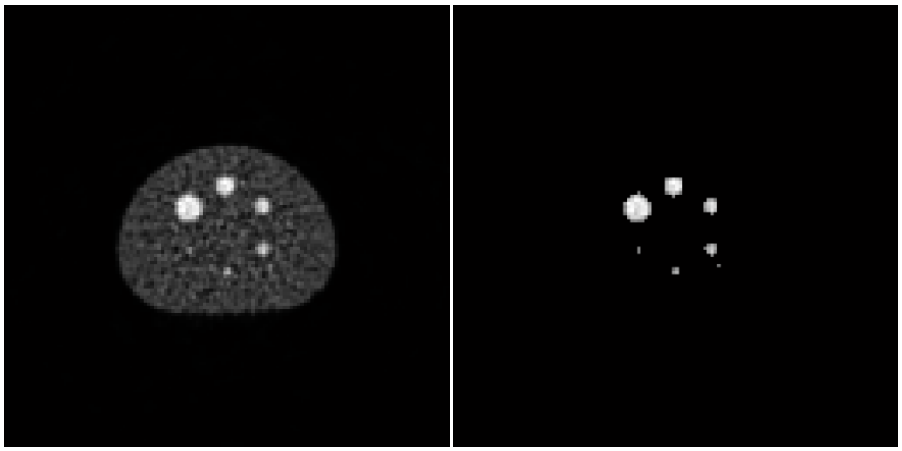

Fig. 8.3 (d) IT =10, Time = 2 min, Collimator : 3D (Left), Segmented (Right)

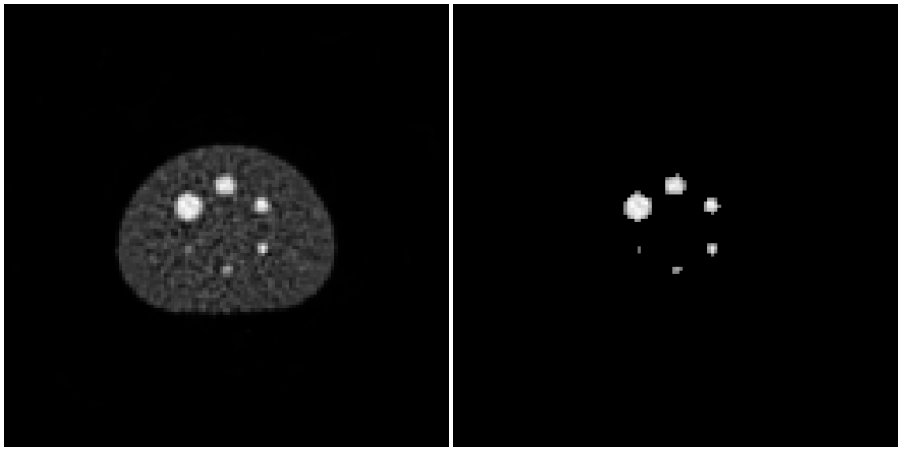

Fig. 8.3 (e) IT =10, Time = 3 min, Collimator : 3D (Left), Segmented (Right)

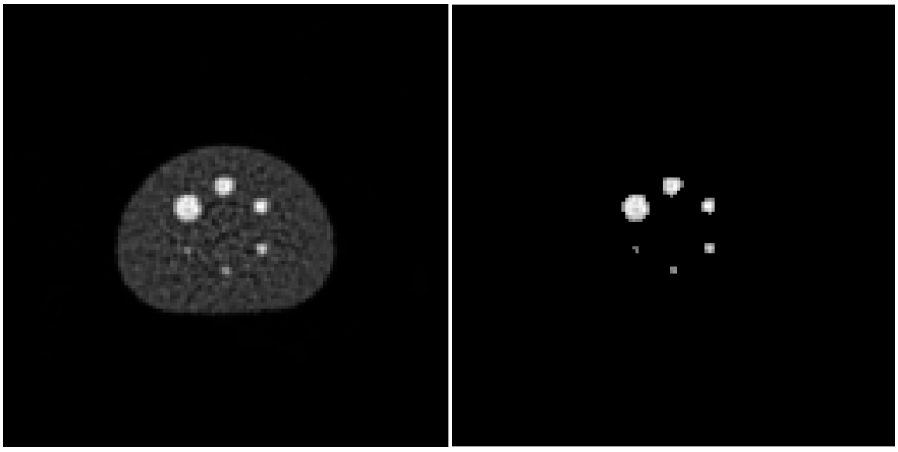

Fig. 8.3 (f) IT =10, Time = 4 min, Collimator : 3D (Left), Segmented (Right)

Fig. 8.3: Segmented results achieved at IT value (10), where the best results detected

Table 8.2: Spheres to background ratio for different time per bed section and attenuation correction

2D / 3D	Attenuation correction	Time / bed section	SBR (%)	Error (%)
2D	Yes	2 min	0.46	-34.0
2D	Yes	3 min	0.58	-16.77
2D	Yes	4 min	0.56	-19.66
2D	Yes	10 min	0.62	-11.05
3D	Yes	2 min	0.72	3.30
3D	Yes	3 min	0.75	7.6
3D	Yes	4 min	0.73	4.73
3D	Yes	10 min	0.7	0.43
2D	No	4 min	2.93	320.37

From Table 8.2, it can be seen that 3D is still much better than the 2D, and the quality is increased by increasing the time spent on each bed section in the scanning process. A big jump in the SBR can be noticed from the scanned dataset without attenuation correction. This is expected as the scanned output is blurred and very hard to analyze.

8.3. Real Clinical Data Validation

In this section, three different real clinical dataset for human diagnosis by cancer have been tested. The data include liver cancer, kidney cancer, and lung cancer respectively. These data have been acquired from a CT scanner in ***Diagnostic Radiology and Nuclear Medicine Department, King Abdullah University Hospital, Ramtha, Jordan***. The data was pre-analyzed as usual, and the report was provided to evaluate the performance of the proposed system.

8.3.1. Liver Cancer

The dataset evaluates the abdominal of a female diagnosed with a cancer located in the liver. Fig. 8.4 shows the comprising slices for the patient's; it is predefined that the cancer can be seen in slices 18 - 37, but it is most clearly visible in slice number 22. This slice will be passed through the proposed segmentation system to facilitate the radiologists' analysis process. Slice number 22 is illustrated in Fig. 8.5, in which the cancer has been highlighted in red based on the provided report referring to the cancer exact location inside the liver.

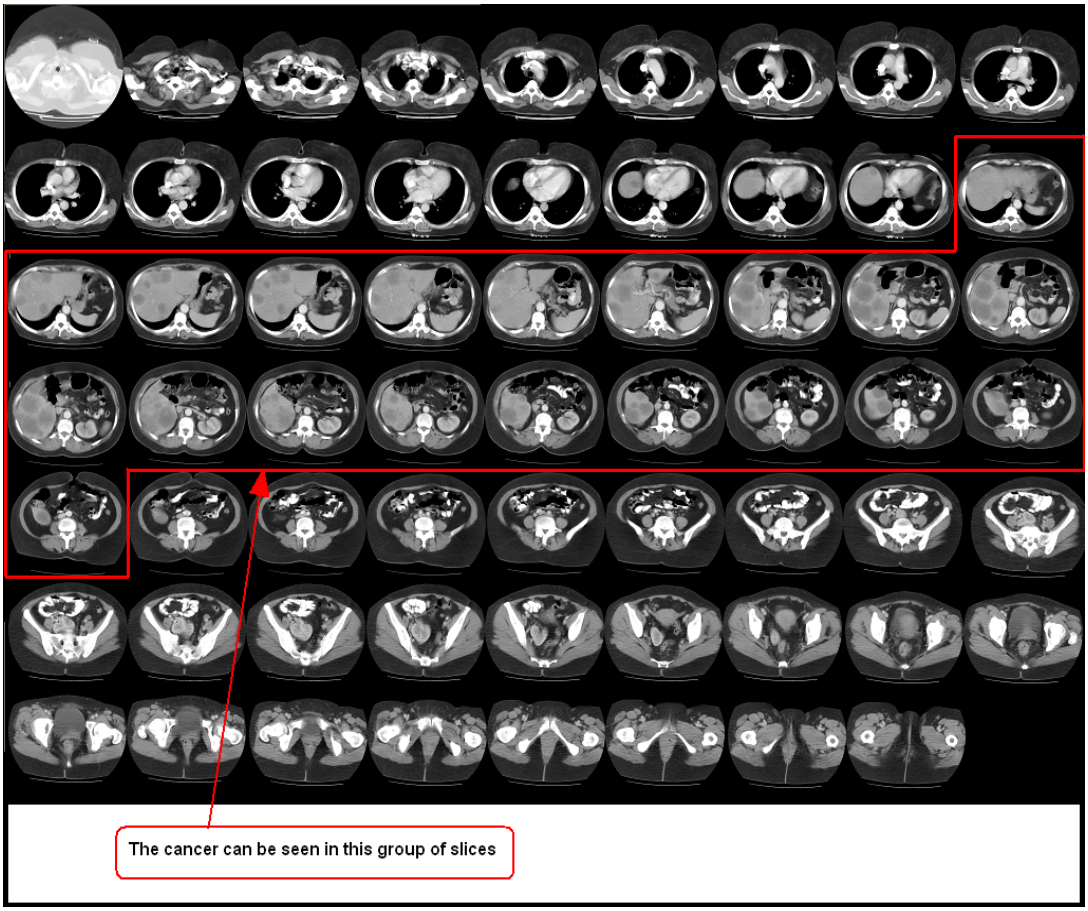

Fig. 8.4: CT scan for female abdomen diagnosed with a liver cancer

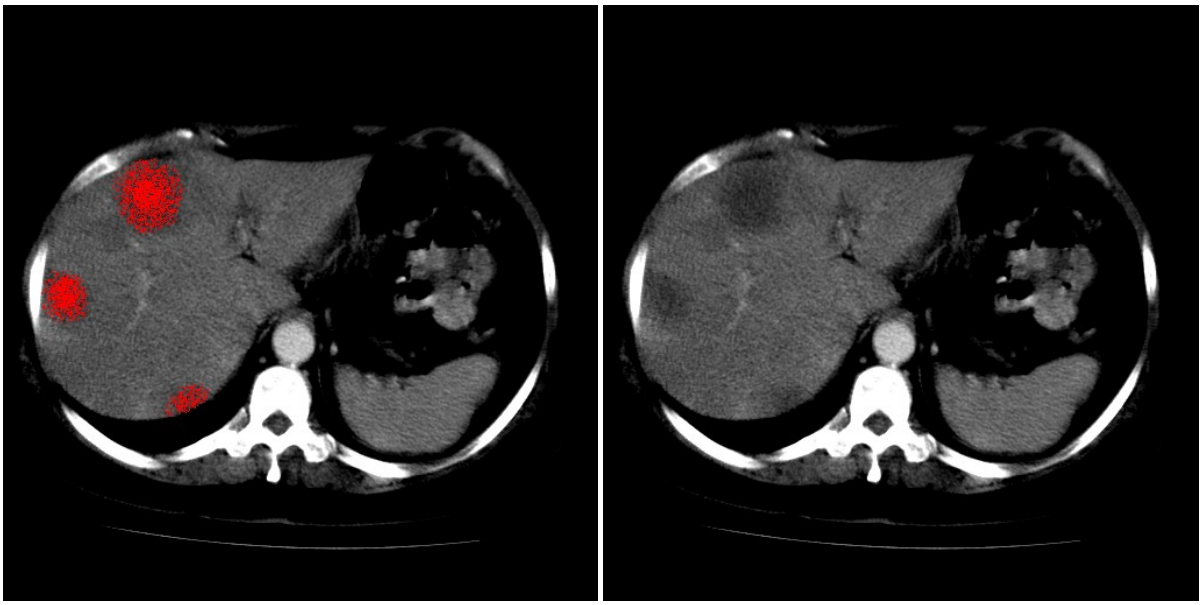

Fig. 8.5: The original medical image without any transformation, with a predefined cancer location

The purpose of medical image segmentation comes through analysis of those images directly without any transformation. Multiple factors make the process of medical image segmentation difficult, including the complexity of human anatomy, the irregular nature of tissues and organs, as well as individual variations. Regional gray inconsistency, artifacts, weak borders and border breaks, which often happen in scanners' output images, could not be analyzed based on the traditional method. As a result, medical image segmentation techniques should be implemented.

The proposed segmentation techniques have been applied on slice number 22 (illustrated in Fig. 8.5), and Fig. 8.6 illustrate the segmented outputs after applying the implemented segmentation techniques on this slice.

(a) Thresholding at t = 77

(b) Inverse Thresholding at t = 50

(c) Clustering (6 classes)

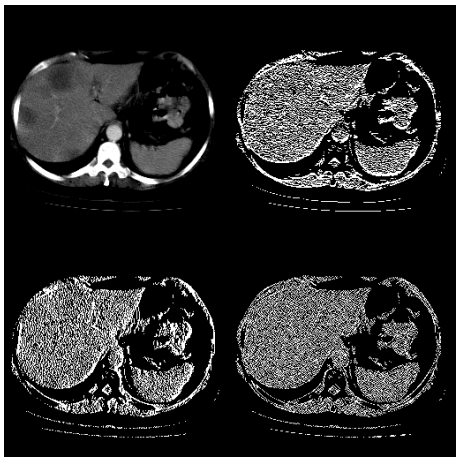

(d) Wavelet Transform

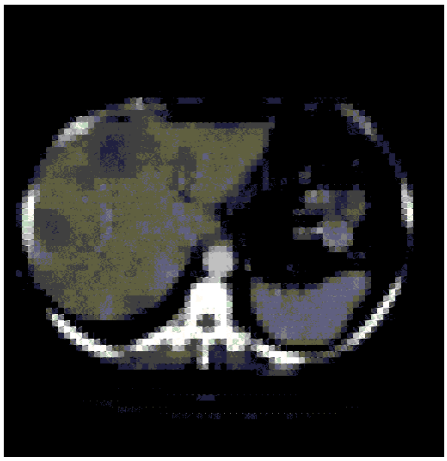

(e) RADON Transform

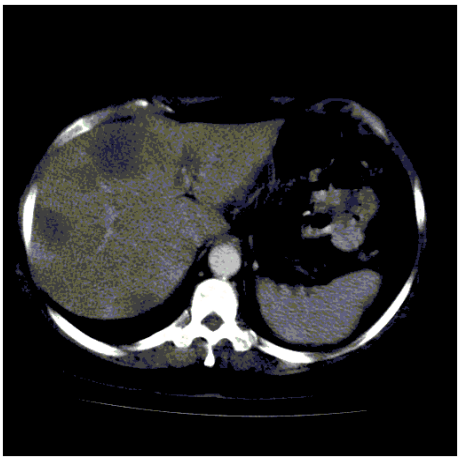

(f) Ridgelet Transform

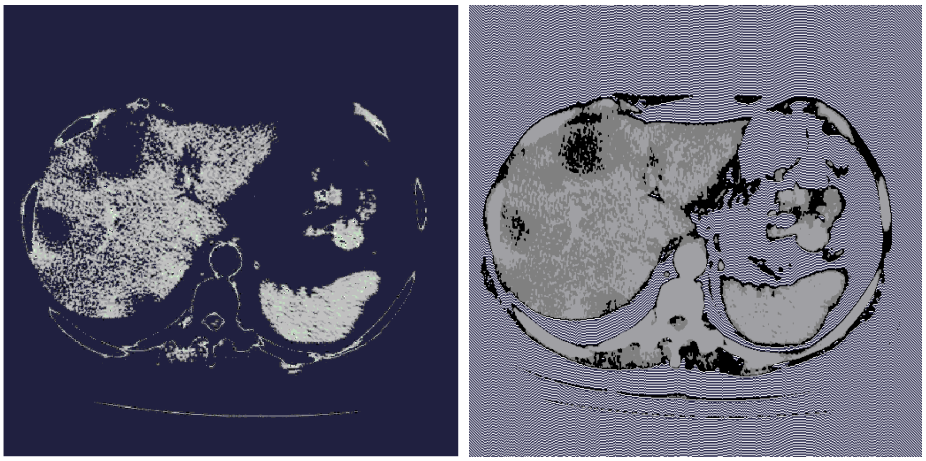

(g) Curvelet Transform (h) HMMs

Fig. 8.6: Segmented liver cancer using the implemented segmentation techniques

It can be seen from the segmented images in Fig. 8.6 that ROI has been detected using most of the segmentation techniques, but with varying quality. Both thresholding-based techniques in Fig. 8.6 (a) and (b) have detected the predefined liver cancer, but the problem with those methods is the data contouring loss, whereby much image information has been missed in the transformed domain. Therefore, thresholding-based techniques are of limited use in medical image segmentation, and are best used as pre-processing or post-processing steps along with other techniques. Clustering technique (used in Fig. 8.6 (c)) provided more accurate results compared to the thresholding techniques. The problem with using clustering in medical image segmentation lies in manual thresholding; multi-thresholding values have been set manually based on the human vision.

MRA has been used with this slice, and the outputs of applying wavelet, FRAT, ridgelet and curvelet transforms have been illustrated in Fig. 8.6 (d) to (g) respectively. Curvelet transform overcomes the other MRA transforms for this dataset, but this cannot be

generalized, as each MRA technique performs better than the others with specific data types. HMMs overcome all the other available techniques in segmenting the illustrated medical slice (Fig. 8.6 (h)). ROI has been detected accurately and the other image contouring has not been affected.

8.3.2. Kidney Cancer

The second proposed dataset comprised of 217 slices, with slice thickness of 3.0 mm. based on the provided report, the patient is affected by multiple bilateral renal cortical cysts; the largest one is seen in the lower pole of the right kidney, measuring about 47 x 45 mm. A snapshot taken for the AMIDE window and the ROI has been located by the red lines in three different orientations of the patient's body scan (Fig. 8.7). It can be seen that ROI appears more clearly in its biggest illustration in slice 198, this slice is illustrated in Fig. 8.8, and the ROI (kidney cancer) has been highlighted by red colour.

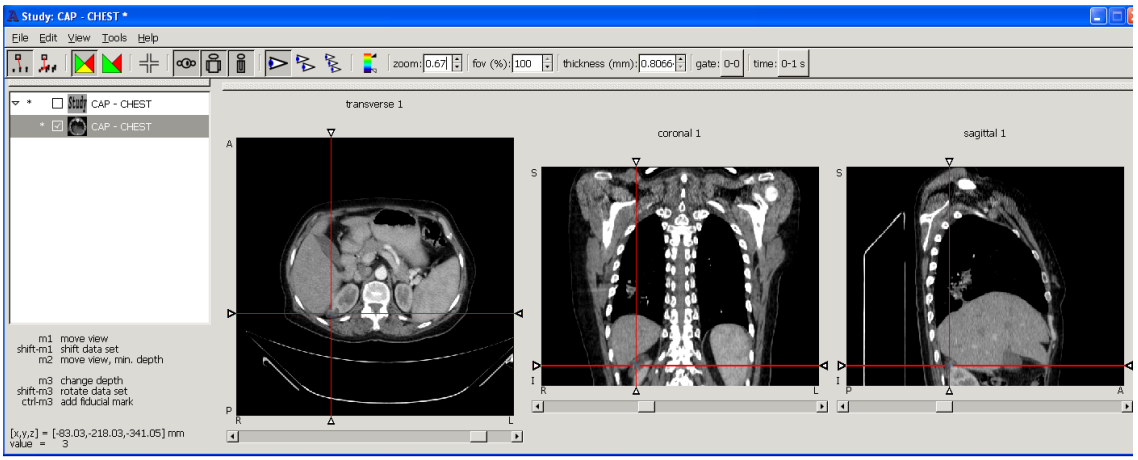

Fig. 8.7: AMIDE snapshot locating the kidney cancer

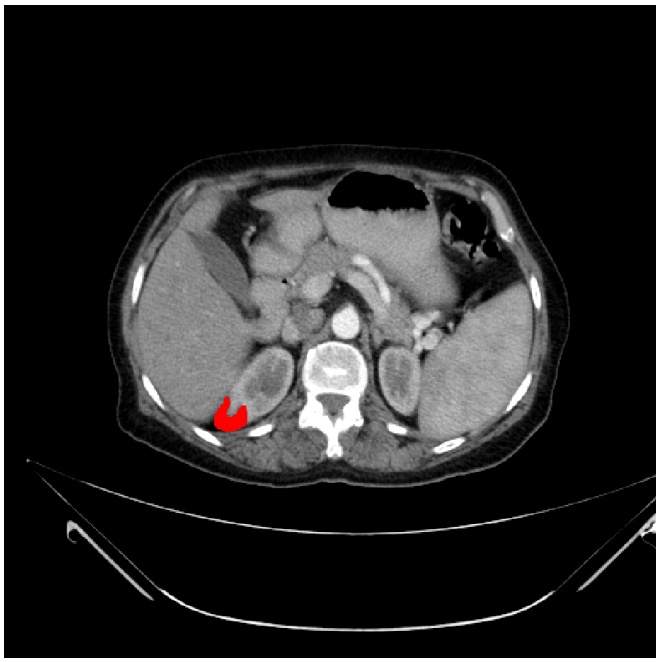

Fig. 8.8: ROI highlighted in the original image (Kidney cancer)

Different segmentation techniques have been applied on the medical image to segment it and detect ROI. Fig. 8.9 illustrates the outputs of applying those techniques on the CT slice that affected by kidney cancer:

Fig. 8.9: Segmenting medical CT slice diagnosis by kidney cancer using different segmentation techniques

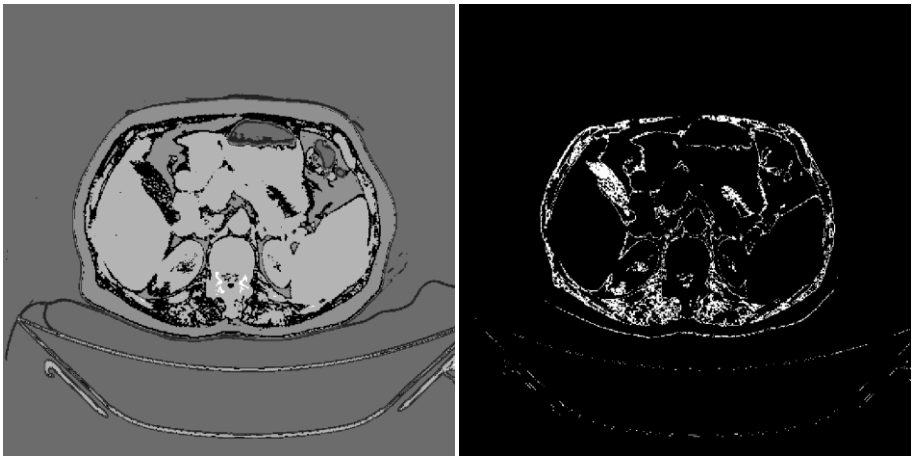

(a) Clustering

(b) Multi-Thresholding at t1=1015 and t2=1045

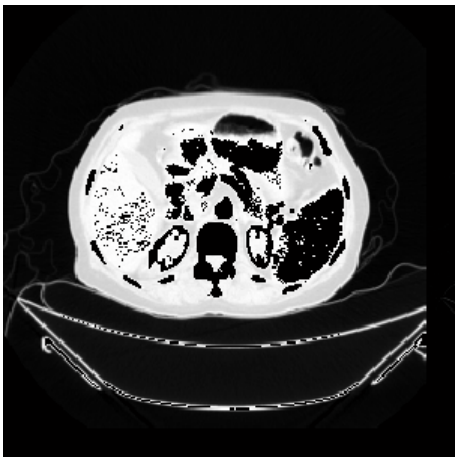

(c) First decomposition Level of Wavelet transform (DWT) and Daubechies filter (db2) with inverse thresholding at t= 2200

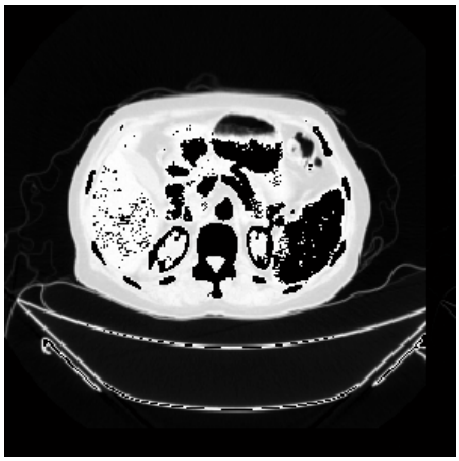

(d) First decomposition Level of Wavelet transform (DWT) and Haar filter with inverse thresholding at t= 2200

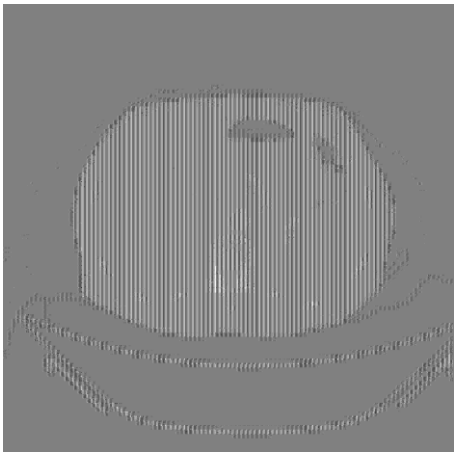

(e) Ridgelet Transform

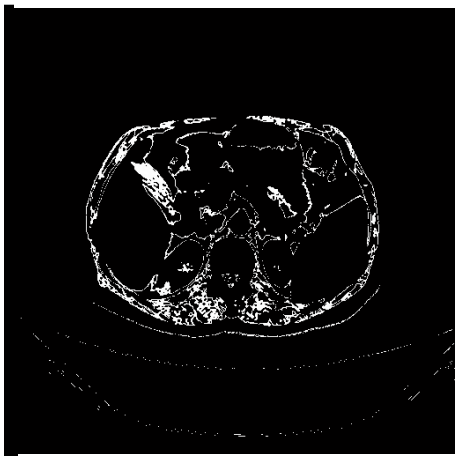

(f) Curvelet Transform

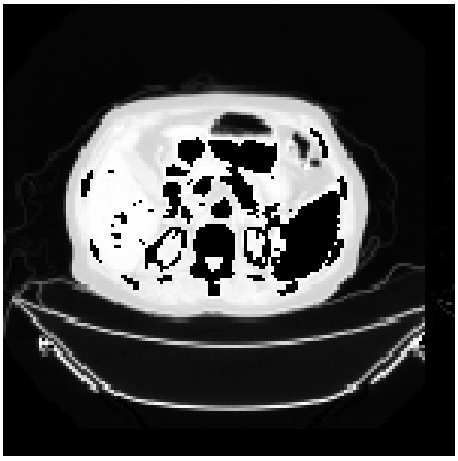

(g) Second decomposition Level of Wavelet Packet with inverse thresholding at t=4400

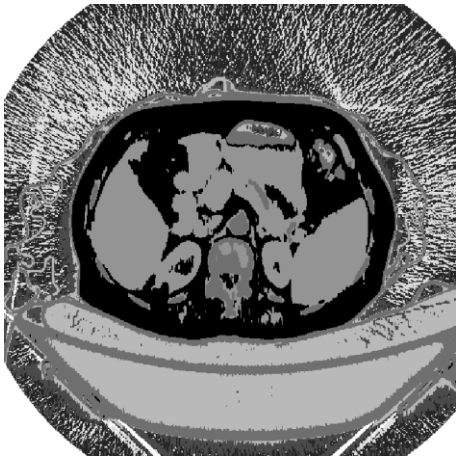

(h) Segmentation using HMMs with 8 classes

It can be seen in the previous images that some techniques segment the ROI properly (Fig. 8.9 – (a)(c)(d)(f)(h)) and some do not such as ridgelets; additionally, some of them merge some obstacles together and make the analyzing process more difficult. Each technique has its advantages and disadvantages, and it may segment a part of the medical image accurately and the other parts badly. Therefore, the proposed segmentation system intends to use all of those techniques to produce the most accurate results with least loss.

The performance of the proposed techniques for segmenting the illustrated slice in Fig. 8.9 is explained in Table 8.3. The area of the cancer has been measured and compared to the provided report, and then used to qualify the performance of each technique as well as MSE, Data Loss and PSNR. Data loss has been classified here bas on our experience.

Table 8.3: Segmentation techniques' performance based on patient data (kidney cancer data)

Segmentation Technique		Cancer Area Accuracy (%)	MSE	PSNR (dB)	Data Loss
Classification		93.9	56.0	38.5	Low
Multi-Thresholding		95.1	97.7	27.8	High
DWT	**Haar**	91.0	102.7	35.2	Normal
	Daubechies	89.5	104.5	34.3	Normal
Wavelet Packet		83.2	111.2	30.9	Normal
Ridgelet		---	109.9	30.3	High
Curvelet		96.2	88.2	29.5	Normal
HMMs		97.3	43.1	41.2	Low

8.3.3. Lung Cancer

Based on the provided report with this dataset, it consists of 221 slices, with slice thickness of 3.0 mm. A well-defined lobulated soft tissue mass lesion can be seen in the lateral segment of the right lower lung lobe, containing foci of calcification measuring about 38 x 20 mm. A snapshot taken for the AMIDE window (Fig. 8.10) and the ROI is located by the red lines in three different axes of the patient's body scan. The cancer can be located easily in each axial view, but defining the exact edges of the cancer is problematic. Slice number 140 has been predefined as the slice containing the best view of the cancer in the transverse patient scan view. The predefined cancer has been highlighted in the three axial views (transverse, coronal, sagittal), as illustrated in Fig. 8.11.

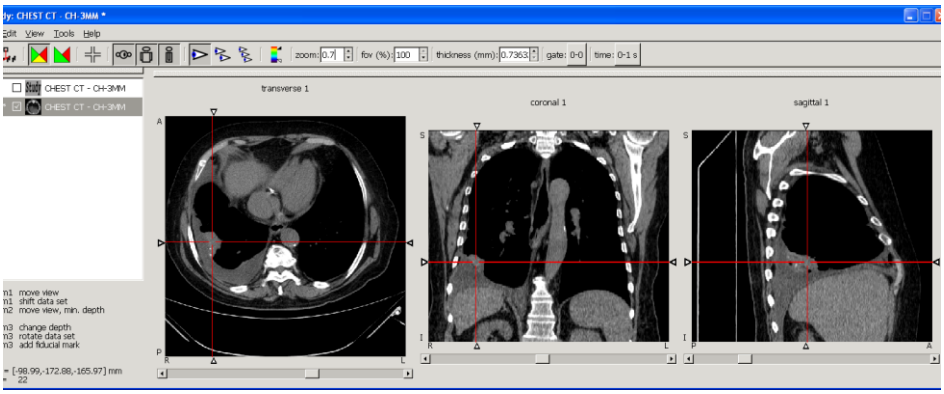

Fig. 8.10: AMIDE snapshot locating the lung cancer

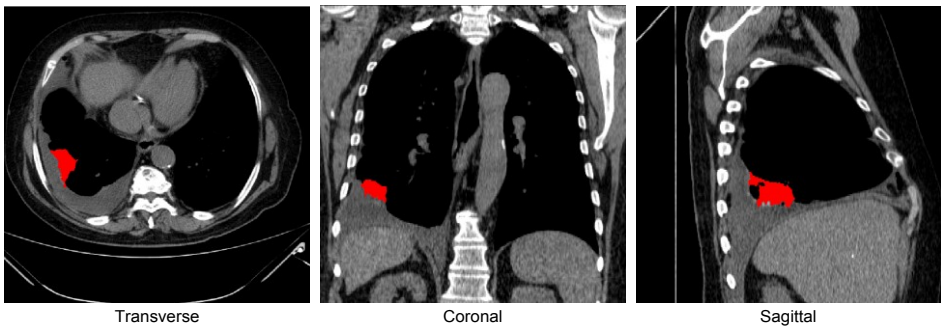

Transverse Coronal Sagittal

Fig. 8.11: ROI highlighjted in the original image

The lesion highlighted in Fig. 8.11 is located near the lung edge, which make the process of quantifying this lesion harder than other locations in the lung. It is hard here to differentiate between the pixels comprising the cancer and the calcareous pixels. Therefore, segmentation techniques can be applied to facilitate the process of analyzing and quantifying the proposed lesion. Fig. 8.12 illustrates segmented transverse axial using different segmentation techniques.

(a) Clustering

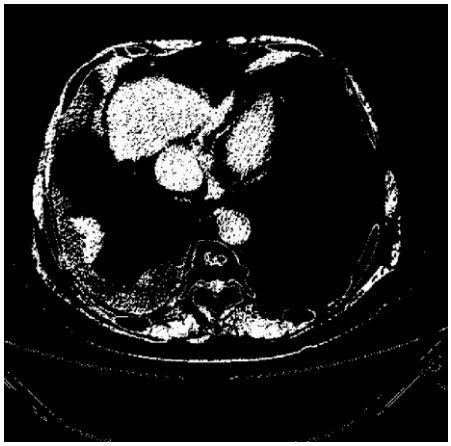

(b) Multi-Thresholding at t1=1035 and t2=1080

(c) First decomposition Level of Wavelet transform (DWT) and Daubechies filter (db2) with inverse thresholding at t= 1500

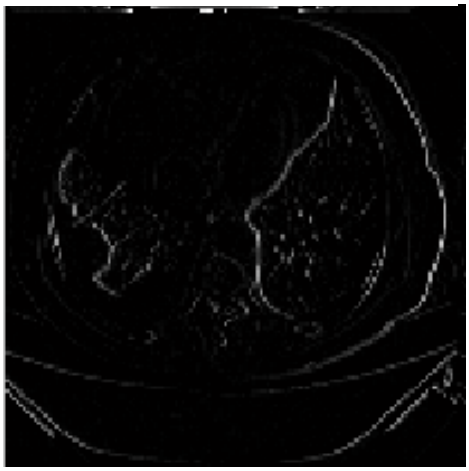

(d) Second decomposition Level of Wavelet Packet with inverse thresholding at t=4400 (High-pass filter output - **LLHL**)

(e) Ridgelet Transform

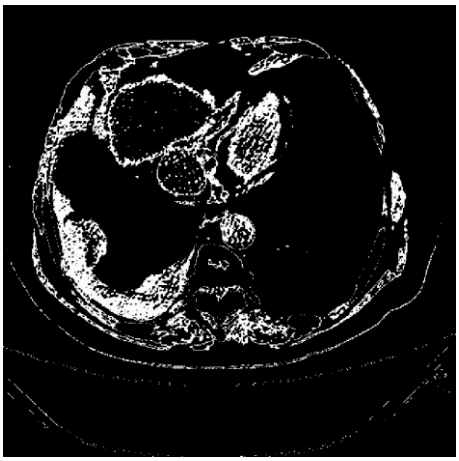

(f) Curvelet Transform

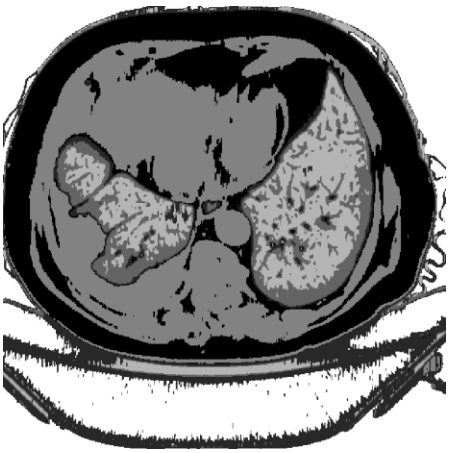

(g) Segmentation using HMMs with 4 classes

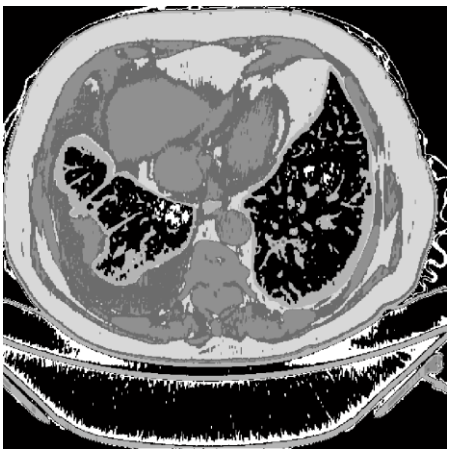

(h) Segmentation using HMMs with 8 classes

Fig. 8.12: Detecting Lung cancer using different segmentation techniques

It can be seen in Fig. 8.12 that all of the proposed segmentation techniques detect the ROI (lung lesion), but in varying degrees of quality. Except ridgelet transform which proved its failure in medical image segmentation techniques, the reason was provided in chapter 4 in this thesis. Some of the techniques detect ROI properly, such as multi-thresholding and HMMs with eight classes, but data loss occurs with segmenting the proposed data with multi-thresholding. The other techniques segment the ROI and merge the detected object

with other objects, such as the lung edge in segmentation using HMMs with four classes. The overall quality and performance of each technique for segmenting the proposed data set and detecting the predefined lesion are illustrated in Table 8.4.

Table 8.4: Segmentation techniques' performance based on patient data (Lung cancer data)

Segmentation Technique	Cancer Area Accuracy (%)	MSE	PSNR (dB)	Data Loss
Classification	68.4	62.3	33.3	Low
Multi-Thresholding	97.2	92.5	25.6	High
DWT with Daubechies filter	78.9	106.6	27.4	High
Wavelet Packet	88.0	109.0	30.3	High
Ridgelet	---	103.2	28.8	High
Curvelet	92.1	89.2	24.9	Normal
HMMs (No. of classes = 4)	96.5	45.6	40.1	Low
HMMs (No. of classes = 8)	98.8	39.1	44.5	Low

It can be noticed from the experimental results from the real clinical datasets that some segmentation techniques' segmented output with a particular dataset was convincing, but at the same time, this technique failed with other dataset. For example, clustering segments the dataset with kidney cancer properly and causes a data loss in segmenting the dataset with lung cancer, and merges the lesion pixels with other objects' pixels. Therefore, the proposed system used to test all available techniques with each single dataset, and takes the decision based on the best segmented results.

The clinical datasets have been segmented also using 3D segmentation techniques, and the lesions were detected accurately. The available patient data which includes lesions in liver, kidney and lung has been segmented using the proposed 3D techniques, the achieved results are visualized in Fig. 8.13, Fig. 8.14 and Fig. 8.15 where the OOIs are located.

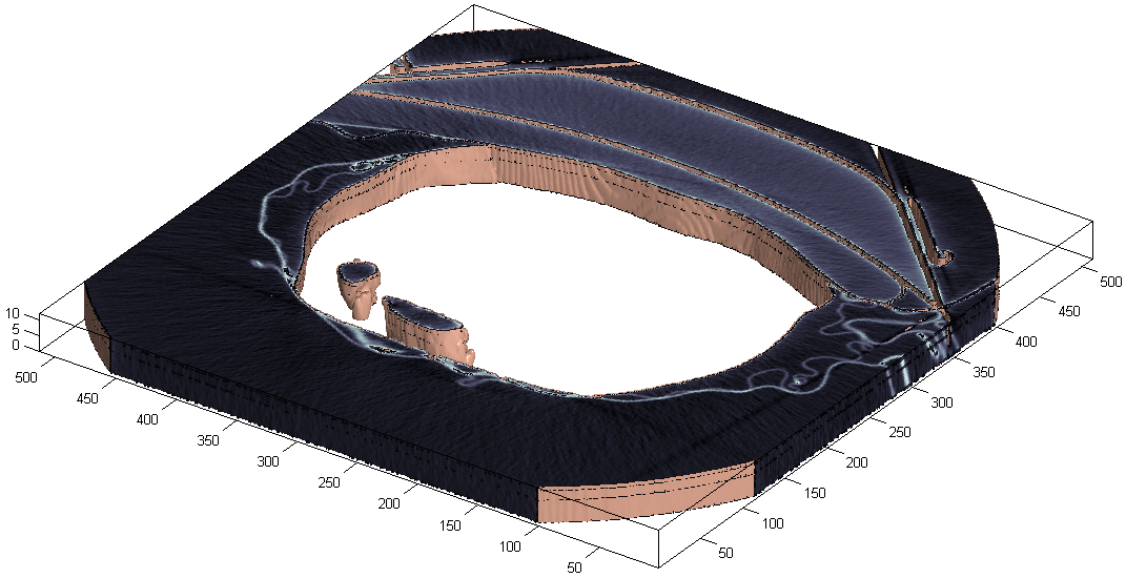

Fig. 8.13 (a): The first segment (Background)

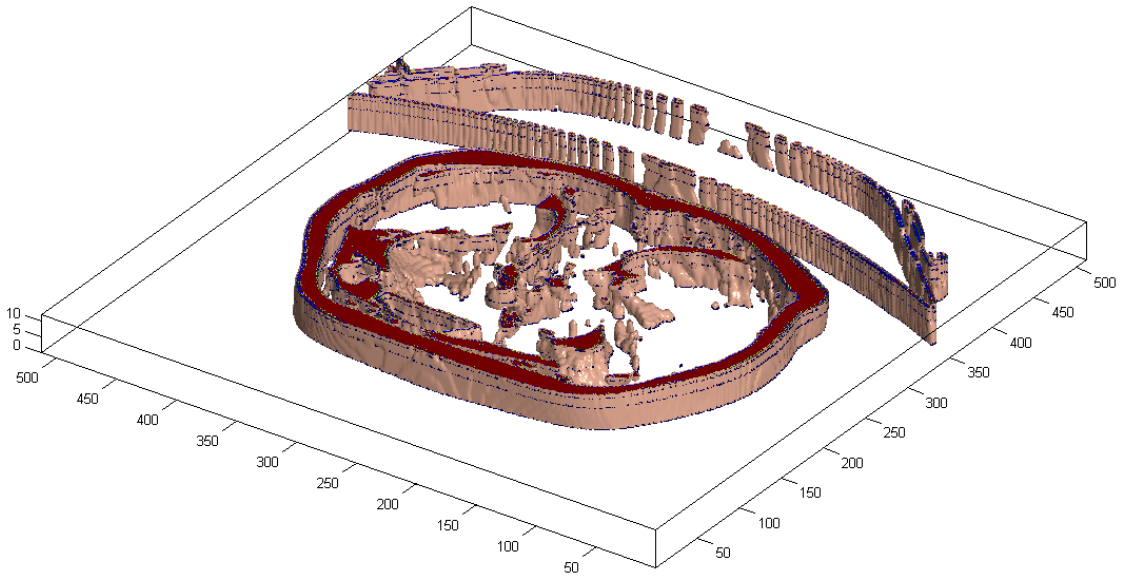

Fig. 8.13 (b): The second segment (Obstacle edges)

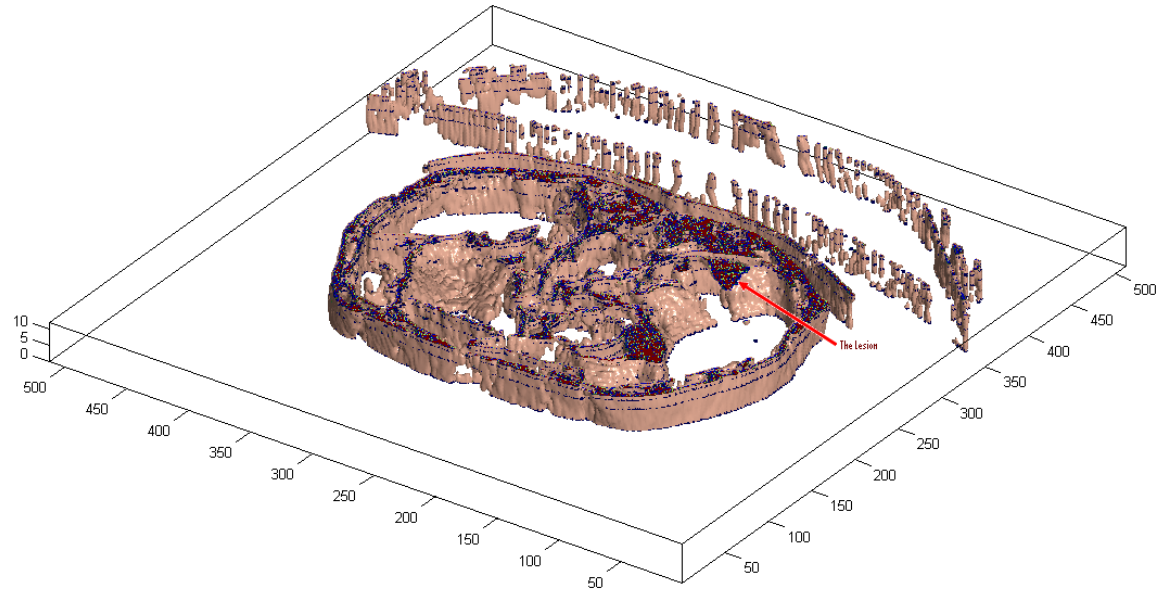

Fig. 8.13 (c): The third segment (includes ROI)

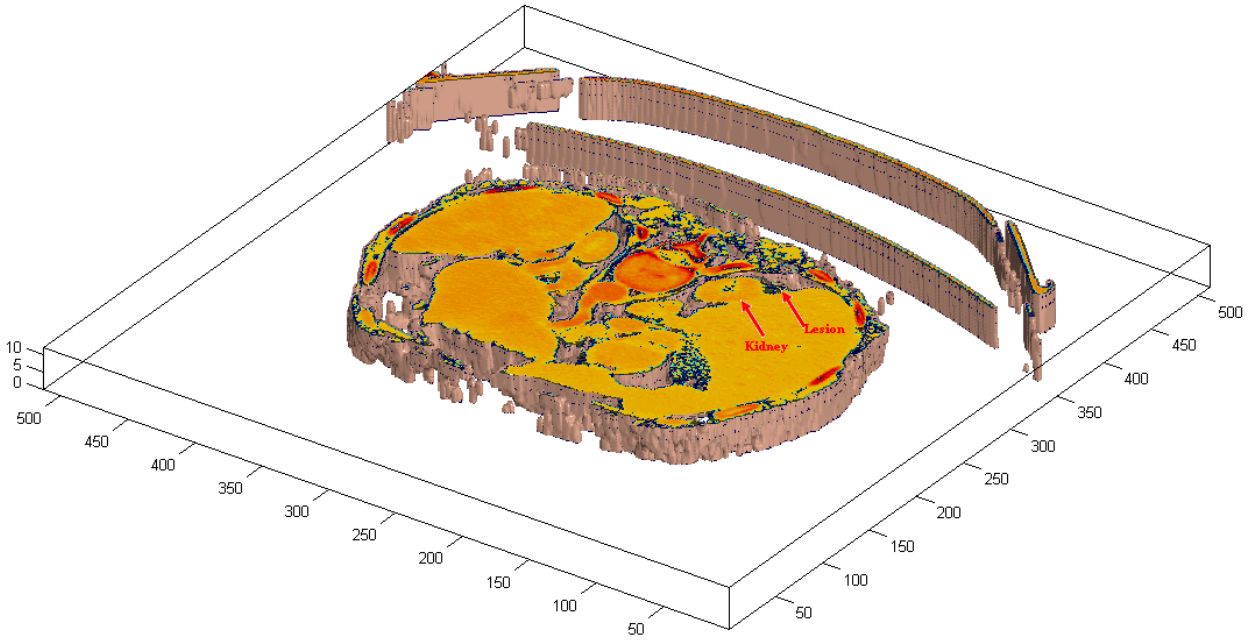

Fig. 8.13 (d): The fourth segment (obstacle surfaces)

Fig. 8.13: Segmenting patient volume data affected by the kidney cancer

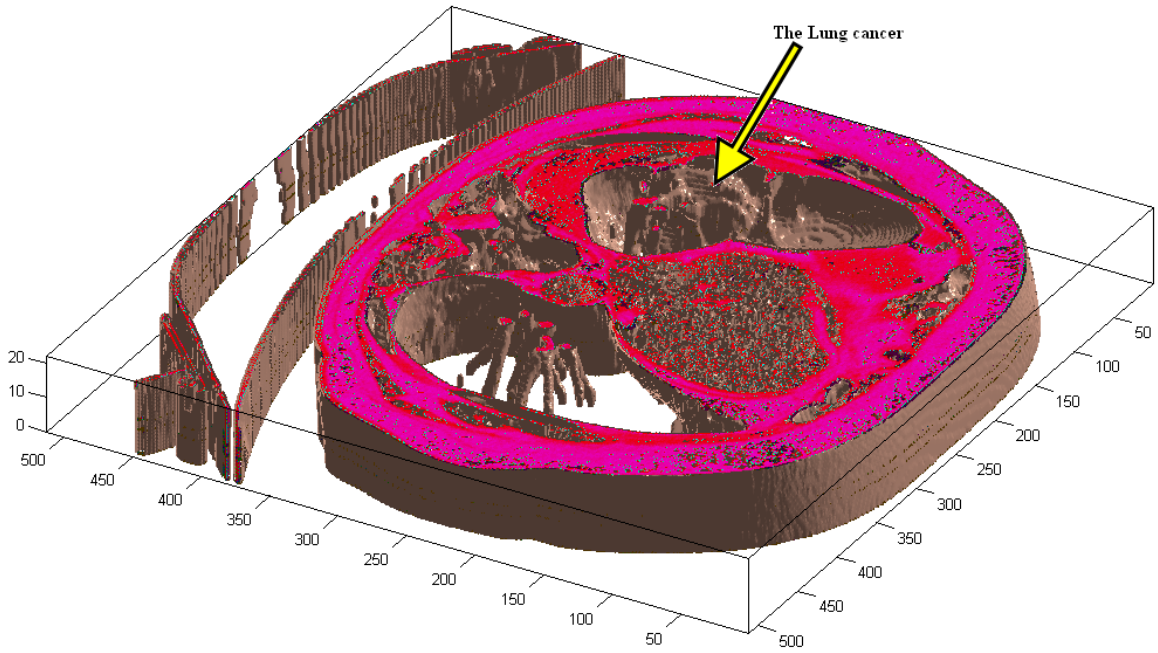

Fig. 8.14: Segmenting patient volume data affected by the Lung cancer

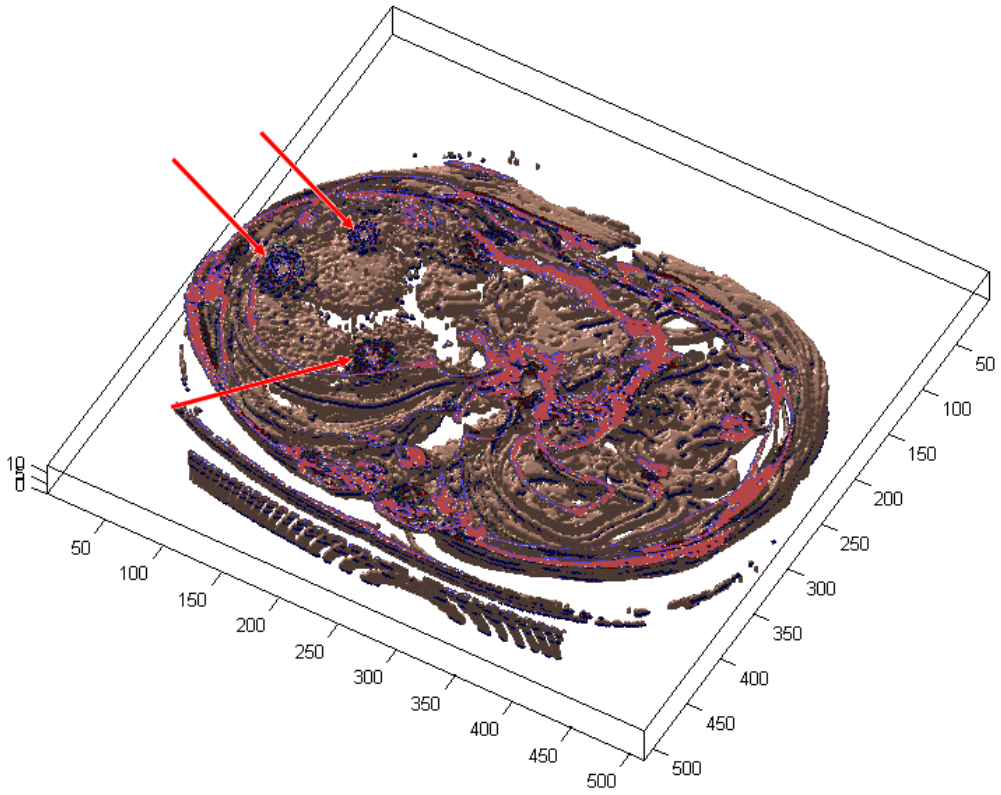

Fig. 8.15: Segmenting patient volume data affected by the Liver cancer (Located by red arrows)

8.4. End Users Validation

It has been mentioned before that the end users of the proposed system are the radiologists and doctors, who analyze the scanner output for cancer diagnosis and radiotherapy planning. The end users must be happy with the system to validate it and make it applicable for real clinical applications.

The proposed system was devised to cover the end users' requirements in the process of analyzing medical images, and avoid any weakness based on their point of view. Therefore, a survey explaining the implemented techniques and the expected segmented output of these techniques was prepared and filled in by the end user specialists. This survey focused mainly on arranging the implemented techniques into five different classes based on different comparison factors, as well as comparing the output results with other results acquired from previously available segmentation techniques for the same experimental dataset. This survey is attached in appendix A.

It is worth mentioning that the number of the filled surveys was just 13, which is very small compared to other general surveys, this is due to the nature of the sample (i.e. highly specialized professionals). After several meetings with those specialists in the UK and Jordan, the conclusion of their point of view met our expectations. Table 8.5 concludes the end users' opinions regarding the proposed medical image segmentation techniques.

Table 8.5 employs the scale of one to five used to rate the results of using the technique (1 indicating very bad results, and 5 indicating extremely excellent results). The original input slice is included in the comparison to make it fair, as some of the end users still preferred to analyze the original scanner output without any transformations.

1 → Extremely bad

2 → Bad

3 → Acceptable

4 → Good

5 → Excellent

Table 8.5: Proposed techniques quality based on the survey of end users'

Questions	Segmentation Techniques									
	1- Original	2- Thresholding	3- Inverse Thresholding	4- Clustering	5- Edge function	6- Wavelet	7- Ridgelet	8- Radon	9- Curvelet	10- HMMs
How easy the classification	2.1	2.7	3.0	3.9	2.3	3.3	3.2	2.1	3.7	5.0
ROI illustration	2.3	3.8	3.6	4.1	2.7	2.8	2.7	2.3	4.2	4.8
Noise effects	2.5	3.1	4.3	3.4	3.2	1.3	2.8	1.8	3.6	3.7
Data loss	5.0	2.1	2.2	3.7	1.2	3.6	4.0	3.2	3.8	4.5
Ease of output analysis	2.1	3.9	3.9	4.0	2.7	2.6	2.7	1.8	4.1	4.1
Benefits for cancer diagnosis?	2.8	4.2	4.4	4.1	1.3	2.9	2.4	2.8	4.5	4.3
Better known and commonly used	1.5	4.6	3.8	3.9	2.1	4.8	1.2	1.6	2.2	2.1
Overall segmentation	2.4	3.5	3.2	4.2	1.3	3.1	2.1	3.4	4.9	4.8

It can be seen from Table 8.5 that clustering, curvelet and HMMs surpass the other techniques in most of the quality factors. The other techniques perform well in some comparison factors. Therefore, some of the end users advised the use of all of the implemented techniques, to form an accurate and solid segmentation system. The majority of the end users rated HMMs the best for medical image segmentation technique, and advised to accelerate this method.

The rest of the survey (Appendix A) includes assay questions regarding to the system techniques and the choice of using 3D volume or a stack of 2D slices for medical volume illustration. The end users' samples varied in their choice between the 3D volume illustration and the stack of 2D slices illustration. Some of them preferred to analyze a stack of 2D slices, as they are familiar with this, and learning the 3D method would be troublesome. Some other chose the 2D method for reasons related to hidden information; they mentioned that ROI may be encapsulated inside other objects in the body, and 3D choice obscures this from the end users' vision.

End users who prefer 3D volume illustration cited the benefits of the proposed segmentation system, which can be used to decapsulate ROI or remove the surrounding familiar body objects. They prefer 3D volume illustration because of its ease of use, and its ability to visualize ROI which is extending through many slices (occupying a very small area in each slice); they observed that a stack of 2D slices cannot detect such objects.

In conclusion, end users who refuse the proposed system do so due to the background of their knowledge; they have been taught to use a stack of 2D slices without any transformation for medical image analysis. They are not familiar with any transformed image except the original scanner output.

8.5. Summary

The system has its advantages and disadvantages. Validation procedures are required to generalize the system into real clinical applications. Most of the implemented techniques have been used before in other applications, and these techniques fail in some applications and succeed in others. This chapter has endeavored to activate the proposed techniques in the field of medical imaging for cancer diagnosis and radiotherapy planning. Different ways have been used to validate the proposed system. First of all, the techniques must produce good results with the phantom data, and then the system can be tested on real data.

Different previously analyzed clinical data which has been segmented using the implemented techniques is used here to validate the system. The results obtained have been compared to the predefined results of the radiologists. In order to make the system more generic, it has been tested with data acquired from different collaborators. The first collaborator used the proposed system to validate a general standard of PET variables, providing different scans for the same dataset at different environments. They generalized the best sensitivity variables for each medical image scan based on the results obtained for each variable. The second collaborator provided predefined clinical datasets affected by cancer; they also provided the dimensionalities of the cancers. The implemented techniques were applied on these data, and the results obtained were performed by the collaborator.

In order to strengthen the system and make it ready for application with the scanners by the end users, a survey of the latter was undertaken to ascertain their perspectives on the proposed system. The validation procedure used in this chapter shows that the proposed system can be used in real applications to facilitate medical image segmentation.

Chapter 9

Conclusions and Future Work

9.1. Introduction

3D medical volume segmentation is the process of partitioning voxels in a medical volume into 3D regions (sub-volumes) that represent physical entities which are meaningful, easier to analyze and usable for other applications. The main aim of this research was to enhance the performance of new medical segmentation techniques, and use them together with other implemented segmentation techniques to make the system more accurate, robust and lossless.

MRA has been applied in this research on medical images to extract the important features that comprise ROI; these regions may be the targeted ROIs or any other obstacle in the patient body. Applying MRA removes much of the surrounding noise and makes the image more clear and ready to be segmented.

HMMs have been adapted and enhanced for segmenting medical volumes, the use of gray scale values from the input image to implement HMM matrices produced a more accurate and robust segmentation, as well as automatic segmentation without the need of

any secondary support technique. Hybrid implementation of multiresolution statistical approaches based on HMMs and MRA (wavelet and curvelet) have generated the most accurate segmentation results, where HMMs are applied to clear data instead of noisy input.

Feature Reduction methods have been used in this research to solve the problem of long computational time required for segmentation, this time is due to the huge amount of data used in 3D techniques and the amount of process in the case of HMMs.

The proposed system has been validated using predefined phantom data and previously analyzed real clinical data for patients diagnosed with cancer. The system has been also used to validate the sensitivity variables in PET scanner; it has been applied on one dataset acquired by the PET scanner at different settings. In terms of making the system general and suitable for real applications, a survey has been filled in by the end users, and the results conclude that the system can be applied to real images and helped the radiologists a lot in their analysis.

The rest of this chapter is as follows: the research objectives listed in chapter 1 are revisited in section 9.2 to ensure that it have been successfully addressed. Section 9.3 illustrates the limitations and restrictions of this research. The future work related to this thesis is introduced in section 9.4.

9.2. Research Objectives "Revisited"

The main objectives of this research are listed in Chapter 1, these having been addressed along the thesis and achieved using the proposed techniques within the fields of medical

image segmentation. Each of these objectives is now revisited to determine the success in addressing these issues:

- ***Investigate the use of wavelet transform and higher dimensional multiresolution analysis in medical image segmentation system.***

  This research investigates the use of wavelet transform using different filters and different decompositions to extract the features from medical images. Most of the noise is removed and the comprising objects were visualized clearer with sharp edges. This has been made firm with the concepts of higher dimensional MRA using curvelet transform, where curves in medical images are extracted properly to be segmented accurately.

- ***Enhance the use of Hidden Markov Models for medical image segmentation.***

  The gray scale values of medical images have been utilized in this thesis to generate HMM observation sequence. Then, probability matrices were established based on this sequence and used to train HMM for medical image segmentation. The segmentation results were promising and overcame the other available segmentation techniques.

- ***Direct 3D medical volumes segmentation.***

  The use of direct 3D image segmentation techniques without slicing the medical volume into a number of 2D images has been implemented successfully in this thesis; 3D thresholding, 3D DWT and 3D HMMs have been implemented successfully. The achieved segmentation results using 3D techniques with the proposed phantom data

was better than their pertaining 2D versions. The problem related to this is the long computational time due to the huge amount of data used for testing.

- ***Accelerate the slowest blocks in the proposed system using FR techniques.***

  The slowest block in the proposed system was the HMMs segmentation, as well as all 3D segmentation techniques. These techniques have been accelerated by reducing the number of features from the tested medical volume without significant data loss, which leads to reduce the amount of tested data. Acceleration in this thesis has been done using different FR methods, and the best results were achieved with PCA reduction, where the third dimension "number of slices" is reduced successfully.

- ***Come up with a new automatic, unsupervised and real time segmentation system.***

  The overall segmentation system was accurate; some of the proposed techniques were unsupervised as there is no need for any preprocessing steps to segment the medical data accurately. The system is also robust because the cancer could be illustrated without any loss in its contouring. The system can be applied in real medical applications, the time in some of these applications are a very important factor. Therefore, the system is close to be very fast in its computational time, it has segmented 2D and 3D medical data and located the lesions successfully without significant data loss.

- ***Validate the implemented system on real clinical applications.***

  The system has been validated on real clinical applications using different procedures, it has been tested on a phantom data and showed promising results compared to the actual phantom information. Three different real clinical datasets for patients diagnosed by lesions in different body parts have been also tested, this data has been already analyzed by the specialists who had provided cases description reports. The segmentation result achieved using our system coincides with the information given in the radiologists reports, which means that the system can be generalized for real applications.

  To emphasis this, a survey has been filled in by the end users specialists "radiologists", and the conclusion confirmed the validity of this system for real applications.

- ***Investigate the use of the proposed systems for other applications.*** Here, the proposed system has been used to test the sensitivity of PET scanner to different important variables used. One predefined phantom data has been scanned many times with different sensitivity variables, and the volumes acquired from these scans have been segmented using the proposed systems, and the achieved results were compared to the definition of the phantom. Graphs and tables of comparisons were generated and the conclusion matches the expectations about those variables.

9.3. Research Limitations

A number of restrictions and limitations have been identified during this research. Although that the aim and objectives were fulfilled successfully. These limitations can be summarized as follows:

- ***MRA using ridgelet transform***

  MRA using both wavelet and curvelet prove promising result in the proposed segmentation system; they extract the points and curves singularities properly from medical images which are rich of those singularities. Ridgelet transform has been succeed in many applications, where it is able to detect line of discontinuity, but medical images are poor to this kind of singularities and applying ridgelet transform here may damage the quality of the image instead of enhancing it. As a result, ridgelet transform is restricted to be used in the medical image segmentation system, unless for some particular images which contain a variety of straight lines such as thigh or shank bones.

- ***3D segmentation techniques***

  It has been mentioned that 3D segmentation techniques overcome their pertaining 2D versions which depends on the tested data. But the end users of the proposed system have a different opinion (based on the survey – Appendix A), as 3D techniques may fail to detect lesions that are encapsulated inside normal tissues. It is impossible to detect

this kind of lesion without decapsulating the lesion or removing all pixels comprising the surrounding tissue. In this case, the use of 2D segmentation technique is recommended.

- ***Feature reduction using DWT/WP and GPR***

  It has been mentioned in this thesis that segmentation process can be accelerated using different FR methods. The use of GPR for reducing features is limited where more than two-levels of GPR is prohibited. This is due to data loss which starts from the second level in the Gaussian pyramid. This is also happened with FR using DWT and especially when the WP decomposition is used, where a noisy output image that lost many of the comprising data will be arised with high wavelet decomposition levels.

9.4. Future Work

The following are suggested directions to the future work of this thesis:

- ***3D Curvelet Transform***

  Some 3D segmentation and feature extraction techniques have been implemented in this research, and they overcame their pertaining 2D versions. What is interesting here is 3D curvelet transform, which has not been implemented yet for the purpose of medical image segmentation. This could extract the curves which are occurring along many slices in medical volumes.

  Applying 3D curvelet transform on medical images guarantees more accurate segmentation results and could be used in many other applications.

- ***Automatic Selection of PCA eigenslices***

  An interesting area of research that can be a good future work of this research is the selection of the best eigenslice after applying PCA on medical volumes. This process has been done in this thesis manually, and the second eigenslice that were selected for all the datasets to ensure the least data loss and less noise. But sometimes the less features eigenslices may include the exact ROI with less noise, in other words, find the required features in a clearer and smaller eigenslice.

  What can be done here is to investigate a procedure for choosing the best eigenslice, as well as making this process automatic if applicable.

- ***Segmentation Technique Decision Making***

  The implemented techniques vary in their quality for segmenting medical data. Therefore, the end user can be sensitive in choosing the suitable technique. A decision making model for selecting the best segmentation technique for a specific medical data could be an extension of the work done in this thesis, and will be a very interesting area of research.

- ***Hardware Accelerations "Graphical Processing Units"***

  The use of FR techniques in this thesis for image segmentation acceleration was promising, FR is a software accelerator that can be applied to medical images before segmentation to accelerate the process. Hardware accelerators can also be used with the proposed system to do the segmentation in faster time. There are a variety of hardware accelerators that are being used nowadays such as Matlab® accelerators.

The most recent hardware implementation for real time systems is the Graphical Processing Unit (GPU), it has been used in many applications including business, accounting, engineering, as well as image processing. The basics of GPU are the multithreads processing or parallel computations, where some new versions of the GPUs can execute 1000 instructions at the same time. This is not far from the segmentation acceleration, where the same segmentation technique could be applied on all slices in parallel.

Appendix A:

Validation Survey for

Medical Image Segmentation System

This survey has been prepared and will be analyzed by Shadi M. Al Zu'bi, a Ph.D. student at Brunel University - West London.

I am doing this survey to get as much proof to help validate the proposed system, which aims to provide radiologists with a fully automated medical image segmentation system. The system helps to analyze medical images with increased accuracy, reduced noise and reduced time, in a simpler way.

This system will be responsible to facilitate the work of radiologist; it is very important to hear from the correspondents because they are the end users of the system.

For further questions, please do not hesitate to contact me on:

E-mail: shadi.alzubi@brunel.ac.uk

Mobile: (+44)7760 647 880

Name : …….

Job title : …….

Date : …….

Note: The following segmented images have been printed out in high quality and provided to the specialists with the survey.

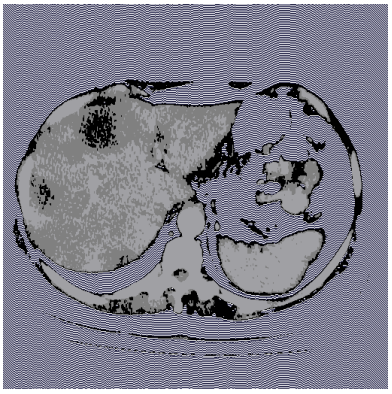

1) HMMs

2) Thresholding at t = 77

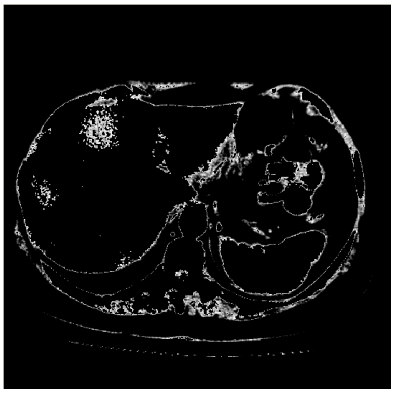

3) Inverse Thresholding at t = 50

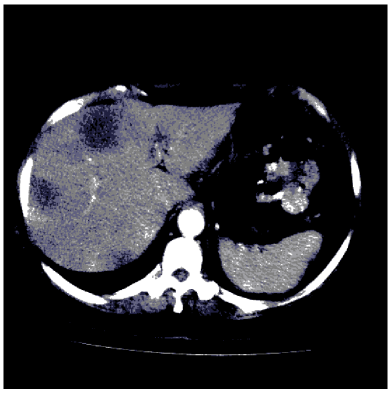

4) Clustering (6 classes)

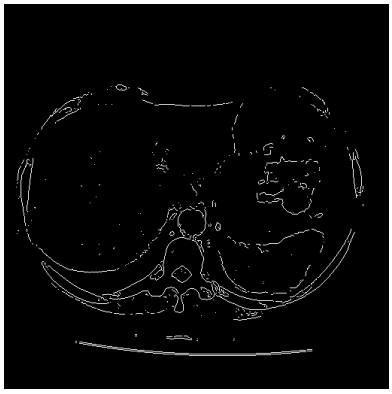

5) Edge function

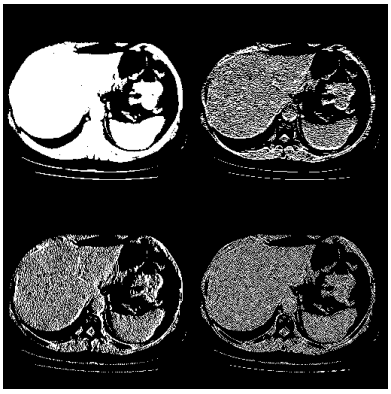

6)Wavelet Transform

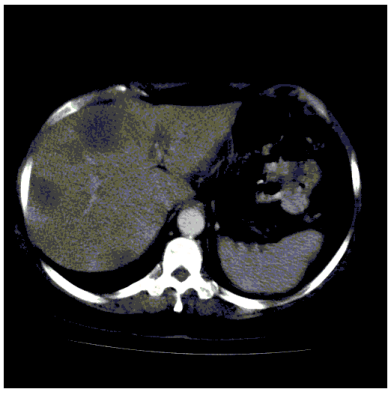

7) Ridgelet Transform

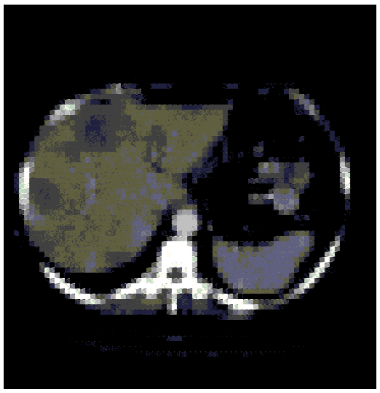

8) RADON Transform

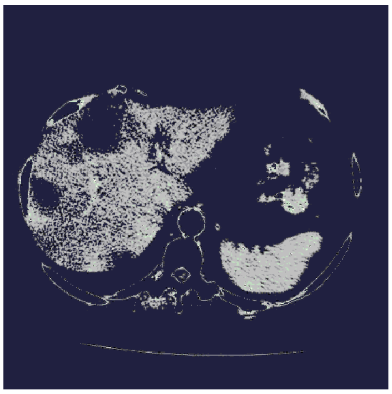

9) Curvelet Transform

Please fill the following table with numbers from 1 to 5 according to the given segmented images:

1	Extremely bad.	2	Bad.	3	Acceptable.
4	Good		5		Excellent.

Questions		Segmentation Techniques									
		1- Original	**2- Thresholding**	**3- Inverse Thresholding**	**4- Clustering**	**5- Edge function**	**6- Wavelet**	**7- Ridgelet**	**8- Radon**	**9- Curvelet**	**10- HMMs**
a.	How easy to classify the content of the output image:										
b.	The segmentation technique output illustrates the ROI clearly:										
c.	The segmentation technique output does not include noise:										
d.	The data loss in the segmentation technique output:										
e.	How easy is to analyse the segmented outputs:										
f.	Are the presented techniques beneficial for cancer diagnosis?										
g.	In your opinion, Which technique is better known and most commonly used in medical image segmentation?										
h.	**According to the overall segmentation process:**										

- In medical image analysis, do you prefer to use automatic segmented images or the original scanner output without any transformation? **Why?**

  .....

  .....

  .....

  According to the table that you filled in the previous part, which

  segmentation technique do you think is the best? **Why?**

  .....

  .....

  .....

- What problems may you face during the analysis of medical images?

  .....

  .....

  .....

- Does automatic segmentation using the proposed techniques solves the problems mentioned in the previous question?

  .....

  .....

  .....

❖ The following are two different ways of presenting 3D medical volumes.
(*Notice that you can freely rotate the volume and view it from any specific angle*)

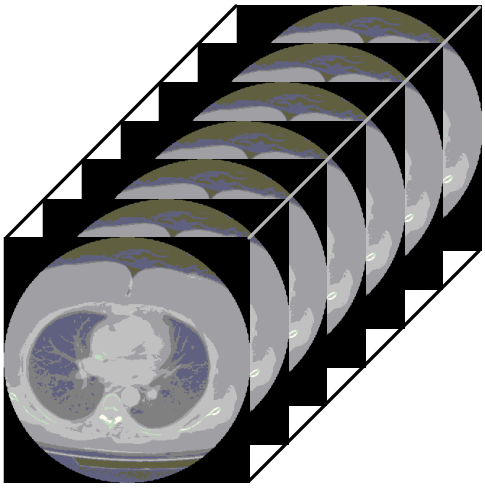

2D segmentation techniques (Slice-by-slice)

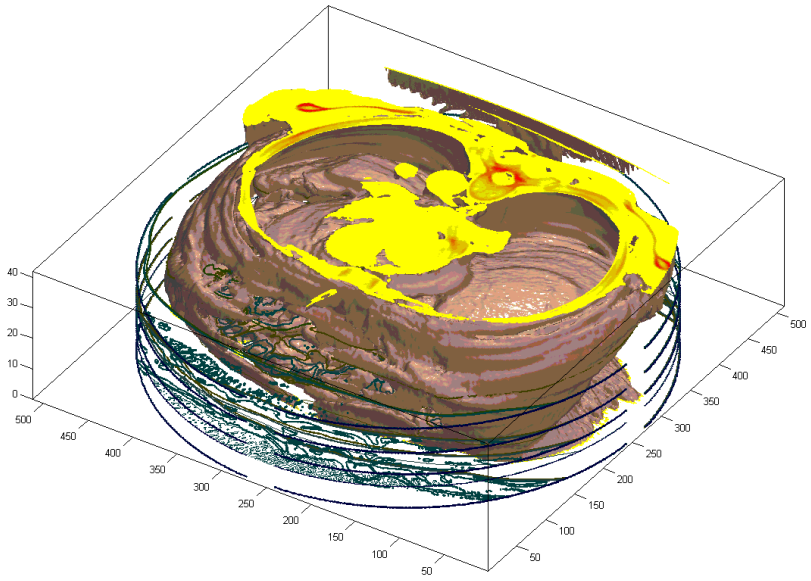

3D segmentation techniques (After volume reconstruction)

- According to the previously illustrated ways of presenting medical volumes, which way do you prefer? **Why?**

.....

.....

.....

According to the previously illustrated ways of presenting medical volumes,

which one do you think increases result accuracy? **Why?**

.....

.....

.....

Do you have any suggestion to improve the medical image segmentation

system?

.....

.....

.....

Kind regards

References

[1] D. Montgomery, "Multiscale compression and segmentation of volumetric oncological PET imagery," *Ph.D. Thesis*, The Queen's University of Belfast, Northern Ireland, UK, 2006.

[2] Lauren O'Donnell, "Semi-Automatic Medical Image Segmentation," *MSC. Thesis*, Department of Electrical Engineering and Computer Science, Massachusetts Institute of Technilogy (MIT), Massachusetts, USA, 2001.

[3] N. Nikolaidis and I. Pitas, "3-D Image Processing Algorithms," ISBN-13: 978-0471377368, Wiley-Blackwell, 2001.

[4] Medical Image Segmentation, 'http://encyclopedia.jrank.org/articles/pages/6789/Medical-Image-Segmentation.html' accessed 20th Jan 2011.

[5] M. Rizk, E. Koosha, "A Comparison of Principal Component Analysis and Generalized Hebbian Algorithm for Image Compression and Face Recognition," *IEEE 2009 International Conference on Image Processing (ICIP 2009)*, Cairo, Egypt, 2009.

[6] P. Dendy and B. Heaton, "Physics for Diagnostic Radiology, Institute of Physics," Taylor & Francis, ISBN-10: 0750305916 2002.

[7] B. Gulyas, H. Muller, "Positron Emission Tomography: A Critical Assessment of Recent Trends," Norwell, MA at Kluwer Academic Publishers, Netherlands, 1998.

[8] A. Webb, "Introduction to Biomedical Imaging," The international journal of medical physics research and practice, IEEE Press Series in Biomedical Engineering, Vol. 30, issue (1), pp. 2267, 2003.

[9] M. Ter-Pogossian, M. Phelps, E. Hoffman, "A positron-emission transaxial tomograph for nuclear imaging (PETT)," *scientific assembly and annual meeting of the Radiological Society of North America*, Washington University, USA, 1975.

[10] N. Dyson, "Radiation Physics with Applications in Medicine and Biology," *Massachusetts General Hospital in Radiation Research*, Vol. 138, No. 1, Ellis Horwood, New York, USA, 1993.

[11] D. Lardinois, W. Weder, T. Hany, E. Kamel, S. Korom, B. Seifert, G. Schulthess and H. Steinert, "Staging of Non–Small-Cell Lung Cancer with Integrated Positron-Emission Tomography and Computed Tomography," *The New England Journal of Medicine*, Vol. 348, pp. 2500-2507, 2003.

[12] T. Arulampalam, D. Costa, M. Loizidou, D. Visvikis, P. Ell, I. Taylor, "Positron emission tomography and colorectal cancer," *British Journal of Surgery*, Vol. 88, issue (2), pp. 176-189, 2001.

[13] H. Anderson and P. Price, "What Does Positron Emission Tomography Offer Oncology?" *European Journal of Cancer*, Vol. 36, ISSUE (16), pp. 2028-2035, 2000.

[14] U. Roelcke, and K. Leenders, "PET in Neuro-oncology," *Journal of Cancer Research and Clinical Oncology*, Vol. 127, Number (1), pp. 2-8, 2001.

[15] *Nobel Prize Organization*, "The Nobel Prize in Physiology or Medicine 1979," last access 6th. JAN 2011 at 13:55 'http://nobelprize.org/nobel_prizes/medicine/laureates/1979/'

[16] S. Amador Kane, "Introduction to Physics in Modern Medicine," *Taylor and Francis*, ISBN-13: 978-0415301718, 2003.

[17] D. Ingram and R. Bloch, "Mathematical Methods in Medicine, Part 2: Applications in Clinical Specialities," *John Wiley and Sons*, ISBN: 047190046x, 1986.

[18] M. Deck, C. Henschke, B. Lee, R. Zimmerman, R. Hyman, J. Edwards, L. Saint Louis, P. Cahill, H. Stein and J. Whalen, "Computed tomography versus magnetic resonance imaging of the brain, a collaborative interinstitutional study," *Clinical Imaging Journal*, Vol. 13, issue (1), pp. 2-15, 1989.

[19] R. Packer, R. Zimmerman, L. Bilaniuk, "Magnetic resonance imaging in the evaluation of treatment-related central nervous system damage," *A Cancer journal of Clinicians*, Vol. 58, issue (3), pp. 635–640, 1986.

[20] *Fight meso the lioma cancer*, "Magnetic Resonance Imaging (MRI) Scans for Mesothelioma Lung Cancer - How It Works, Magnetic Resonance? Superconducting Magnets & Precautions," 'http://www.fightmesotheliomacancer.com/mri.html' accessed: 6th. JAN. 2011 at 14:14

[21] *Discovery health*, "Howstuffworks, How MRI Works?" 'http://health.howstuffworks.com/medicine/tests-treatment/mri.htm' accessed: 6th.Jan.2011 at 14:32

[22] W. Sweet and G. Brownell, "Localization of brain tumors with positron emitters," *Nucleonics*, Vol.11, pp. 40-45, 1973.

[23] D. Mietchen, M. Aberhan, B. Manz, O. Hampe,B. Mohr,C. Neumann and F. Volke, "Three-dimensional Magnetic Resonance Imaging of fossils across taxa," *Biogeosciences Discussions*, Vol. 4, Issue (4), pp. 2959-3004, 2007. 'http://www.biogeosciences.net/5/25/2008/bg-5-25-2008.html' Accessed: 3rd Feb.2011

[24] J. Hornak, "Magnetic Resonance Imaging," *Imaging Hardware*, 'http://www.cis.rit.edu/class/schp730/lect/lect-17.htm'. Accessed: 6th.JAN.2011 at 14:20.

[25] Y. Wu, D. Chesler, M. Glimcher, L. Garrido, J. Wang, H. Jiang and J. Ackerman, "Multinuclear solid-state three-dimensional MRI of bone and synthetic calcium phosphates," *Proceeding of the National Academy of Science of the United States of America*, vol. 96, number (4), pp. 1574-1578, 1999.

[26] *The Meditech group*, "How MRI Works," 'http://www.meditech.cn/meditech-edu/mri-1.asp'. Accessed 6th. Jan. 2011 at 14:25.

[27] S. Zakavi, A. Zonoozi, V. Kakhki, M. Hajizadeh, M. Momennezhad and K. Ariana, "Image Reconstruction Using Filtered Backprojection and Iterative Method: Effect on Motion Artifacts in Myocardial Perfusion SPECT," *Journal of Nuclear Medicine Technology,* Vol. 34, Number (4), pp. 220-223, 2006.

[28] C. Moler - the creator of MATLAB, "The Origins of MATLAB". 'http://www.mathworks.com/company/newsletters/news_notes/clevescorner/dec04.html' Accessed 3rd.Feb.2011 at 01:26.

[29] C. Moler- the creator of MATLAB, "MATLAB Incorporates LAPACK - The Mathworks newsletter".'http://www.mathworks.com/company/newsletters/news_notes/clevescorner/winter2000.cleve.html' Accessed: 3rd.Feb.2011 at 01:26.

[30] R. Goering, "Matlab edges closer to electronic design automation world," *EE Times*, 'http://www.eetimes.com/electronics-news/4050334/Matlab-edges-closer-to-electronic-design-automation-world' Accessed: 3rd.Feb.2011 at 01:29.

[31] The AMIDE User's Manual V0.3, 'http://amide.sourceforge.net/help/C/index.html' Accessed: 5th. Jan. 2011 at 12:08.

[32] L. Shapiro, and G. Stockman, *Computer Vision*, Prentice Hall. ISBN 0-13-030796-3, 2002.

[33] P. Sahoo, S. Soltani and A. Wong, "A survey of thresholding techniques," *Computer Vision, Graphics and Image Processing*, Vol. 41, number (2), pp. 233–260, 1988.

[34] A. Amira, S. Chandrasekaran, D. Montgomery and I. Uzun, "A segmentation concept for positron emission tomography imaging using multiresolution analysis," *Neurocomputing for Vision Research; Advances in Blind Signal Processing*, vol. 71, issues (10–12), pp. 1954–1965, 2008.

[35] K. Jain and R. Dubes, "Algorithms for Clustering Data," *Prentice Hall*, ISBN:0-13-022278-X, 1988.

[36] J. Besag, "Statistical Analysis of Dirty Pictures," *Journal of the Royal Statistical Society*, Vol. 48, Series B, pp. 259-302, 1986.

[37] M. Sezgin and B. Sankur, "Survey over image thresholding techniques and quantitative performance evaluation," *Journal of Electronic Imaging*, Vol. 13, issue (1), 146–165, 2004.

[38] B. Yaremko, T. Riauka, D. Robinson, B. Murray, A. Alexander, A. McEwan and W. Roa, "Thresholding in PET Images of Static and Moving Targets," *Physics in Medicine and Biology*, Vol. 50, pp. 5969-5982, 2005.

[39] B. Yaremko, T. Riauka, D. Robinson, B. Murray, A. McEwan and W. Roa, "Threshold Modification for Tumour Imaging in Non-Small-Cell Lung Cancer Using Positron Emission Tomography," *Nuclear Medicine Communications*, Vol. 26, pp. 433-440, 2005.

[40] J. Daisne, M. Sibomana, A. Bol, T. Doumont, M. Lonneux and V. Gregoire, "Tri-Dimensional Automatic Segmentation of PET Volumes Based on Measured Source-to-Background Ratios: Influence of Reconstruction Algorithms," *Radiotherapy and Oncology*, Vol. 69, pp. 247-250, 2003.

[41] X. Zhang and M. Desai, "Wavelet based automatic thresholding for image segmentation," *Proceedings of the IEEE International Conference on Image Processing (ICIP '97)*, vol. 1, pp. 224–227, 1997.

[42] H. Singleton and G. Pohost, "Automatic Cardiac MR Image Segmentation Using Edge Detection by Tissue Classification in Pixel Neighborhoods," *Magnetic Resonance in Medicine*, Vol. 37, pp. 418-424, 1997.

[43] W. Polakowski, D. Cournoyer, S. Rogers, M. DeSimio and D. Ruck, "Computer-Aided Breast Cancer Detection and Diagnosis of Masses Using Difference of Gaussians and Derivative-Based Feature Saliency," *IEEE Transaction on Medical Imaging*, Vol.16, pp. 811-819, 1997.

[44] H. Cheng, Y. Lui and R. Freimanis, "A Novel Approach to Micro-calcification Detection Using Fuzzy Logic Technique," *IEEE Transaction on Medical Imaging*, Vol. 17, pp. 442-450, 1998.

[45] G. Beylkin, R. Coifman, and V. Rokhlin, "Fast Wavelet Transforms and Numerical Algorithms I," *Communications on Pure and Applied Mathematics*, Vol. 44, pp. 141-183, 1989.

[46] J. Bezdek, L. Hall and L. Clarke, "Review of MR Image Segmentation Techniques Using Pattern Recognition," *Medical Physics*, Vol. 20, pp. 1033-1048, 1993.

[47] P. Dempster, N. Laird and D. Rubin, "Maximum Likelihood from Incomplete Data via the EM Algorithm," *Journal of royal statistical society*, Vol. 39, pp. 1-38, 1977.

[48] T. Lei and W. Sewchand, "Statistical Approach to X-Ray CT Imaging and its Applications in Image Analysis," *IEEE Transaction on Medical Imaging*, Vol. 11, issue (1), pp. 62-69, 1992.

[49] Z. Liang, J. MacFall and D. Harrington, "Parameter Estimation and Tissue Segmentation from Multispectral MR Images," *IEEE Transaction on Medical Imaging*, Vol. 13, pp. 441-449, 1994.

[50] R. Acharya and R. P. Menon, "A Review of Biomedical Image Segmentation Techniques," *IEEE Computer Society Press, Deformable Models in Medical Image Analysis*, pp. 140-161, 1998.

[51] D. Pham and J. Prince, "An Adaptive Fuzzy C-Means Algorithm for Image Segmentation in the Presence of Intensity Inhomogeneities," *Pattern Recognition Letters*. Letters, Vol. 20, pp. 57-68, 1999.

[52] E. Salli, A. Visa, H. Aronen, A. Korvenoja and T. Katila, "Statistical Segmentation of fMRI Activations Using Contextual Clustering," *Proceeding in Second International Conference on Medical Image Computing and Computer-Assisted Intervention (MICCAI'99)*, Series: Lecture Notes in Computer Science, Vol. 1679, pp. 481-488, 1999.

[53] K. Leemput, F. Maes, D. Vandermeulen and P. Suetens, "A Unifying Framework for Partial Volume Segmentation of Brain MR Images," *IEEE Transaction on Medical Imaging*, Vol. 22, issue (1), pp. 105-119, 2003.

[54] K. Leemput, F. Maes, D. Vandermeulen and P. Suetens, "Automated Model-Based Tissue Classification of MR Images of the Brain," *IEEE Transaction on Medical Imaging*, Vol. 18, pp. 897-908, 1999.

[55] S. Mallat, "A theory for multiresolution signal decomposition: the wavelet representation," *IEEE Transactions on Pattern Analysis and Machine Intelligence*, Vol. 11, number (7), pp. 674-693, 1989.

[56] K. Masood, N. Rajpoot, K. Rajpoot and H Qureshi, "Hyperspectral Colon Tissue Classification using Morphological Analysis," *International Conference on Emerging Technologies (ICET '06),* pp. 735 – 741, 2006.

[57] P. Scheunders, S. Livens, G. Van-deWouwer, P. Vautrot and P. Van-Dyck, "Wavelet-Based Texture Analysis," *IEEE Conference on Image Processing and its Applications*, Vol. 2, pp. 581 – 585, 1997.

[58] P. Hill, C. N. Canagarajah, and D. Bull, "Image Segmentation Using a Texture Gradient Based Watershed Transform," *IEEE Transaction on Image Processing*, Vol. 12, issue (12), pp. 1618-1633, 2003.

[59] R. Paroli and L. Spezia, "Digital Image Segmentation Through Bayesian Hidden Markov Models," 'http://www.sis-statistica.it/files/pdf/atti/rs08_spontanee_18_1.pdf' Accessed: 11th.Jan.2011 at 04:48.

[60] D. DeMenthon, D. Doermann, M. Stuckelberg, "Image distance using hidden Markov models," *15th International conference on pattern recognition*, Vol. 3, pp. 143-146, Barcelona, Spain, 2000.

[61] Y. Liu, Y. Lin and Z. Chen, "Using hidden Markov model for information extraction based on multiple templates," *7th international conference on natural language processing and knowledge engineering*, pp. 394-399, Beijing, China, 2003.

[62] D. Donoho, "Ridge functions and orthonormal ridgelets," *Journal of Approximation Theory*, Vol. 111, issue (2), pp. 143–179, 2001.

[63] B. Hou, F. Liu and L. Jiao, "Linear feature detection based on ridgelet," *Science in China, Series E: Technological Science*, Vol. 46, pp. 141-152, 2003.

[64] Y. Li, M. He and C. Li, "An Approximate Finite Ridgelet Transform Algorithm for SAR Image Segmentation," *8th International Conference on Signal Processing*, Bejing, China, 2006.

[65] P. Danielsson, "Euclidean distance mapping," *Computer Graphics and Image Processing*, Vol. 14, issue 3, pp. 227-248, 1980.

[66] K. Zou, S. Warfield and A. Bharatha, "Statistical validation of image segmentation quality based on a spatial overlap, index 1, scientific reports," *Academic Radiology*, vol. 11, number (2), pp. 178–189, 2004.

[67] Q. Huynh-Thu, M. Ghanbari, "Scope of validity of PSNR in image/video quality assessment," *IET Electronics Letters journal*, Vol. 44, issue 13, pp.800-801, 2008.

[68] L. Lehmann, G. Casella, "Theory of Point Estimation, second edition," *Springer*, ISBN 0-387-98502-6, New York, 1998.

[69] S. Alzu'bi, A. Amira, "3D Medical Volume Segmentation Using Hybrid Multiresolution Statistical Approaches," *Advances in Artificial Intelligence*, *Special issue on Machine Learning Paradigms for Modeling Spatial and Temporal Information in Multimedia Data Mining,* vol. 2010, 2010. [Accessed: 3rd.Feb.2010]. http://www.hindawi.com/journals/aai/2010/520427.html.

[70] J. Starck, M. Elad and D. Donoho, "Redundant multiscale transforms and their application for morphological component separation," *Advances in Imaging Electron Physics*. Vol. 132, pp. 287–348, 2004.

[71] A. Mojsilovic, M. Popovic, S. Markovic, M. Krstic, "Characterization of visually similar diffuse diseases from B-scan liver images using nonseparable wavelet transform," *IEEE Transaction on Medical Imaging*, Vol. 17, issue (4) pp. 541–549, 1998.

[72] C. Mulcahy, "Image compression using the Haar wavelet transform," *Spelman Science and Math Journal,* Vol. 1, pp. 22–31, 1997.

[73] W. Fourati, F. Kammoun, M. Bouhlel, "Medical image denoising using wavelet thresholding," *Journal of Testing and Evaluation*. ISSN: 1945-7553, Vol. 33, issue (5), 2005.

[74] B. Kara, N. Watsuji, "Using wavelets for texture classification," *IJCI Proceedings of International Conference on Signal Processing*, ISN 1304-2386, pp. 920–924, 2003.

[75] M. Do, M. Vetterli, "The finite ridgelet transform for image representation," *IEEE Transaction on Image Processing*, Vol. 12, pp. 16–28, 2003.

[76] M. Do, M. Vetterli, "Image denoising using orthonormal finite ridgelet transform," *Proceedings of SPIE: Wavelet Applications in Signal and Image Processing*, vol. 4119, pp. 831–842, 2003.

[77] E. Candes, L. Demanet, D. Donoho and L. Ying, "Fast Discrete Curvelet Transform," *Applied and Computational Mathematics*, Tutorial in Department of Statistics, Stanford University, CA, USA, 2006.

[78] I. Daubechies, "Wavelet transforms and orthonormal wavelet bases, Different Perspectives on Wavelets," *Proceedings of Symposia in Applied Mathematics*, *American Mathematical Society,* vol. 47, pp. 1-33, 1993.

[79] I. Uzun and A. Amira, "Design and FPGA Implementation of Finite Ridgelet Transform," *IEEE International Symposium on Circuits and Systems (ISCAS'05)*, Vol. 6, pp. 5826 - 5829, 2005.

[80] E. Stollnitz, T. DeRose and D. Salesin, "Wavelets for Computer Graphics: A Primer, Part 1," *IEEE Computer Graphics and Applications*, Vol. 15, issue (3), pp. 76 - 84 2002.

[81] A. Haar, "Zur Theorie der Orthogonalen Funkt Ionensysteme," *Mathematische Annalen*, Vol. 71, Number (1), pp. 331-371, 1910.

[82] I. Daubechies, "Orthonormal Bases of Compactly Supported Wavelets," *Communications on Pure and Applied Mathematics*, Vol. 41, issue (7), pp. 909-996, 1988.

[83] M. Antonini, M. Barlaud, P. Mathieu and I. Daubechies, "Image Coding Using the Wavelet Transform," *IEEE Transactions on Image Processing*, Vol. 1, pp. 205-220, 1992.

[84] A. Cohen, I. Daubechies and J. Feauveau, "Biorthogonal Bases of Compactly Supported Wavelets," *Communications on Pure and Applied Mathematics*, Vol. 45, issue (5), pp. 485-560, 1992.

[85] D. LeGall and A. Tabatabai, "Subband Coding of Digital Images Using Symmetric Short Kernel Filters and Arithmetic Coding Techniques," *Proceedings of IEEE International Conference on Acoustics, Speech and Signal Processing (ICASSP'88)*, Vol. 2, pp. 761-764, USA, 1988.

[86] D. Montgomery, A. Amira and F. Murtagh, "A Non-Separable Lifting Approach for 3D Image Compression," *Proceedings of IEEE International Conference on Acoustics, Speech and Signal Processing (ICASSP'04)*, Vol. 3, pp. iii, 137, 40, Montreal, Canada, May 2004.

[87] M. Unser and T. Blu, "Mathematical Properties of the JPEG2000Wavelet Filters," *IEEE Transactions on Image Processing*, Vol. 12, issue (9), pp. 1080-1090, 2003.

[88] I. Daubechies, "Ten Lectures on Wavelets," S*ociety for Industrial and Applied Mathematics (SIAM)*, ISBN-13:978-0-898712-74-2, Philadelphia, USA, 1992.

[89] R. Calderbank, I. Daubechies, W. Sweldens and B. Yeo, "Wavelet Transforms that Map Integers to Integers," *Applied and Computational Harmonic Analysis*, Vol. 5, number (3), pp. 332-369, 1998.

[90] E. Cand'es and D. Donoho, "Curvelets - a surprisingly effective non-adaptive representation for objects with edges," *4th International Conference on Curves and Surfaces*, Curve and Surface Fitting, Vol. 2, pp. 105-120, ISBN 0-8265-1357-3, Saint-Malo, France, 2000.

[91] M. Do and M.Vetterli, "Orthonormal Finite Ridgelet Transform for Image Compression," *Proceedings on International Conference on Image Processing (ICIP)*, vol. 2, pp. 367-370, 2000.

[92] E. Candes, "Ridgelets: Theory and Application," *Ph.D. thesis*. Department of Statistics, Stanford University, 1998.

[93] E. Candes and D. Donoho, "Ridgelets: A key to higher-dimensional intermittency?" *Philosophical Transactions of the Royal Society*, Vol. 357, number (1760), pp. 2495-2509, 1999.

[94] J. He, "A characterization of inverse Radon transform on leguerre hypergroup," *Journal of Mathematical Analysis and Applications*, Vol. 318, issue (1), pp. 387-395, 2006.

[95] L. Dettori and L. Semler, "A comparison of wavelet, ridgelet, and curvelet-based texture classification algorithms in computed tomography," *Computers in Biology and Medicine*, Vol. 37, issue (4), pp. 486 – 498, 2007.

[96] Computed tomography scanner technical report, Diagnostic Radiology and Nuclear Medicine Department, *King Abdullah University Hospital*, Ramtha, Jordan, 2009.

[97] J. Starck, E. Candes and D. Donoho, "The curvelet transform for image denoising," *IEEE Transactions on Image Processing*, vol. 11, number (6), pp. 670-684, 2002.

[98] I. Sumana, "Image Retrival using discrete curvelet transform," *Master's Thesis*, Monash University, Australia, 2008.

[99] L. Demanet, *The curvelet Organization*, 'http://www.curvelet.org/software.html' Access: 18th.July.2010 at 00:53.

[100] *International Electrotechnical Commission (IEC)*, 61675-1, Geneva, Switzerland, 1998. And *National Electrical Manufacturers Association (NEMA)*, Standards Publication No. NU2, Washington, D.C, 2001.

[101] W. Jentzen, L. Freudenberg, E. Eising, M. Heinze, W. Brandau, and A. Bockisch, "Segmentation of PET volumes by iterative image thresholding," *Journal of Nuclear Medicine*, vol. 48, number (1), pp. 108–114, 2007.

[102] M. Elmezain, A. Al-Hamadi, B. Michaelis, "Hand Trajectory-based Gesture Spotting and Recognition Using HMM", *16th IEEE International Conference on Image Processing (ICIP'09)*, pp. 3577-3580, Cairo-Egypt, 2009.

[103] D. Montgomery, A. Amira, and H. Zaidi, "Fully automated segmentation of oncological PET volumes using a combined multiscale and statistical model," Medical Physics, vol. 34, number (2), pp. 722–736, 2007.

[104] J. Lu and L. Carin, "HMM-based multiresolution image segmentation," *Proceedings of the IEEE International Conference on Acoustic, Speech, and Signal Processing (ICASSP)*, pp. 3357–3360, Durham, USA, 2002.

[105] A. Huang, R. Abugharbieh, and R. Tam, "Image segmentation using an efficient rotationally invariant 3D region-based hidden Markov model," *Proceedings of the IEEE Computer Society Conference on Computer Vision and Pattern Recognition Workshops (CVPR '08)*, pp. 107–111, Alaska, USA, 2008.

[106] D. DeMonthon and M. Vuilleumier, "Image distance using hidden Markov models," *Proceedings of the 15th International Conference on Pattern Recognition (ICPR '00)*, vol. 3, pp. 143 - 146, Barcelona-Spain, 2000.

[107] L. Rabiner, "A Tutorial On Hidden Markov Models And Selected Applications In Speech Recognition," *Morgan Kaufmann Publishers Inc*., San Francisco, USA, 1990.

[108] J. Li and J. Wang, "Studying digital imagery of ancient paintings by mixtures of stochastic models," *IEEE Transactions on Image Processing*, vol. 13, number (3), pp. 340–353, 2004.

[109] J. Jiten and B.Merialdo, "Semantic image segmentation with a multidimensional hidden Markov model," *Advances in Multimedia Modeling Conference, Lecture Notes in Computer Science,* vol. 4351, pp. 616–624, 2006.

[110] Y. He and A. Kundu, "2D shape classification using hidden Markov model," *IEEE Transactions on Pattern Analysis and Machine Intelligence*, vol. 13, number (11), pp. 1172–1184, 1991.

[111] N. Arica and F. Vural, "A shape descriptor based on circular hidden Markov model," *Proceedings of the 15th IEEE International Conference on Pattern Recognition*, vol. 1, pp. 924-927, Spain, 2000.

[112] J. Solomon, J. Butman, and A. Sood, "Segmentation of brain tumors in 4D MR images using the hidden Markov model," *Computer Methods and Programs in Biomedicine*, vol. 84, number (2-3), pp. 76-85, 2006.

[113] P. Nicholl, "Face Recognition using Multiresolution Statistical Approaches," *Ph.D. Thesis*, School of Electronics, Electrical Engineering and Computer Science, The Queen's University of Belfast, Northern Ireland, UK, 2009.

[114] HS. Le and H. Li, "Recognizing Frontal Face Images Using Hidden Markov Models with One Training Image per Person," *Proceedings of the 17th International Conference on Pattern Recognition (ICPR)*, Vol. 1, pp. 318-321, 2004.

[115] T. Othman, "A Separable Low Complexity 2D HMM with Application to Face Recognition," *IEEE Transactions on Pattern Analysis and Machine Intelligence (TPAMI)*, vol. 25, number (10), pp. 1229-1238, 2003.

[116] X. Ma, D. Schonfeld and A. Khokhar, "Distributed multidimensional hidden Markov model: theory and application in multiple-object trajectory classification and recognition," *SPIE International Conference on Multimedia Content Access: Algorithms and Systems*, San Jose, California, 2008.

[117] Y. Zhang, M. Brady and S. Smith, "Segmentation of brain MR images through a hidden Markov random field model and the expectation-maximization algorithm," *IEEE Transactions on Medical Imaging*, vol. 20, number (1), pp. 45–57, 2001.

[118] J. Li, A. Najmi and R. Gray, "Image classification by a two-dimensional hidden Markov model," *IEEE Transactions on Signal Processing*, vol. 48, number (2), pp. 517–533, 2000.

[119] D. Bouchaffra, J. Tan, "Introduction to the Concept of Structural HMM: Application to Mining Customers' Preferences in Automotive Design," *17th International Conference on Pattern Recognition (ICPR'04)*, vol. 2, pp.493-496, Cambridge, UK, 2004.

[120] A. Balter, "DICOM to three Dimentional," *Pacific Northwest National Laboratory*, 2009.

[121] S. Chang, B. Yu and M. Vetterli, "Spatially adaptive wavelet thresholding with context modeling for image denoising," *IEEE Transactions on Image Processing*, vol. 9, number (9), pp. 1522-1531, 2000.

[122] R. Zhang, W. Ouyang and W. Cham, "Image Multi-Scale Edge Detection using 3D Hidden Markov Model Based on the Non-Decimated Wavelet," *16th IEEE International Conference on Image Processing (ICIP'09)*, Cairo, 2009.

[123] W. Huang and H. Yin, "Linear and nonlinear dimensionality reduction for face recognition," *16th IEEE International Conference on Image Processing (ICIP'09)*, Cairo, 2009.

[124] P. Moravec, V. Snel, "Dimension Reduction Methods for Image Retrieval," *Sixth International Conference on Intelligent Systems Design and Applications (ISDA '06)*, pp. 1055 – 1060, Jinan, China, 2006.

[125] The MathWorks™, "Image Processing Toolbox 6: User's Guide," September 2009, Revised for Version 6.4, *Release 2009b*, pp. 9-16, 'http://www.mathworks.com/help/toolbox/images/rn/br218x3-1.html' Accessed: 3rd.Feb.2011.

[126] P. Burt and E. Adelson, "The Laplacian Pyramid as a Compact Image Code," *IEEE Transactions on Communications*, vol. 31, issue (4), pp. 532-540, 1983.

[127] A. AlMuhit, M. Islam and M. Othman, "VLSI Implementation of Discrete Wavelet Transform (DWT) for Image Compression," *2nd International Conference on Autonomous Robots and Agents*, Vol. 4, issue (4), pp. 421-433, New Zealand, 2004.

[128] P. Nicholl, A. Ahmad and A. Amira. "Optimal Discrete Wavelet Transform (DWT) Features for Face Recognition," *2010 IEEE Asia Pacific Conference on Circuits and Systems (APCCAS'10)*, Kuala Lumpur, Malaysia, 2010

[129] A. Abbas, M. Khalil, S. AbdelHay, H. Fahmy, "Illumination invariant face recognition in logarithm discrete cosine transform domain," *IEEE International conference on image processing*, pp. 4157 – 4160, Cairo, Egypt, 2009.

[130] M. Turk and A. Pentland, "Eigenfaces for Recognition," *Journal of Cognitive Neuroscience*, Vol. 3, issue (1), pp. 71-86, 1991.

[131] R. Gonzalez, R. Woods and S. Eddins, "Digital Image Processing using Matlab," second edition, ISBN: 9780982085400, *Gatesmark Publishing*, 2009.